

UNCLASSIFIED

AD NUMBER

AD480727

LIMITATION CHANGES

TO:

Approved for public release; distribution is unlimited.

FROM:

Distribution authorized to U.S. Gov't. agencies and their contractors;
Administrative/Operational Use; 01 MAY 1960.
Other requests shall be referred to Air Force Cambridge Research Laboratories, Attn:
Geophysics Research Directorate, Hanscom AFB, MA.

AUTHORITY

AFCRL ltr dtd 22 Dec 1971

THIS PAGE IS UNCLASSIFIED

SECURITY

MARKING

The classified or limited status of this report applies to each page, unless otherwise marked.

Separate page printouts MUST be marked accordingly.

THIS DOCUMENT CONTAINS INFORMATION AFFECTING THE NATIONAL DEFENSE OF THE UNITED STATES WITHIN THE MEANING OF THE ESPIONAGE LAWS, TITLE 18, U.S.C., SECTIONS 793 AND 794. THE TRANSMISSION OR THE REVELATION OF ITS CONTENTS IN ANY MANNER TO AN UNAUTHORIZED PERSON IS PROHIBITED BY LAW.

NOTICE: When government or other drawings, specifications or other data are used for any purpose other than in connection with a definitely related government procurement operation, the U. S. Government thereby incurs no responsibility, nor any obligation whatsoever; and the fact that the Government may have formulated, furnished, or in any way supplied the said drawings, specifications, or other data is not to be regarded by implication or otherwise as in any manner licensing the holder or any other person or corporation, or conveying any rights or permission to manufacture, use or sell any patented invention that may in any way be related thereto.

7C

FILE COPY

19

⑩ R. E. Eisele .

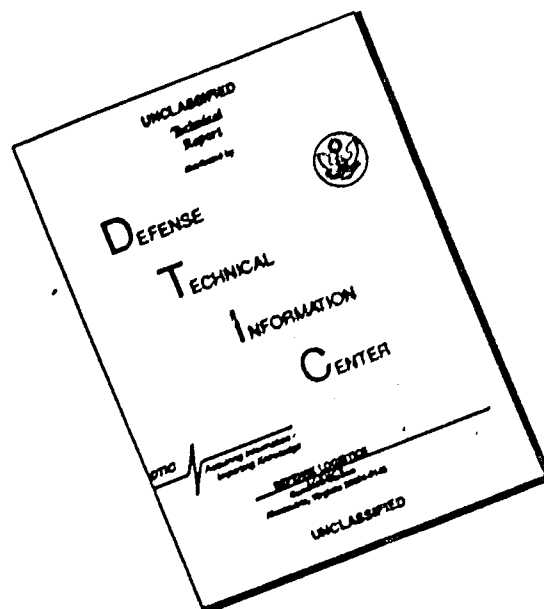
~~CANOGA PARK, CALIFORNIA~~ OK
L.A.

13

DDC
RECEIVED
APR 22 1966
RECEIVED
C

ack

DISCLAIMER NOTICE



THIS DOCUMENT IS BEST QUALITY AVAILABLE. THE COPY FURNISHED TO DTIC CONTAINED A SIGNIFICANT NUMBER OF PAGES WHICH DO NOT REPRODUCE LEGIBLY.

FROM Commanding General U.S. Army Electronics Command ATTN: ANGEL-ED-MAT Fort Monmouth, New Jersey 07703		REQUEST FOR/TRANSMITTAL OF PUBLICATIONS	
TO Commander Air Force Cambridge Research Laboratories CHRA, Step 39 L.O. Hanscom Field Bedford, Mass 01731		FOR DATE 6 April 1966	
REQUEST	<input type="checkbox"/> ON L.O. <input type="checkbox"/> FOR ATTENTION <input type="checkbox"/> RECALL OF L.O. <input checked="" type="checkbox"/> INFORMATION (X) Send loan copy if retention copy is not available.	PUBLICATIONS REQUESTED: "INTEGRATED BACKWARD INVESTIGATION", by R.E. Eisel, Final, Thompson Ramo-Wooldridge Inc., Contr. AF 19(604)-3473, dtd 1960. DOCUMENT NOT AVAILABLE FROM DDC.	
	TRANSMITTAL <input type="checkbox"/> ON L.O. <input type="checkbox"/> FOR ATTENTION <input type="checkbox"/> RECALL OF L.O. <input type="checkbox"/> _____		
REMARKS BY LENDING ACTIVITY			
NOTES: DO NOT FURNISH ANY PUBLICATION FOR WHICH DOCUMENT IS REQUESTED. ADVISE DDC AND ARMY OFFICIAL CONCERNING DELIVERY.			
SOURCE OF REFERENCE		SIGNATURE THOMAS J. LALLI Dd, Technical Documents Center	

CONTENTS

	<u>Page</u>
Introduction	1
Discussion of Key West Background Data	3
Initial Considerations Underlying a Model	27
Empirical Considerations for a Brightness Model	48
Estimated Earth and Sky Background Noise Interference in Infrared Devices	65
Summary	88
References	91

ACQUISITION BY	
SECRET	WHITE SHOT/NOISE <input type="checkbox"/>
SAC	DIFF. SHOT/NOISE <input checked="" type="checkbox"/>
UNANNOUNCED	
JUSTIFICATION	
BY <i>Ln</i>	
DISTRIBUTION/AVAILABILITY CODES	
REG.	AVAIL. and/or SPECIAL
2	

LIST OF ILLUSTRATIONS

<u>No.</u>	<u>Title</u>	<u>Page</u>
1.	Elevation and Azimuth of the Sun for Key West Local Standard Time	8
2.	Overcast Sky, June 16, 1959, Key West, 0-16 Microns	9
3.	Overcast Sky, June 17, 1959, Key West, 0-16 Microns	10
4.	Overcast Sky, June 17, 1959, Key West, 4.25 Microns	11
5.	Blue Sky Areas in a Cloudy Sky, June 23, 1959, Key West, 4.25 Microns	12
6.	Average Spectral Distribution, Overcast Sky, June 16, 1959	13
7.	Average Spectral Distribution, Overcast Sky, June 17, 1959	14
8.	Average Spectral Distribution, Overcast Sky, "Cloudy-Bright", June 19, 1959.	15
9.	Average Spectral Distribution, Blue Sky Areas in a Cloudy Sky, June 23, 1959.	16
10.	Amplitude Probability for Blue Sky at 3 Waves Per Radian	17
11.	Amplitude Probability for Clouds	18
12.	Ninety-Five Percent Distribution Limits for Blue Sky One-Dimensional Power Spectrum	19
13.	Ninety-Five Percent Distribution Limits for Clouds One-Dimensional Power Spectrum	20
14.	Ninety-Five Percent Distribution Limits for Cloud and Sky One-Dimensional Power Spectrum	21
15.	Individual Amplitude Probability Curves - Clouds	22
16.	Individual Amplitude Probability Curves - Clouds	23
17.	Individual Amplitude Probability Curves - Clouds	24

LIST OF ILLUSTRATIONS (Cont'd.)

<u>No.</u>	<u>Title</u>	<u>Page</u>
18.	Individual Spectra for Blue Sky for the Azimuth Plane Perpendicular to the Sun Azimuth Plane	25
19.	Individual Spectra for Blue Sky for the Sun Azimuth Plane	26
20.	Atmospheric Model	44
21.	Typical Absorption Spectra of Major Atmospheric Components	45
22.	Effective Scattering Ratio to Geometrical Cross Sectional Area	46
23.	Scattering Area Coefficient for Several Refraction Indices	46
24.	Scattering Distribution For a Large Spherical Particle	47
25.	Droplet Spectra for Various Types of Clouds	47
26.	Averaged Overcast Sky, June 17, 1959, 4.25 Microns	59
27.	0-16 Micron Region With Respect to Sun Position	60
28.	Computed 0-16 Micron Region for June 16th	61
29.	Computed 0-16 Micron Region for June 17th	62
30.	Computed 4.25 Micron Region for June 23rd	63
31.	Effect of β on $f(\theta)$	64
32.	Effect of α on $f(\phi)$	64
33.	Radiometric Sky Observations	80
34.	Assumed Probability Distribution of Cloud Lengths	81
35.	Schematic Description of Assumed Background	69
36.	Predicted One Dimensional Wiener Background Spectra	32
37.	One Dimensional Wiener Background Spectra - Solar Reflection	83

LIST OF ILLUSTRATIONS (Cont'd.)

<u>No.</u>	<u>Title</u>	<u>Page</u>
38.	One Dimensional Wiener Background Spectra - Thermal Emission	84
39.	Predicted Two Dimensional Wiener Background Spectra	85
40.	Linear Optical Imaging System	86
41.	Transform of Parallel Slit and Radial Reticles	87

INTRODUCTION

✓
COVER ✓
This ~~is the final report to be issued on Contract AF19(604)-3473.~~ This contract was issued by the Geophysics Research Directorate of the Air Force Cambridge Research Center to obtain data concerning the radiant intensity of the infrared sky background and the amplitude of the sky gradient. Measurement of the infrared sky background has been a more or less continuous program since July 1953 and a continuous record of the work accomplished can be gleaned from a ~~perusal~~ of the reports issued, which are included in the reference list. ~~The largest amount of data obtained in the overall program has been taken during the present contract, AF19(604)-3473.~~ Both the radiometric data and the gradient data ~~will be~~ discussed. The actual data have been presented in Reports No. 1, 2, and 3 preceding this final report and the discussions ~~will be~~ based on those data. An empirical form has been worked out for the brightness data taken at Key West, Florida, in June 1959. It had been hoped that the measurements at Key West might result in a mathematical model for sky brightness in the infrared. This might have been possible had completely cloudless blue skies presented themselves for measurement. This condition never occurred; however, work has been done with the data taken to result in a fairly simple and possibly quite useful equation that may prove, with further investigation and consequent modification, to be more general than a mathematical model applying only to blue sky.

Gradient data is also discussed and some work has been done to determine the values of the most likely gradients for blue sky, clouds, and cloud edges. A theoretical mathematical model for the infrared background gradient is presented which includes some considerations concerning the spectrum expected viewing the earth background from various altitudes. Some discussion is included concerning the use of gradient data in the design of equipment.

This final report also includes a summary of the background investigation work from its inception in 1953 with the building of the instrumentation used to obtain the data. Some of the more important phases of the work are discussed in some detail so that this report will bring most of the past work into one bound volume. The theoretical mathematical model for the background gradient gives indications of areas for future measurement work and this is discussed in the summary.

Contract AF19(604)-3473 has been performed by the Infrared Department of Ramo-Wooldridge, a Division of Thompson Ramo Wooldridge, Inc. Personnel directly connected with the performance of this Contract are:

T. R. Whitney	Member Senior Staff	Department Head
G. F. Aroyan	Member Senior Staff	Asst. Dept. Head
P. W. Shadle	Member Technical Staff	Group Head
R. E. Eisele	Member Technical Staff	Project Head
J. W. Fisk	Member Technical Staff	
C. J. Somol	Research Assistant	

DISCUSSION OF KEY WEST BACKGROUND DATA

The data published in Reports No. 2 and 3 were taken at Key West, Florida, in June 1959, as part of a measurement field trip in cooperation with IRMP 59/60. The data was obtained with a combined filter radiometer and gradient meter, the design and operation of which is completely described in previous reports. The calibrations and corrections used in reduction of the data are included in the two reports (4) containing the tabulations. The purpose in this section will be to summarize the data.

Key West is at $24^{\circ} 34'$ latitude and $81^{\circ} 45'$ longitude. It is thus just north of the Tropic of Capricorn and well within the hurricane belt. On June 21, the sun is at the highest elevation and passes very close to zenith at noon solar time and also follows a general East-West azimuth. The plot of sun ordinates with respect to local standard time, Figure 1, shows that the path of the sun does not vary more than 5 degrees from this azimuth between the hours of 10 a.m. and 3 p.m. and no more than 20 degrees throughout the course of the day. It was hoped that radiometric or brightness data taken on cloudless skies would, for this reason, lend itself more easily to evaluation and lead to a simple function for sky brightness in the infrared, thus making conclusions more general for the area. Simply because of the location and the time of year, the mixing of the air mass becomes quite turbulent and leads to constant cloudiness, recurrent storms and brisk winds. The data is indicative of these conditions and represents the radiative character of the sky only for this location and time of year.

RADIOMETER DATA

Data taken June 16th and June 17th are for completely overcast skies which, to the eye, were completely gray and featureless. The sun position was indicated by a large bright area in the cloud cover due to heavy scattering. Total radiation under

such conditions was measured using the bolometer with no spectral filters in the system. The bolometer spectral range is limited by a sodium chloride window and represents a wavelength range from 0 to 16 microns. Polar plots, Figure 2 and 3, sum the data points. The sun position is indicated by an asterisk and represents the midpoint of the sun's travel through the course of the measurements. About 30 minutes is required to gather the information for one plot during which time the sun would have moved a total of 7.5 degrees. The two plots are quite similar with small local differences which are no doubt due to differences in thickness of cloud cover. The energy levels in Figure 2 are slightly lower near the sun than for Figure 3, and for an earlier time of day, but the differences are not great and are no doubt due to changing conditions in overcast. A low area is indicated in Figure 3 about 60 degrees west of the sun position, but, since there is no indication of this in the previous day's run, the cause again is probably differing thickness in cloud cover. Since this spectral region includes the 8 to 12 micron "window", these differences may be due to warmer and colder cloud patches with the cooler areas being thicker. This conjecture is more plausible under such conditions than to presume the cause to be solely scattering in the short wavelength region since the sky was visibly uniformly gray with consequent low illumination levels as borne out by filter measurements in the near infrared under the same conditions.

Figure 4 is a detailed plot of the overcast sky at 4.25 microns. This information was obtained immediately following the total radiation measurement in Figure 3, but no particular correlation is indicated between the two plots. A much more uniform set of curves probably would have resulted had the spectral filter been narrower. The filter at 4.25 microns has a one micron bandwidth and consequently radiation is admitted on both sides of the CO₂ absorption band. Several high energy regions are indicated on the diagram approximately 75 degrees from the sun and an increasing gradient is indicated in the southeast area down to

the horizon. The measurements in this direction were over water which extended perhaps one-half mile and directly beyond this were concrete runways towards the end of the airstrip at Boca Chica (Naval Air Station at Key West). Probably because of the inclement weather, there were no aircraft operating on either of these two days. The total radiation map does in a general way show a high tendency in this same area. Several days later, June 23rd, it was possible to obtain data on blue sky patches in a very cloudy sky. Figure 5 presents this group of measurements for comparison with Figure 4. In general, the data are rather similar. The blue sky observations do not show the details of the overcast sky and the gradient is much more uniform. A general minimum area can be seen at about 70 degrees from the sun. June 23rd was a bright sunny day with many large, white, cumulus clouds. The ambient temperature was 84°F on June 17th and 85°F on June 23rd, but the sun was at a higher elevation for the measurements of the 23rd. The values at the horizon are higher than the blackbody radiation at 4.25 microns for the ambient 85°F which is $140\text{ }\mu\text{W}/\text{cm}^2 \cdot \text{steradian} \cdot \text{micron}$. Again, this may be due to radiation outside the CO_2 absorption band.

Polar plots could be presented for the other spectral regions except that the details are so numerous that the plots are very difficult to prepare and, as a consequence, would be difficult to interpret. It is felt that a spectral plot showing highs, lows and averages for the day give a much better general idea of the radiation characteristics. This information is given for June 16th in Figure 6 for heavy overcast. The average readings are shown bracketed with a shaded area designated as "measurement accuracy". The measurement accuracy is taken as $\pm 6\%$ since both the energy calibration and the voltage calibration each repeat within 2% and the data is read from the record probably within 2%. Whenever the low values were read, a variation of about $\pm 5\text{ }\mu\text{W}/\text{cm}^2 \cdot \text{steradian} \cdot \text{micron}$ was noticed over a 10 to 15 second time duration. This has been attributed to variations in

the background since it does not occur in the laboratory when looking into the blackbody, nor is it periodic. Further, no correlation between filter regions could be observed, i.e. the energy level might be increasing slightly in one filter region while decreasing in another. Motion of the clouds may be the largest contributing factor although variations of this small amplitude could be due to many factors in the background. The variation has been added to the accuracy envelop. Average spectral data for June 17, 19 and 23 are given in Figures 7, 8 and 9. The measurements taken June 19th are designated as "cloudy-bright" which means that the sky was overcast but clearing with a consequent increase in the brightness. The 23rd was quite cloudy with patches of blue sky showing all over which gave the sky a mottled appearance. All data for this day are for blue sky under this condition.

GRADIENT DATA

The gradient data has been sorted into three general classifications: (1) Blue Sky, (2) Clouds, and (3) Clouds and Sky. Those for blue sky are for blue patches of sky under very bright cloudy sky conditions. It is indicative of the conditions at Key West in June that only 90 such measurements could be made during the whole measurement period. Since a 6 degree scanning circle was used to develop the background function, patches of sky smaller than 10 or 12 degrees were ignored because of the possibility of inadvertently including clouds in the field. To enhance the usefulness of the gradient data, each classification was sorted to determine the probable amplitude occurrence at particular frequencies. Histograms were constructed for ten-space frequencies from 3 to 150 waves per radian. From these, probability curves were developed and 95% distribution limits were determined. As an example, Figure 10 shows how the measured amplitudes for 3 waves per radian were distributed for the blue sky data. Figure 11 is a photograph showing the distributions

for clouds erected on a frequency-amplitude chart. This treatment of gradient data provides 95% distribution limit charts for the three general classifications. Figures 12, 13, and 14 represent the complete statistical summary of the sky gradient in the lead sulfide region for Key West during the month of June. These charts include all positional points measured and for this reason are completely general. These charts are presented with the energy ordinate squared and are, therefore, the one dimensional power spectra for the three sky conditions. The center solid line is the peak of the probability curves with the upper and lower solid lines determining the upper and lower limits between which 95% of the total number of measurements lie. Dashed lines of various slopes are included for comparison. Similar measurements made from Mt. Wilson in 1956 showed similar characteristics with the power spectra running slopes to -3.

Because secondary peaks regularly appear in the probability curves for clouds, these are presented in Figures 15, 16, and 17. A definite trend to a secondary slope at higher amplitude levels is indicated for the cloud measurements. No explanation of this is attempted here except to point out that the classification "Clouds" is quite general and further breakdown of this classification into cloud types might reveal more detailed trends.

At times, gradients were measured on the blue sky to look for trends from horizon to zenith for one sun position. No significant trend was observed. Figures 18 and 19 can be considered as representative of this type of data. Figure 18 shows the spectra observed for different elevations for the azimuth plane nearly at right angles to the plane of the sun, while Figure 19 gives similar information for the azimuth plane of the sun.

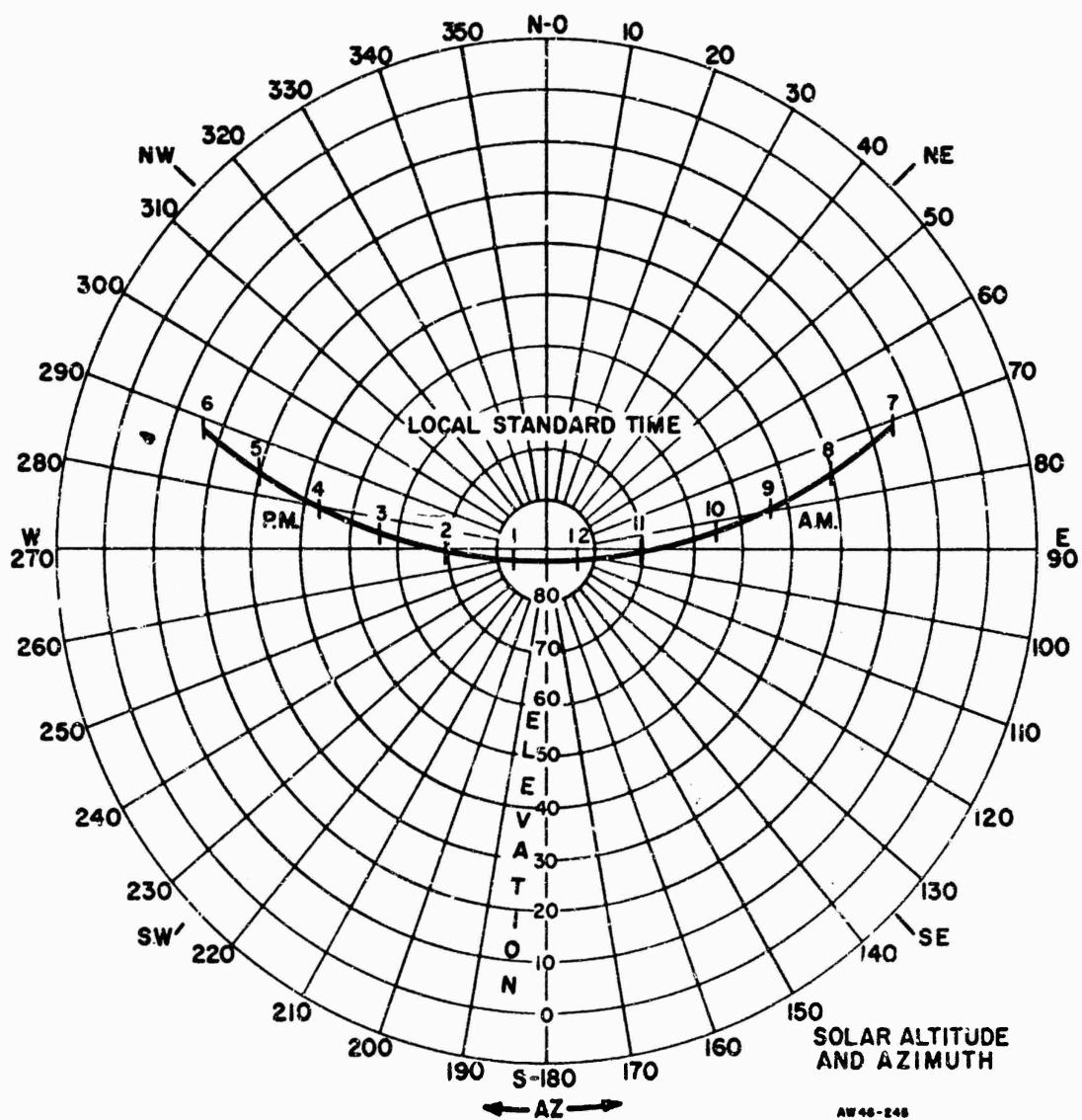


Figure 1. Elevation and Azimuth of the Sun for Key West Local Standard Time.

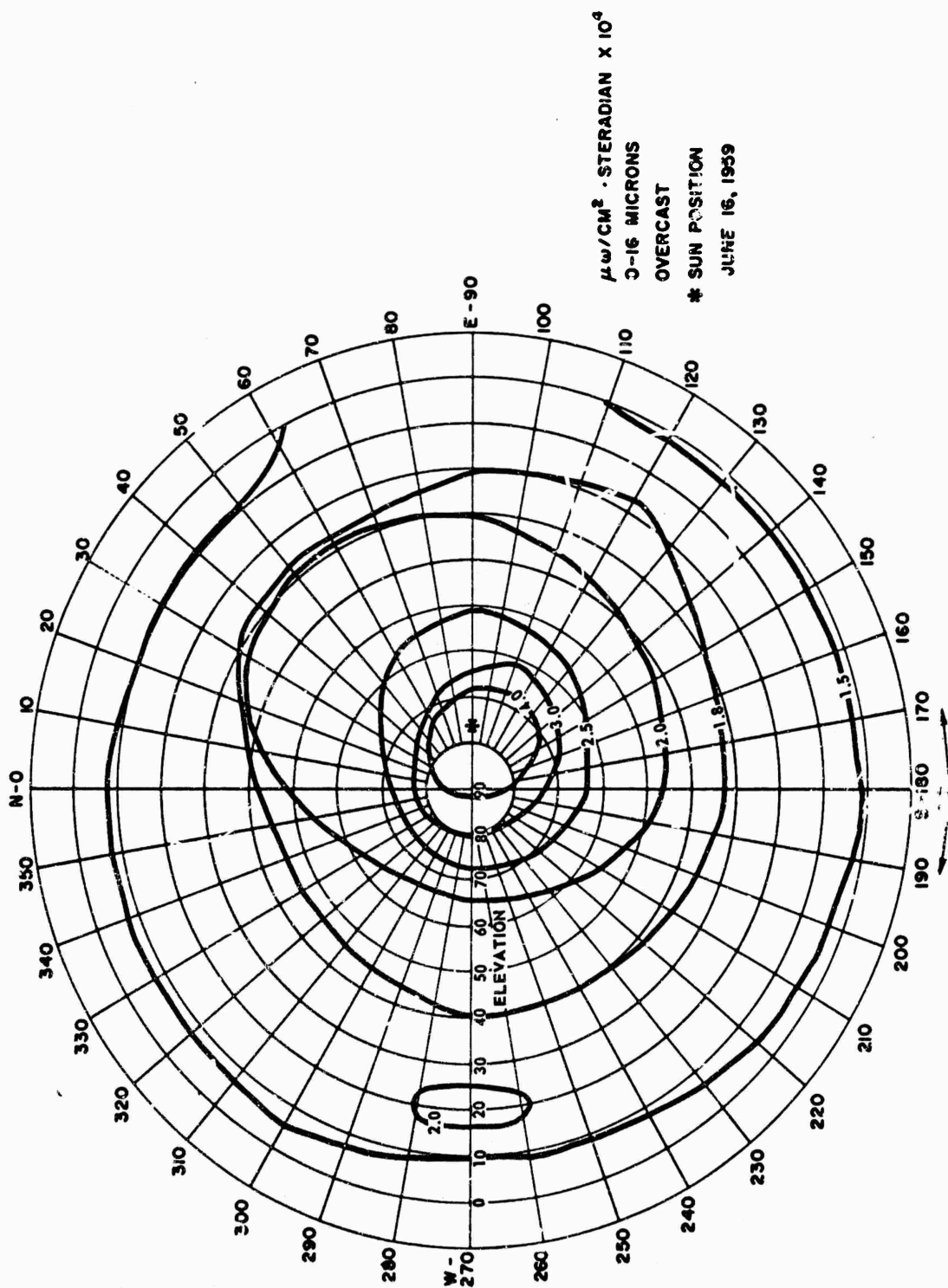


Figure 2. Overcast Sky, June 16, 1959, Key West, 0-16 Microns.

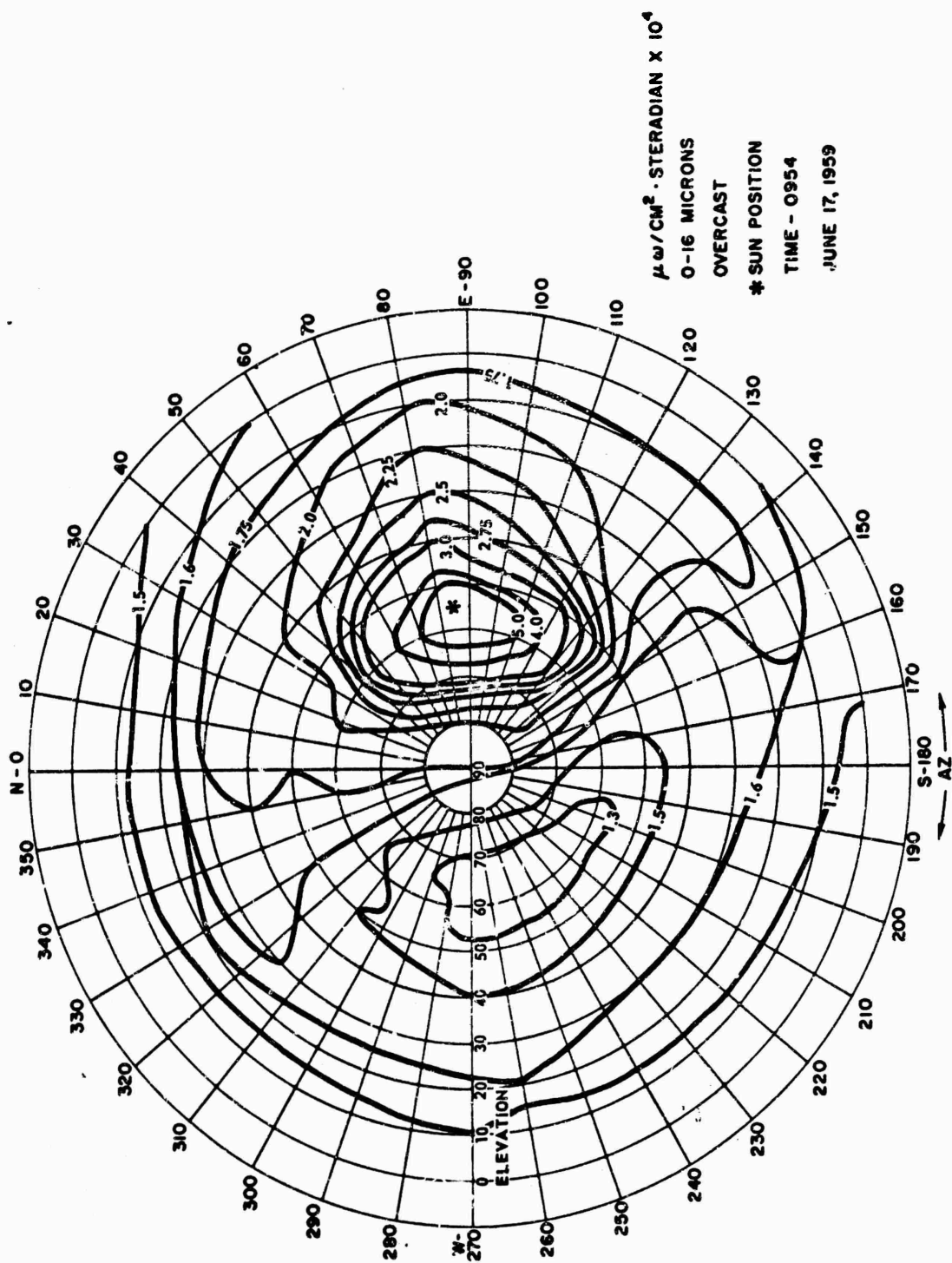


Figure 3. Overcast Sky, June 17, 1959, Key West, 0-16 Microns.

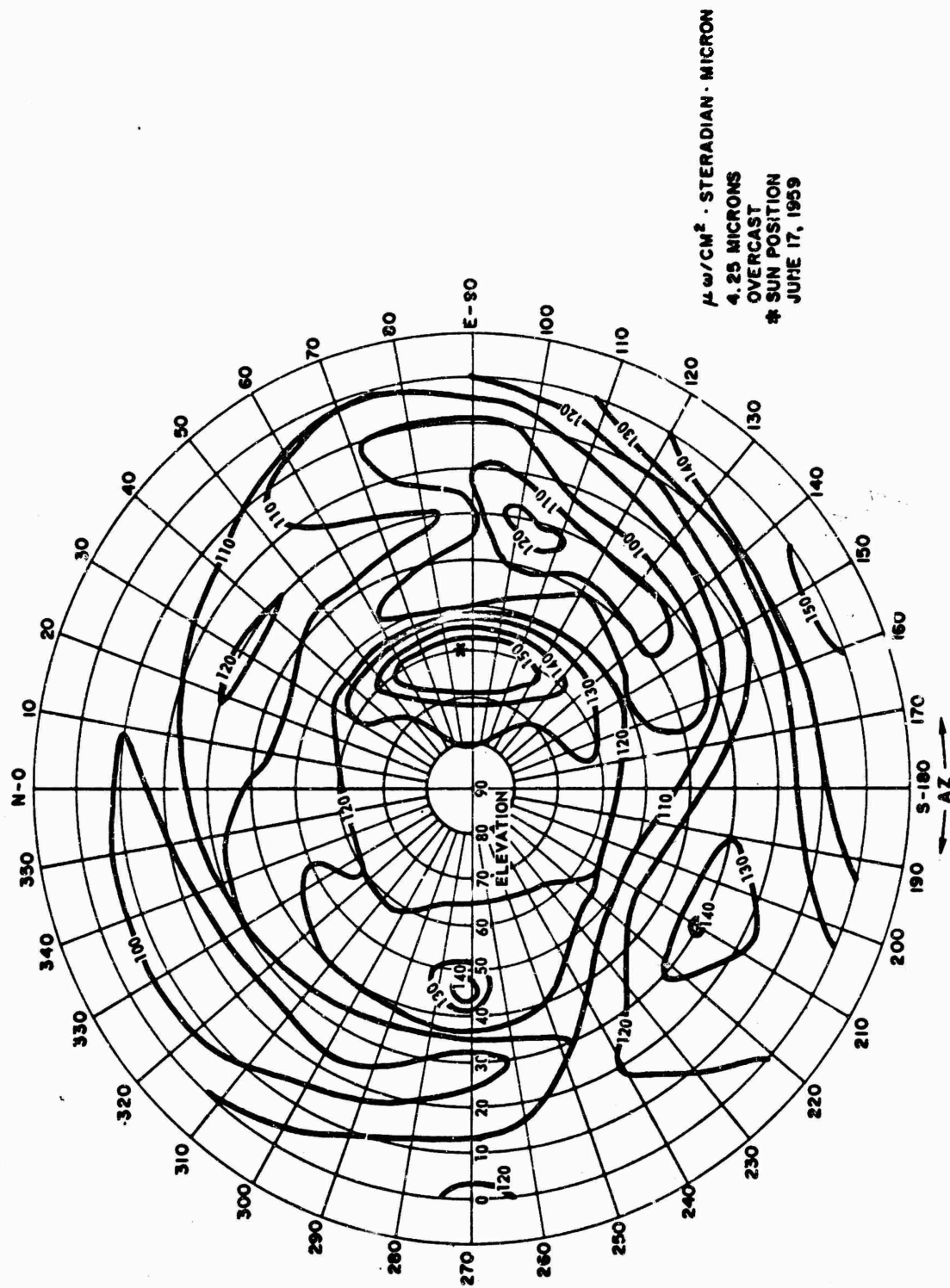


Figure 4. Overcast Sky, June 17, 1959, Key West, 4.25 Microns.

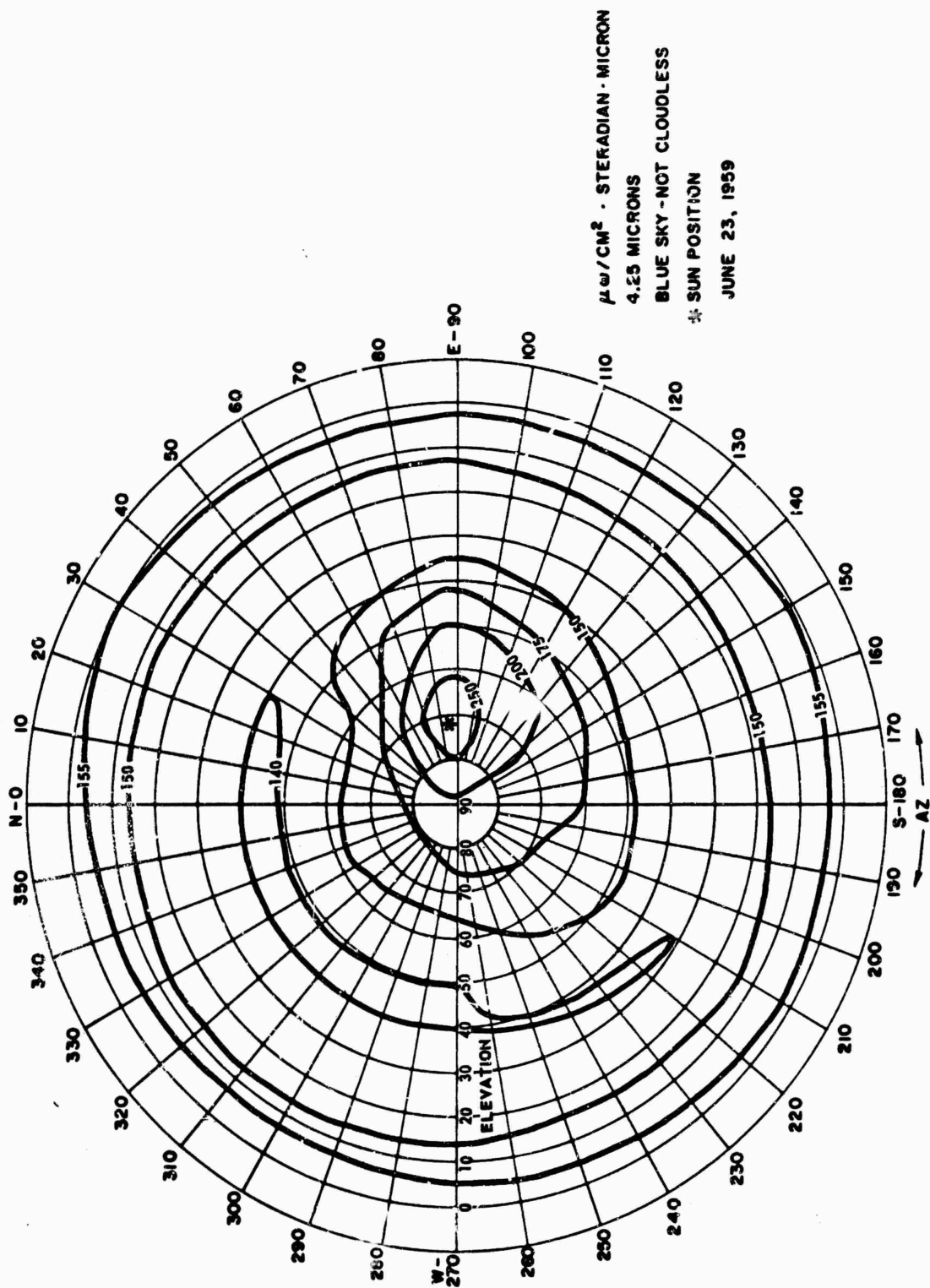


Figure 5. Blue Sky Areas in a Cloudy Sky, June 23, 1959, Key West, 4.25 Microns.

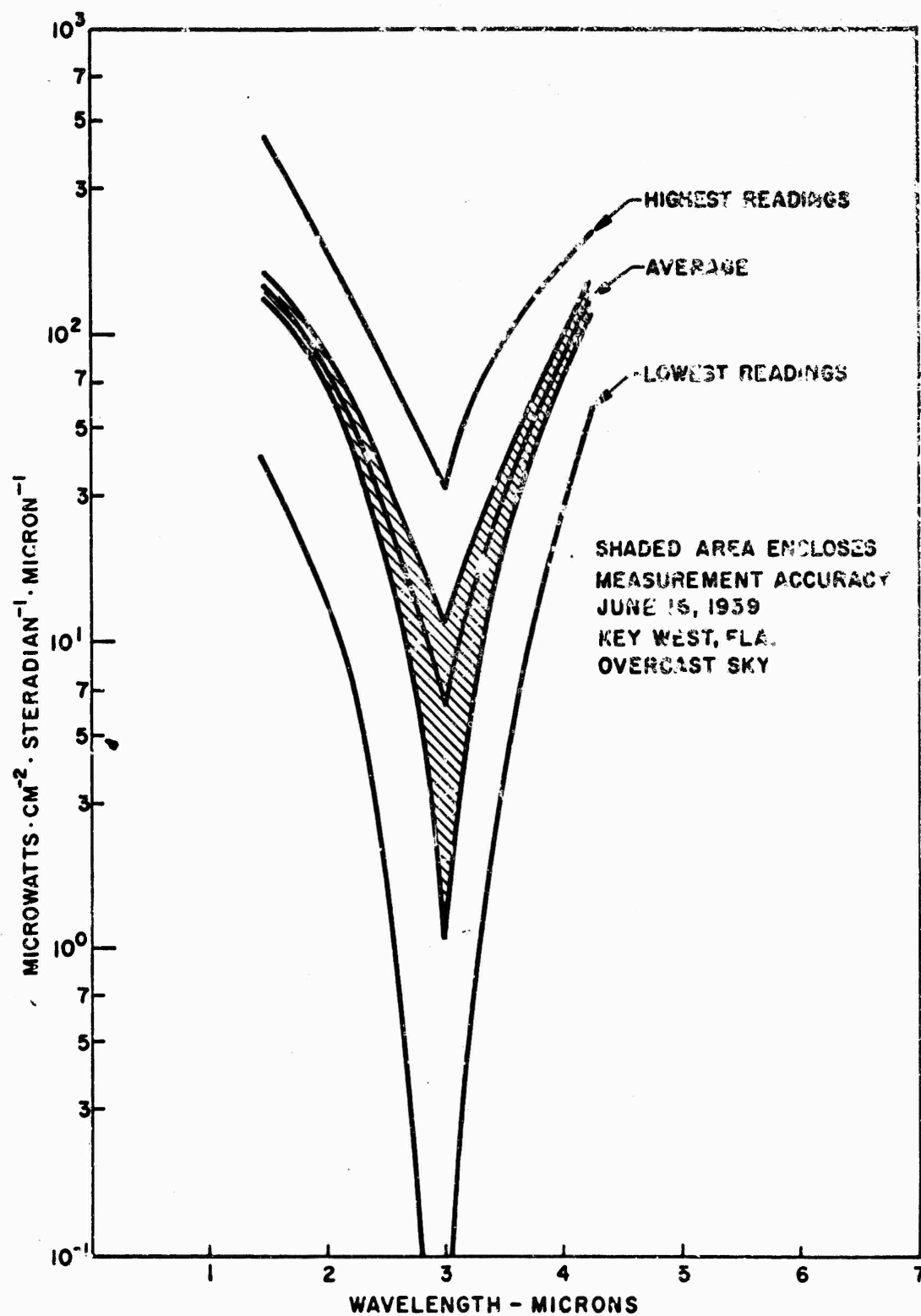


Figure 6. Average Spectral Distribution, Overcast Sky, June 16, 1959.

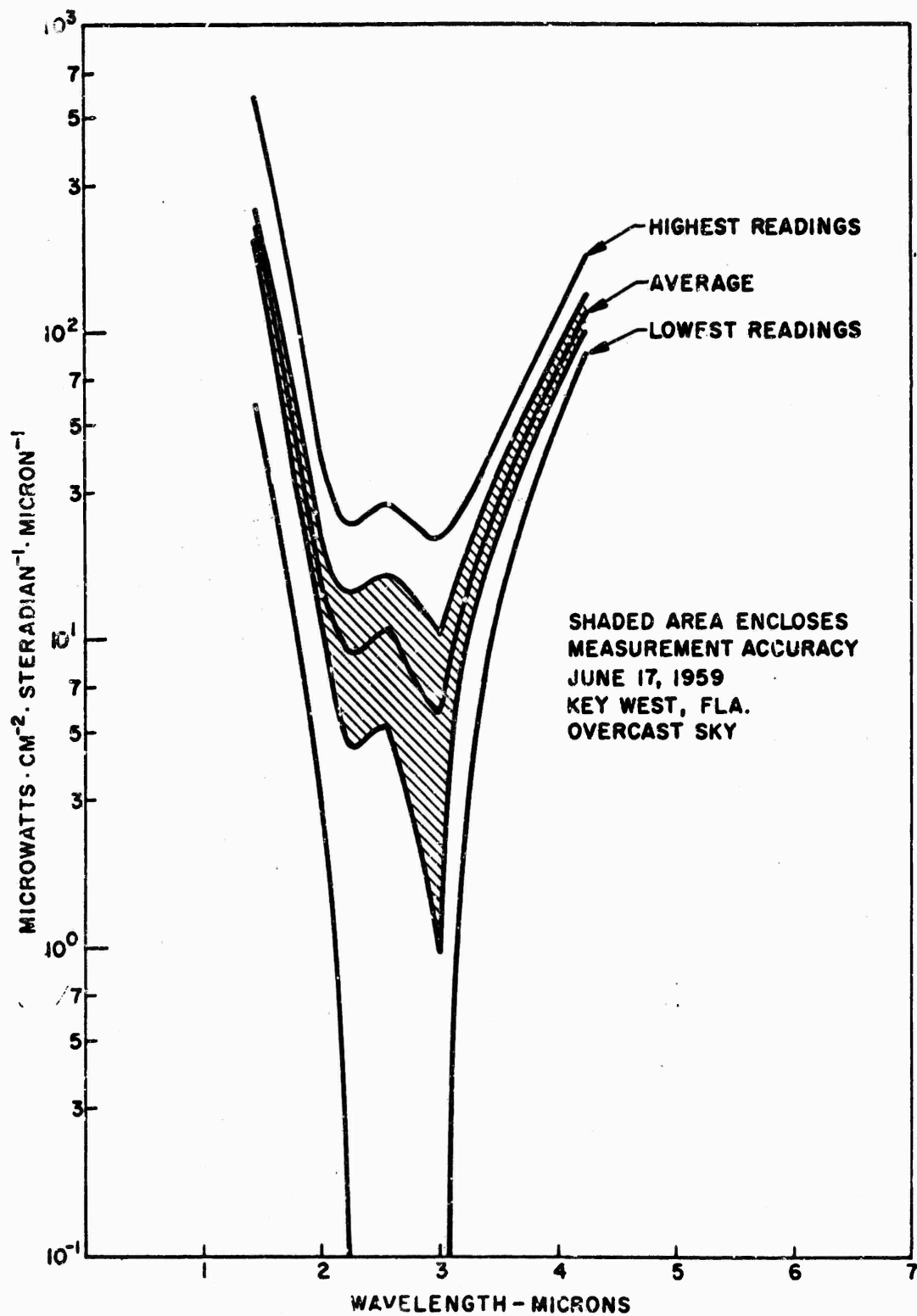


Figure 7. Average Spectral Distribution, Overcast Sky, June 17, 1959.

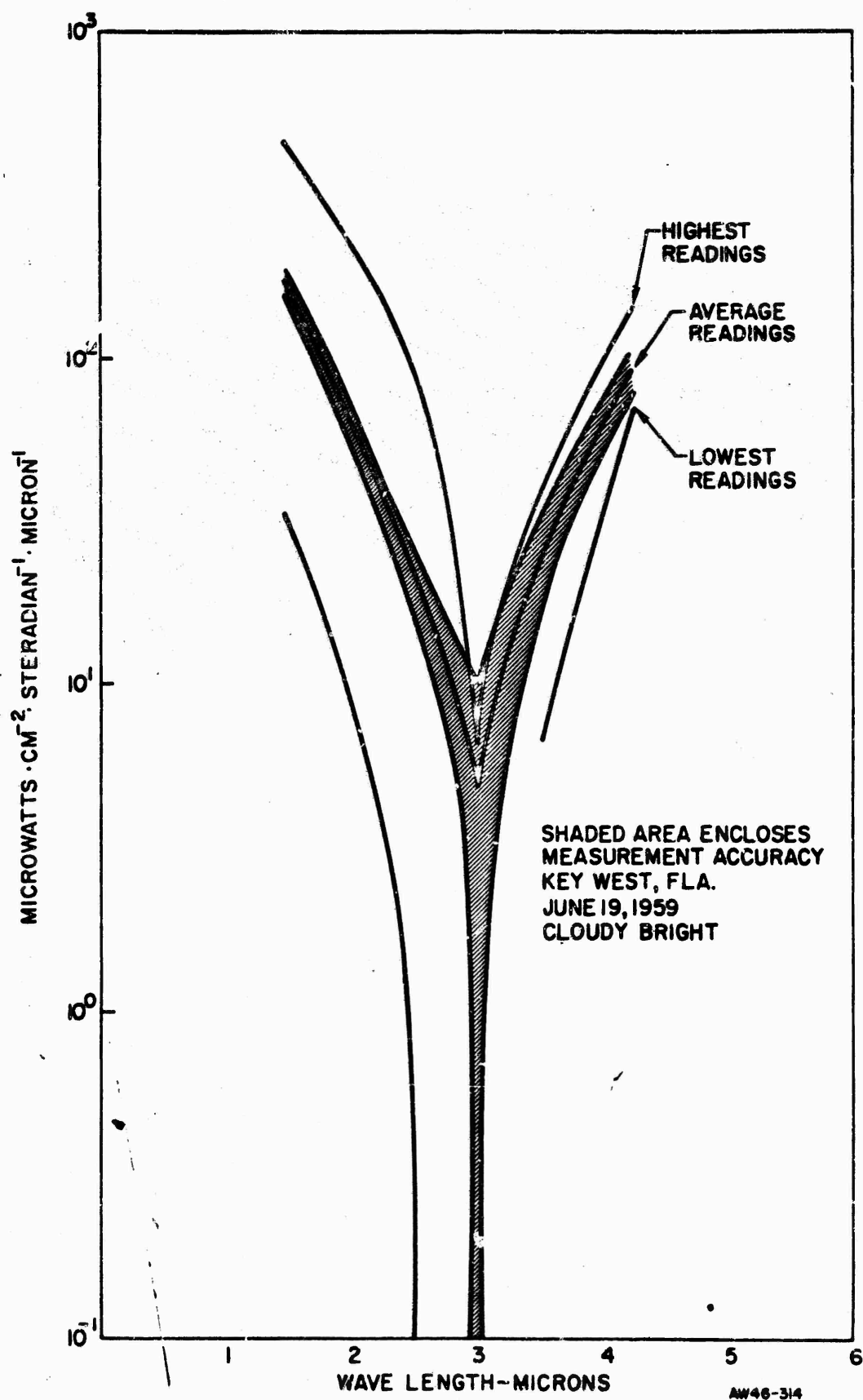


Figure 8. Average Spectral Distribution, Overcast Sky, "Cloudy-Bright", June 19, 1959.

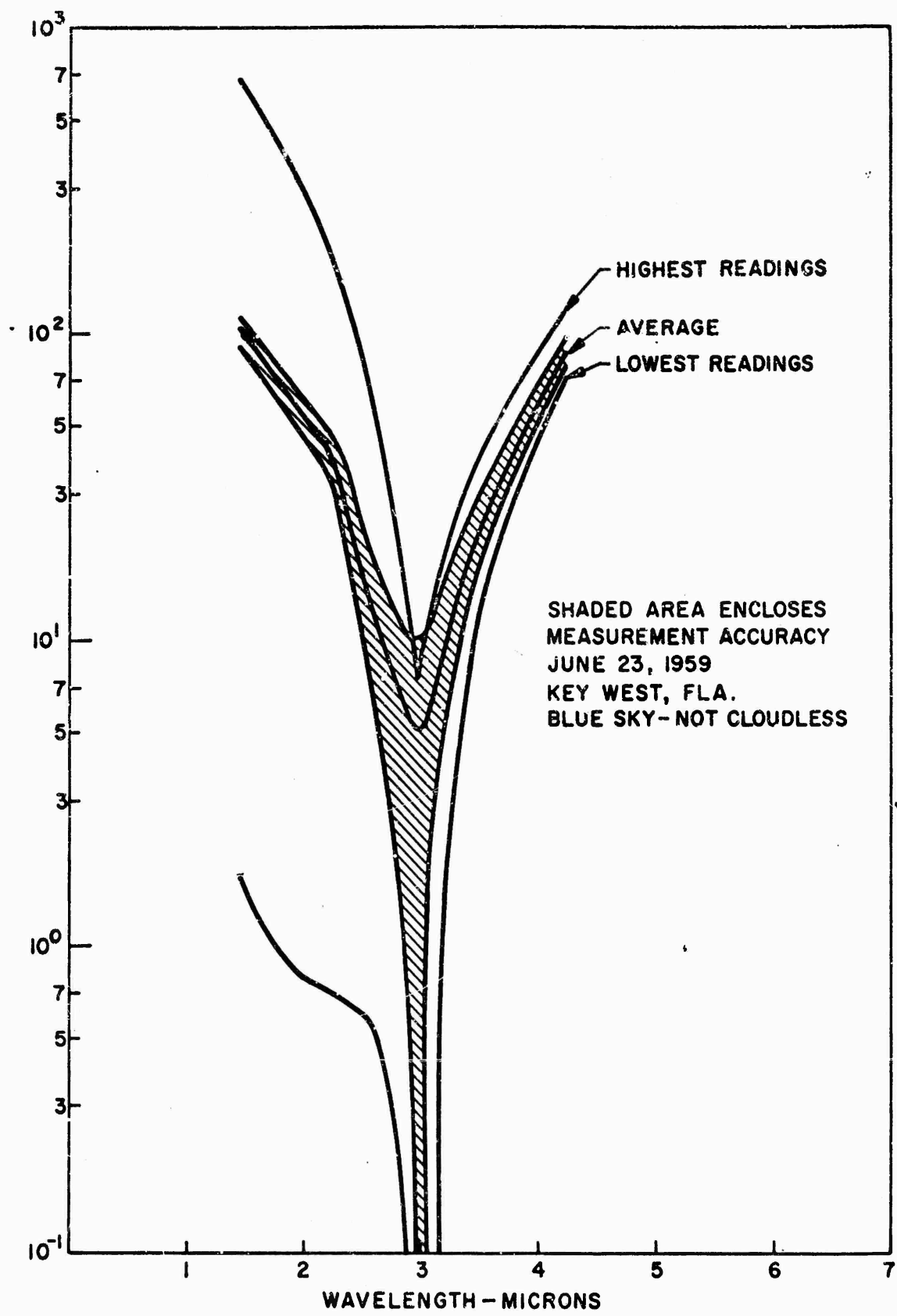


Figure 9. Average Spectral Distribution, Blue Sky Areas in a Cloudy Sky, June 23, 1959.

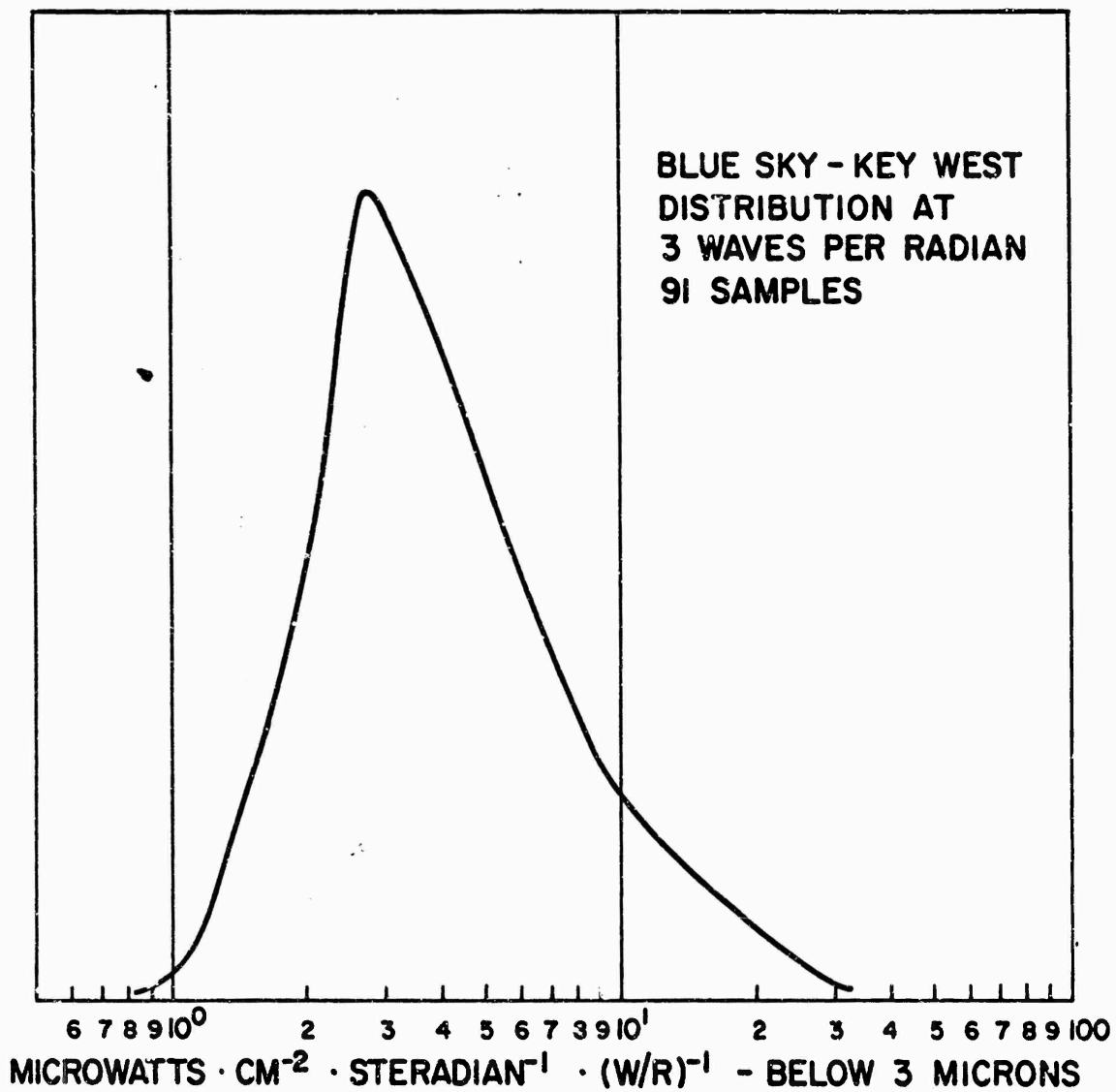


Figure 10. Amplitude Probability for Blue Sky at 3 Waves per Radian.

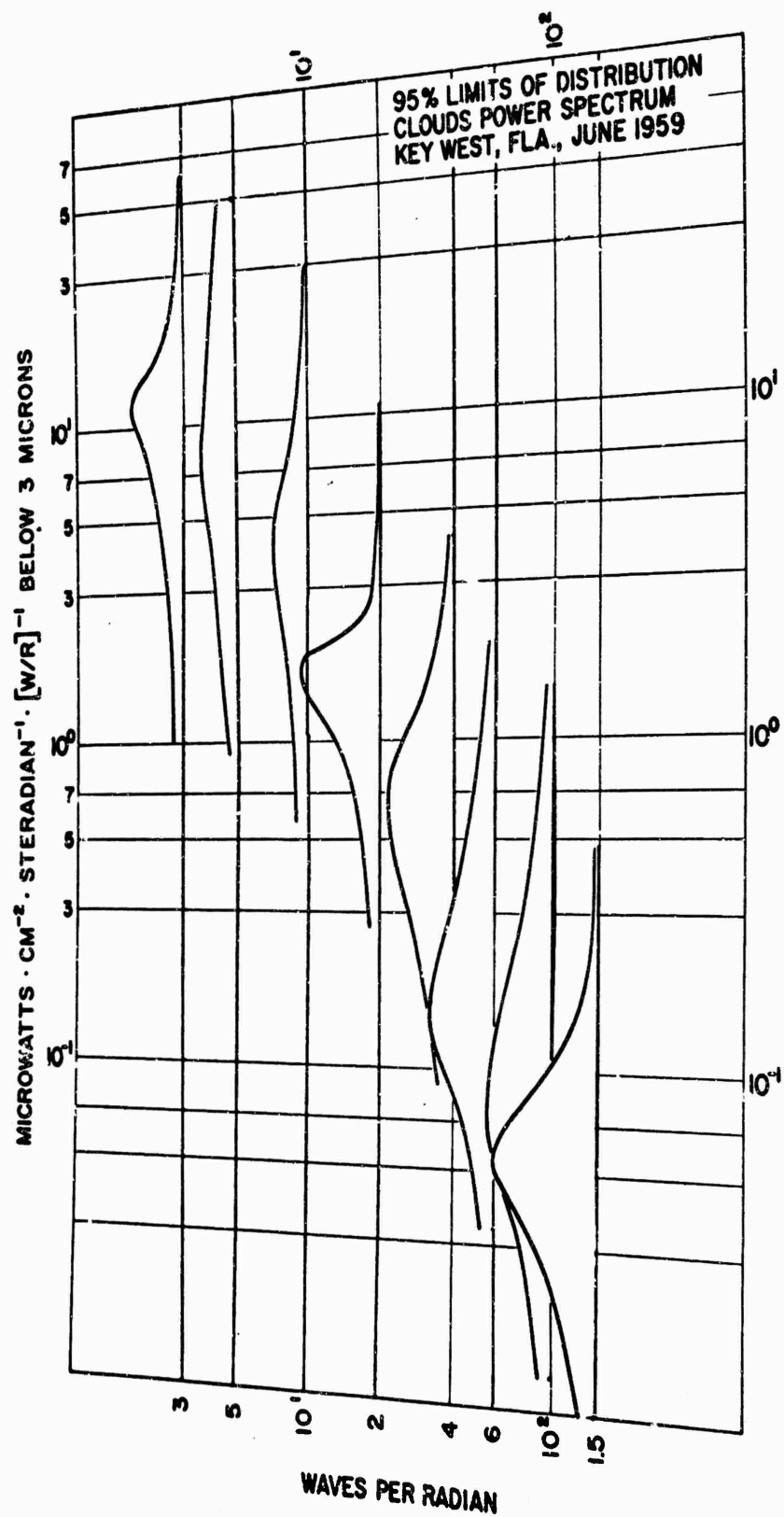


Figure 11. Amplitude Probability for Clouds.

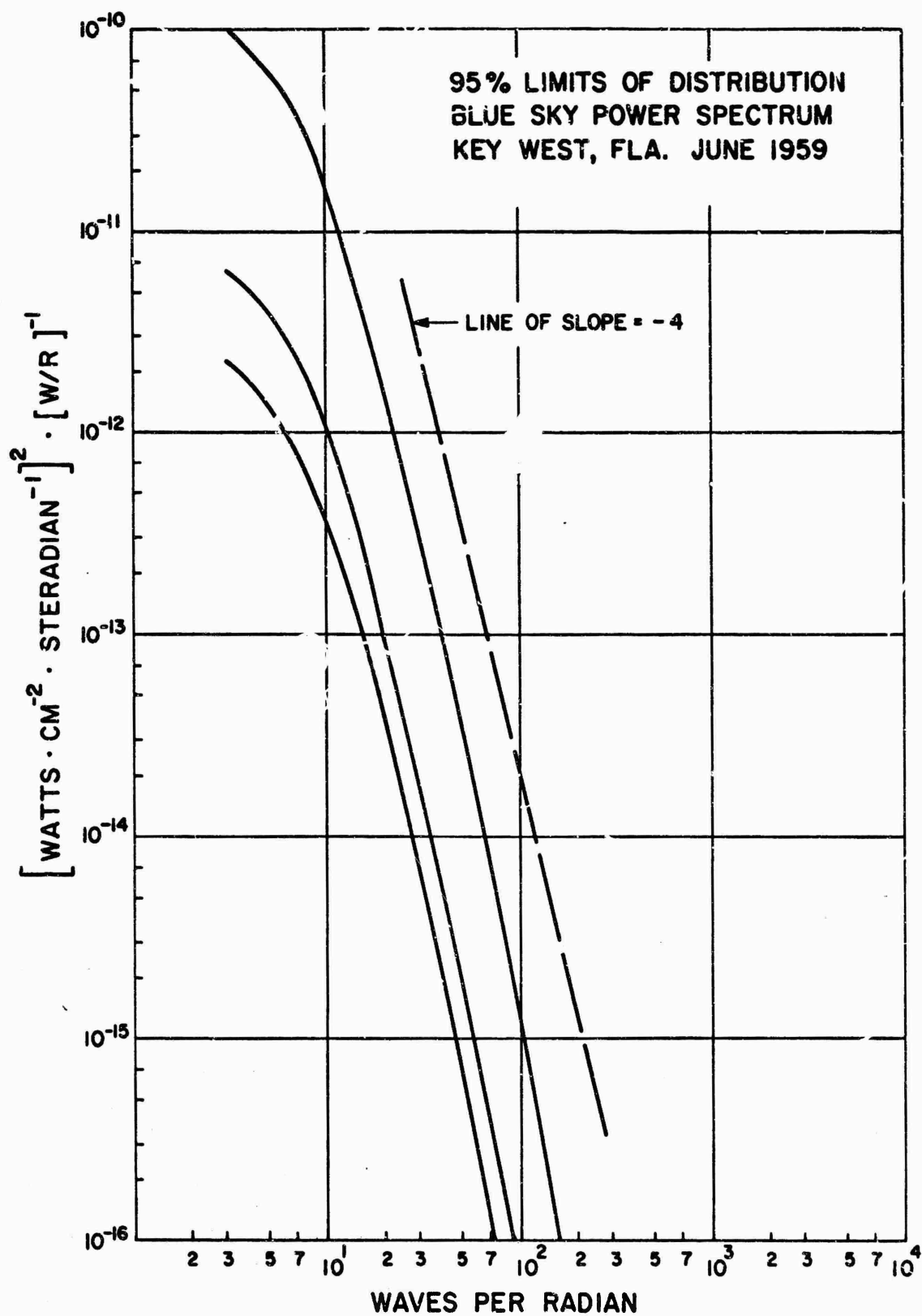


Figure 12. Ninety-Five Percent Distribution Limits for Blue Sky One Dimensional Power Spectrum.

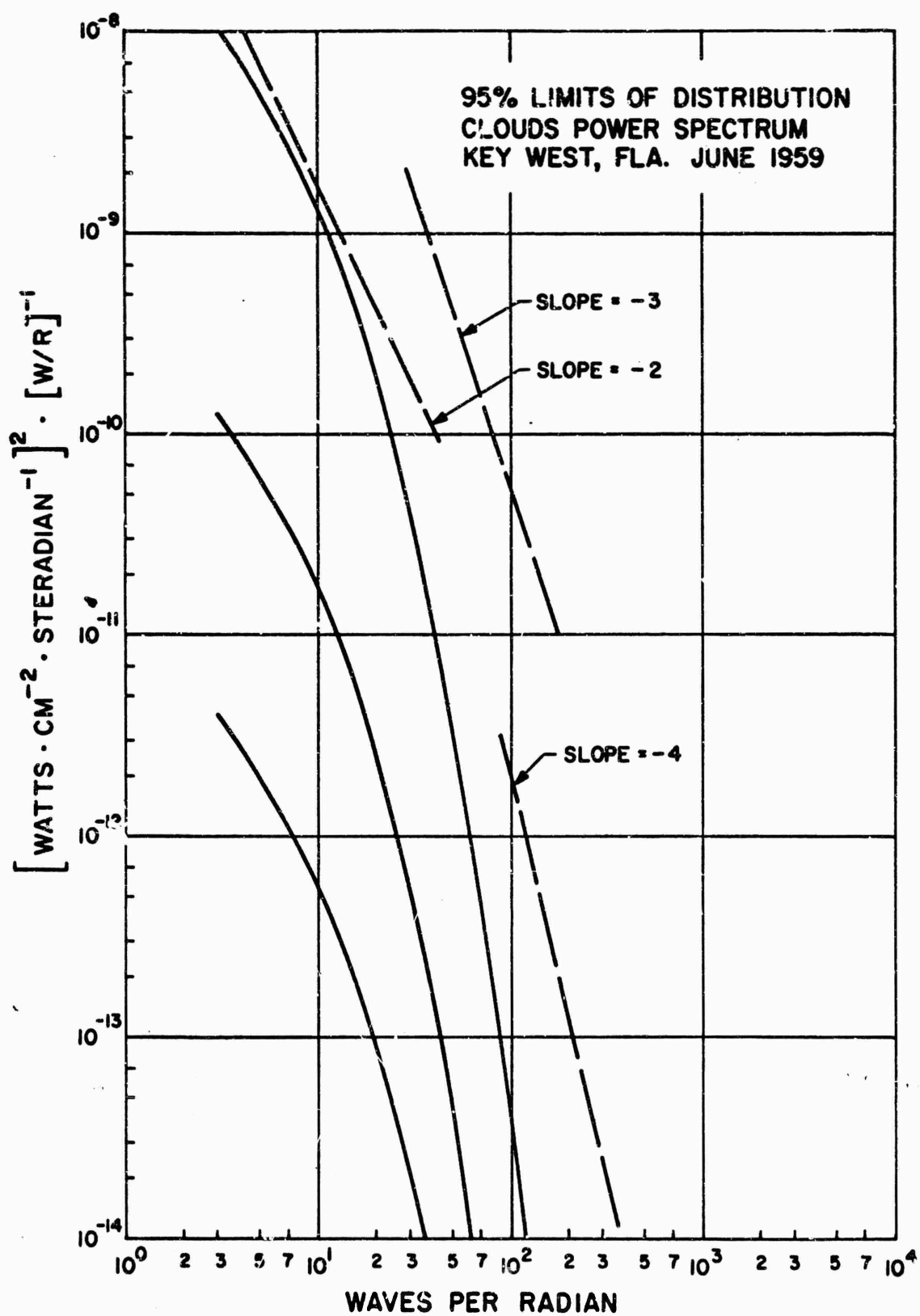


Figure 13. Ninety-Five Percent Distribution Limits for Clouds One Dimensional Power Spectrum.

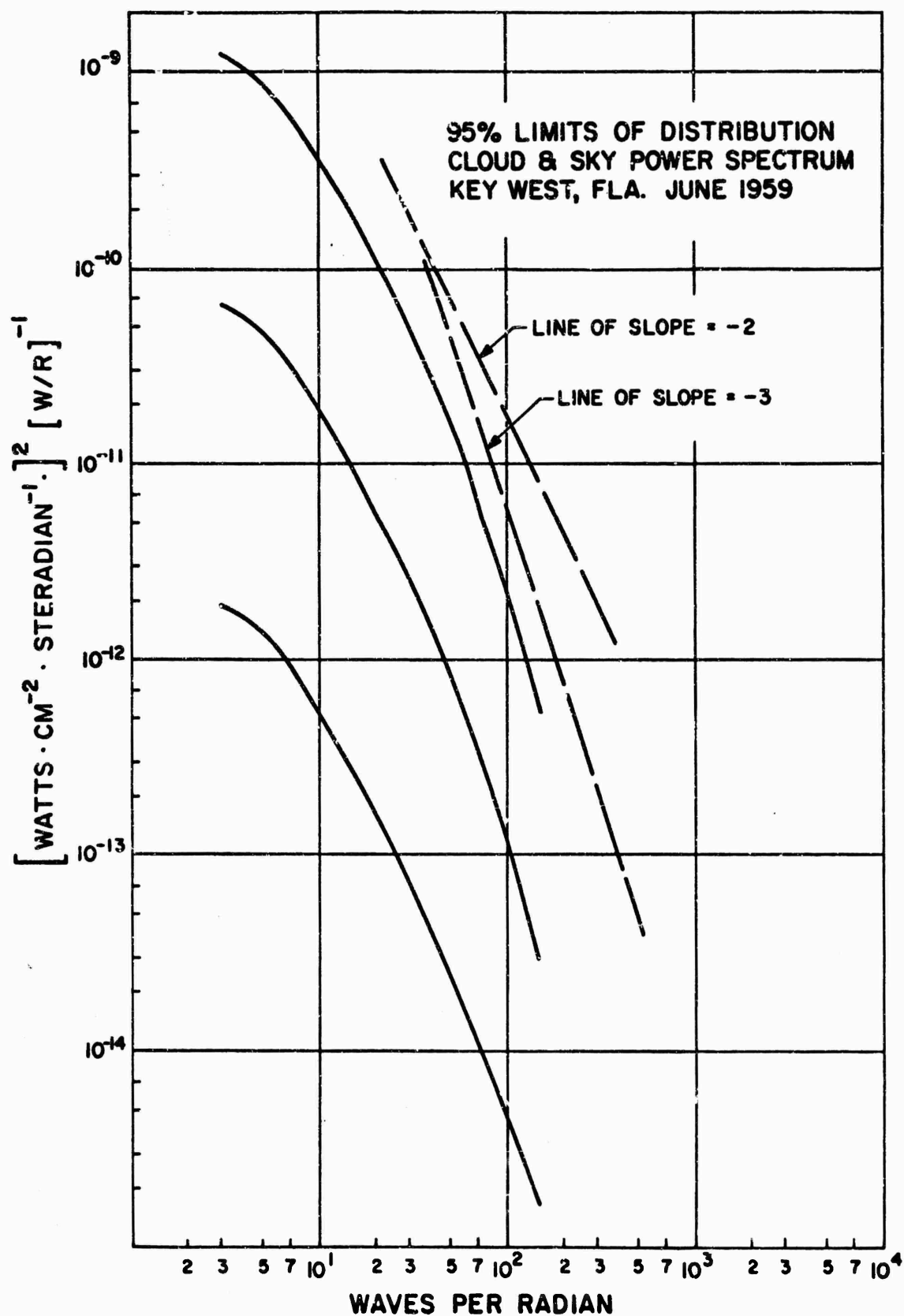


Figure 14. Ninety-Five Percent Distribution Limits for Cloud and Sky One Dimensional Power Spectrum.

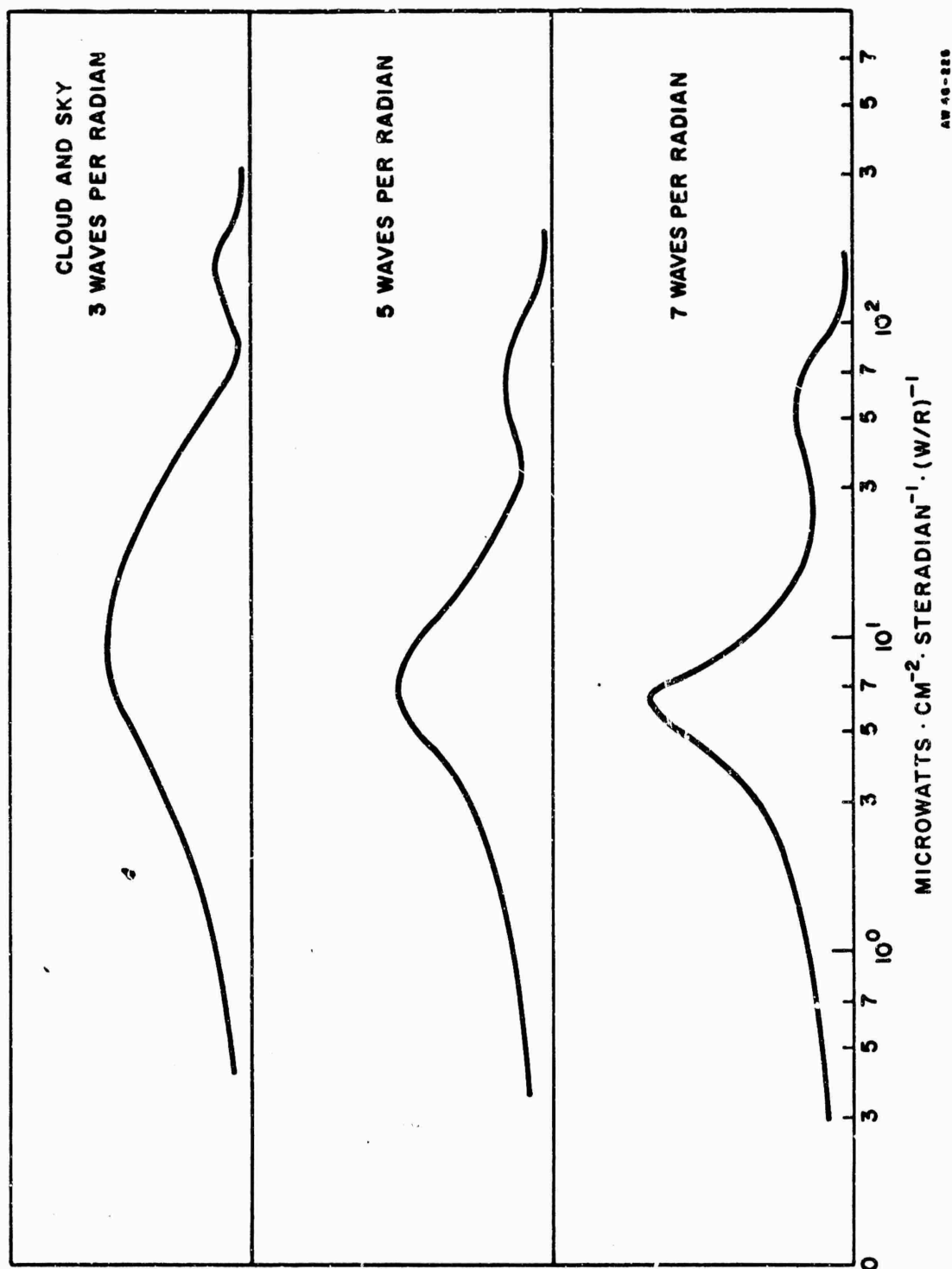


Figure 15. Individual Amplitude Probability Curves-Clouds.

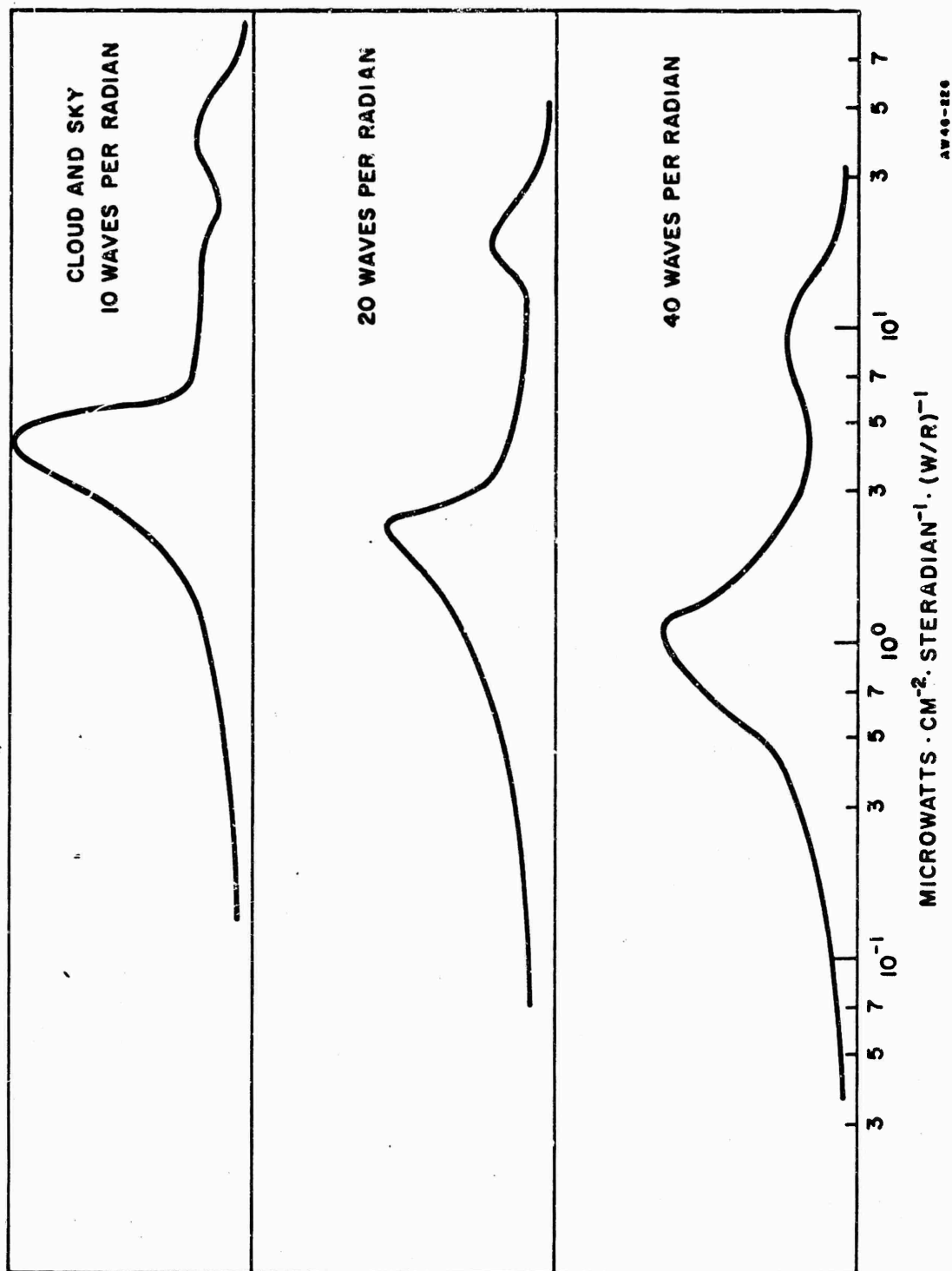


Figure 16. Individual Amplitude Probability Curves - Clouds.

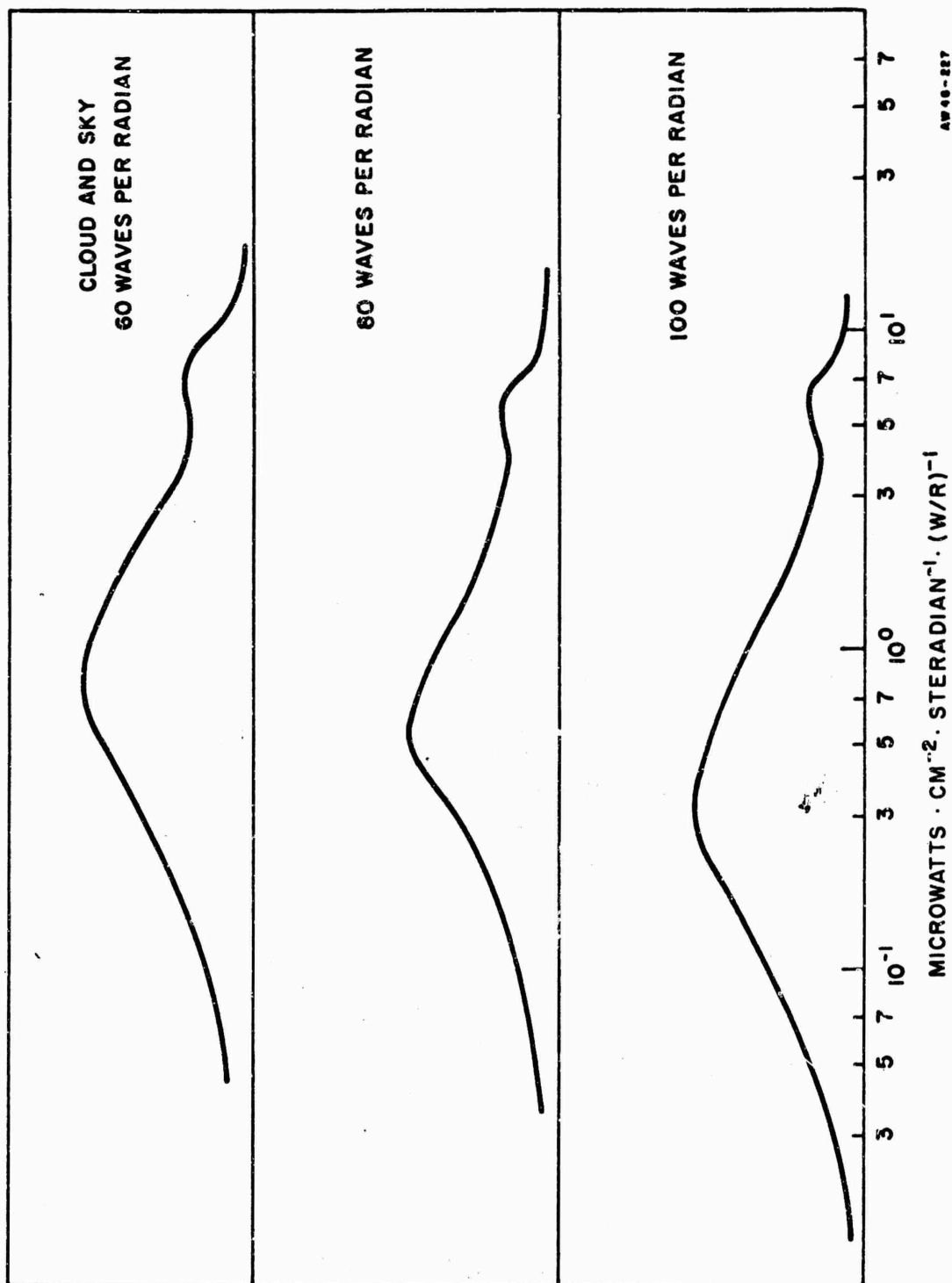


Figure 17. Individual Amplitude Probability Curves - Clouds.

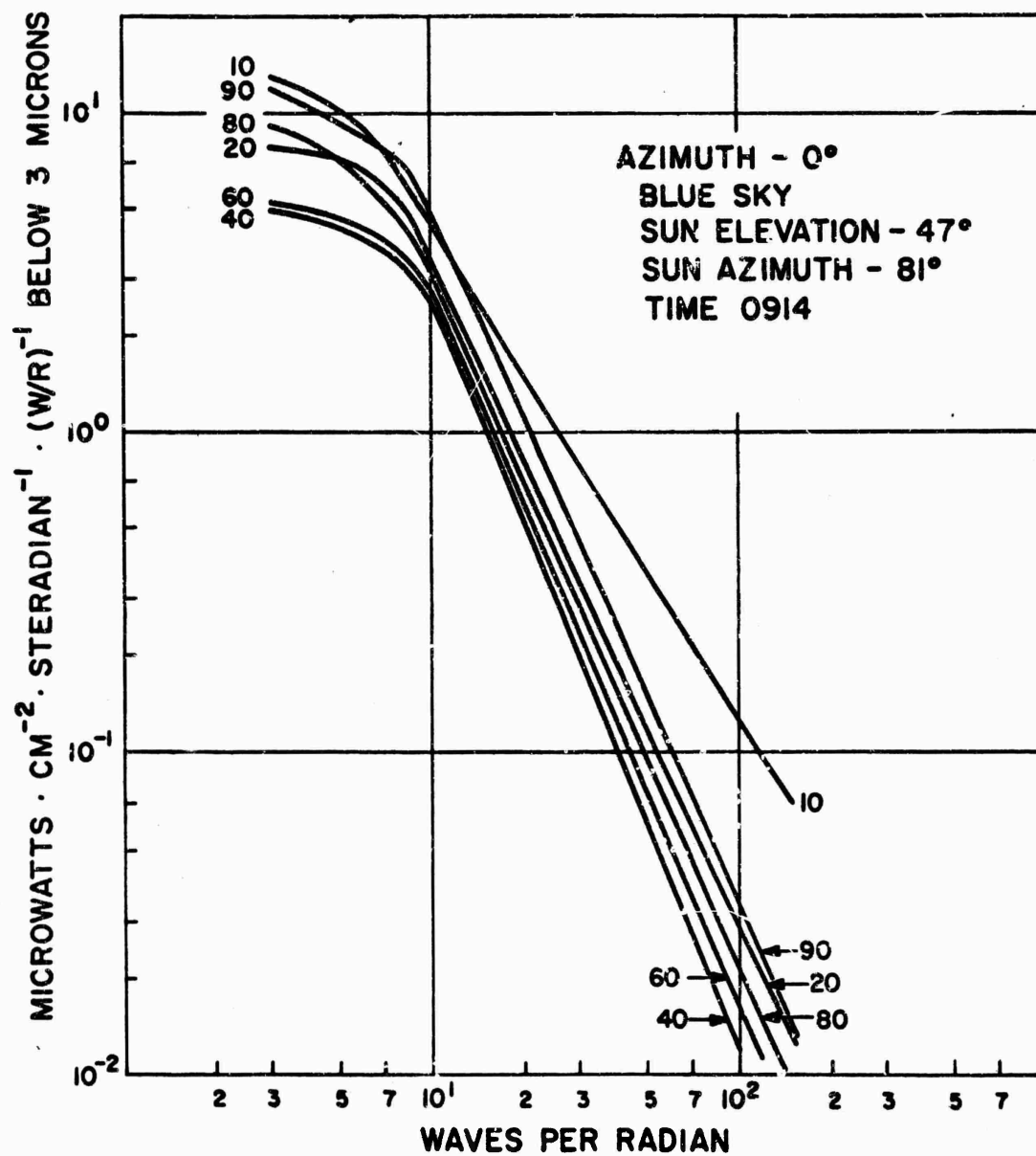


Figure 18. Individual Spectra for Blue Sky for the Azimuth Plane Perpendicular to the Sun Azimuth Plane.

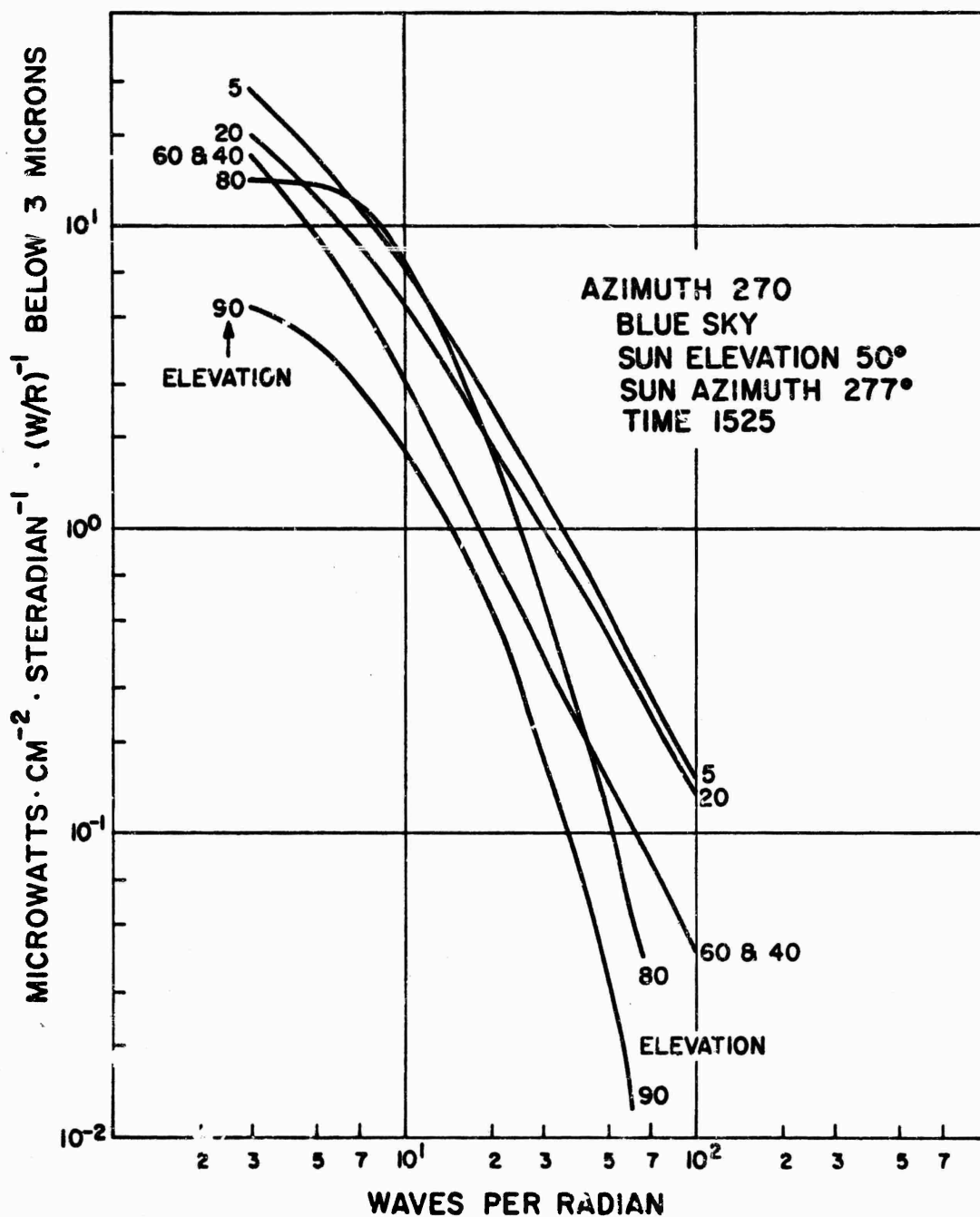


Figure 19. Individual Spectra for Blue Sky for the Sun Azimuth Plane.

INITIAL CONSIDERATIONS UNDERLYING A MODEL

One of the stated objectives of the Key West measurement field trip was to obtain data which might produce a mathematical model for sky brightness. What might be classed as a rigorous mathematical model did not culminate from these data. Sky conditions were widely variant and cloudless sky did not exist during the whole period. Nevertheless, a great amount of effort has been applied to make a beginning attempt and future effort possibly will result in a usable practical model for the infrared sky background. This section of the report discusses, in general fashion, the basic considerations underlying the description of a model. The next section describes some effort to fit the sky brightness values with simple expressions empirically.

Figure 20 depicts a simple model of the earth and its atmosphere. The atmosphere consists of a mixture of permanent gases that exist at a fixed percentage of the total and other gases whose presence is highly variable. The accompanying table summarizes the composition of the atmosphere, neglecting those gases which are present in only small amounts.

Table I

	<u>Constituent</u>	<u>Per Cent</u>
P e r m a n e n t	Nitrogen	78
	Oxygen	21
	Carbon Dioxide	0.033
	Argon	0.93
v a r i a b l e	Water Vapor	0-2
	Ozone	0-.07 p. p. m. (ground level) 1-3 p. p. m. (20-30 KM)

Throughout the troposphere and the stratosphere the permanent gases exist at nearly the same percentage, whereas the water vapor content shows a rapid falloff with increasing height. Although water vapor is generally less than two percent of the atmosphere, it absorbs about six times as much solar radiant energy as all the other gases, and also accounts for almost all the absorption of the earth's radiation.

In addition there are a variety of particles suspended in the atmosphere, which comprise the atmospheric aerosol. Most important are the water droplets and ice crystals of clouds. Other particles include dust, smoke, sea salt particles, and minute organisms such as pollen, spores, bacteria, etc.

The next table indicates the depletion and absorption of incident solar energy under clear skies and cloudy skies, as well as the mean conditions. (The average cloud cover of the earth is 52 percent.)

Table II

<u>Clear Skies</u>	<u>Per Cent</u>
Atmospheric Scattering	9%
Surface Reflection	6%
Total	15%
Absorption by Water Vapor	13%
Absorption by the Other Constituents	3%
Total	16%
Total Depletion	31%
Total Absorption	69%
<u>Overcast Skies</u>	
Reflection and Backscattering	55%
Absorption	10%
Total Depletion	65%
Total Absorption	35%

Table II (Cont'd.)

<u>Mean Conditions</u>	<u>Per Cent</u>
Absorbed through clear skies (.43 x .69)	33%
Absorbed under cloud cover (.52 .35)	18%
Total Incident Energy Absorbed	51%

As far as best observations indicate, the surface of the earth is not undergoing a change in temperature. Therefore, there must be a balance between incident energy and outgoing energy. In the unoccluded portions of the earth, radiation is transmitted through atmospheric "windows" and - in the bands of water vapor and carbon dioxide absorption - energy is radiated to space as blackbody radiation at the temperature of the stratosphere. When the sky is overcast the only emission is at the blackbody temperature of the stratosphere. It is known that these effects vary over the surface of the earth, with season, latitude, region, time, etc. As a simplification of an extremely complex process, the earth will be assumed to be uniform, i. e., each area will be assumed identical with equal probability of being occluded. The next table presents a summary of the earth-atmosphere-solar radiation heat balance. It is assumed that 100 units of radiation are incident upon the atmosphere. (5)

<u>SOLAR (Space) BALANCE</u>		
<u>IN</u>	<u>OUT</u>	
100 units	Solar Radiation scattered upward	9
	Reflected Solar Radiation	27
	Emitted Radiation from Absorbing Transparent Region	47
	Emission from the Earth in the Transparent Region	<u>17</u>
		100

EARTH SURFACE BALANCE

<u>IN</u>		<u>OUT</u>	
Direct Solar Radiation	32	Emission from the earth in atmospheric absorption regions.	120
Solar Radiation scattered downward.	19	Heat carried to the atmosphere in the hydrological cycle.	23
Infrared emission from the atmosphere.	106	Emission from the earth in transparent regions.	17
Heat transported down by eddy currents.	3		
	<hr/> 160		<hr/> 160

ATMOSPHERIC BALANCE

<u>IN</u>		<u>OUT</u>	
Earth emission in absorbing regions	120	Infrared emission to space.	47
Heat carried to the atmosphere in the hydrological cycle.	23	Infrared emission to the earth.	106
Solar radiation absorbed.	13	Heat transported downward by eddy currents.	3
	<hr/> 156		<hr/> 156

The foregoing relations delineate the gross phenomena of the model. Subsequent paragraphs will discuss in detail some of the important processes.

ABSORPTION

Figure 21 presents typical absorption spectra of the gases important in the absorption process of the atmosphere. (The scales are in terms of transmission; the upper limit being 100 percent transmission, the lower limit 0 percent transmission or total absorption.) The solar spectrum is included as a reference. It can be seen that the product of the three transmission curves for the gases considered closely approximates the solar spectrum, indicating that they are

the only gases that need be considered in a simple model. The model indicates that in the lower atmosphere only water vapor and carbon dioxide need be considered, and that ozone is the first gas to effect solar radiation. Since the concentration of ozone is very low at low altitudes, and only one percent of the atmosphere lies above the ozone band, these approximations should not introduce significant errors. In the region between the earth and the ozone band, the role of carbon dioxide becomes more important with increasing altitude. Near ground level, as has been indicated, water vapor accounts for the majority of the absorption, however, its concentration falls off rapidly with altitude, whereas the partial pressure of carbon dioxide relative to the total pressure is essentially constant.

Howard, Burch, and Williams⁽⁶⁾ discuss the problem of absorption by water vapor and carbon dioxide in considerable detail. After a series of measurements of the absorption of these gases at various pressures and with various path lengths, it was found that two types of empirical relationships were sufficient to represent the total absorption of any band in the 0.9μ to 15μ region:

$$\int A_v dv = cw^{1/2} (P + p)^k \quad (\text{weak absorption bands})$$

$$\int A_v dv = C + D \log_{10} w + K \log_{10} (P + p) \quad (\text{strong absorption bands})$$

where $\int A_v dv$ = the total absorption of a band

w = total absorber concentration (atom-cm for CO_2 ,
pr. cm for H_2O)

P = the total pressure

p = the partial pressure of the absorber.

c, k, C, D, K = constants for a given band.

The reference contains tabulations of the constants in the above relationships. For a particular absorption band, there is a value of total absorption below which the "weak" relationship holds, and above which the "strong" relationship is applicable.

There have been two simple theoretical models created to explain the observed absorptions by water vapor and carbon dioxide; the Elsasser Model and the Goody Model. It has long been realized that a spectral "line" must have some finite width because of broadening. For H_2O and CO_2 , under the temperature and pressure of the lower atmosphere, the finite widths of the spectral lines are due to molecular collisions. For a Lorentz-shaped line, which is the shape appropriate to the model atmosphere, the absorption coefficient, k_v is:

$$k_v = \frac{S}{\pi} \frac{\alpha}{(v - v_0)^2 + \alpha^2}$$

where

S = line strength

α = half width at maximum

v = frequency

v_0 = center frequency

The line intensity S , is essentially independent of temperature and α is a function of temperature, T , and pressure, P .

$$\alpha = \alpha_0 \frac{P}{P_0} \sqrt{\frac{T_0}{T}}$$

where the subscript refers to the values at standard conditions.

The detailed structure of a CO_2 band is a fairly regular, approximately evenly spaced, sequence of absorption lines, where adjacent lines have nearly equal intensity. In contrast, an H_2O band consists of many irregularly spaced lines of very unequal intensities.

Elsasser treated the case of an idealized band consisting of an infinite number of equally intense, equidistant Lorentz-shaped lines. For this case the absorption coefficient - assuming lines at $v = 0, \pm 2d, \pm 4d, \dots$ is

$$kv = \sum_{n=-\infty}^{\infty} \frac{S}{\pi} \frac{\alpha}{(v - nd)^2 + \alpha^2}$$

Letting $a = \frac{2\pi v}{d}$ and $b = \frac{2\pi\alpha}{d}$

$$kv = \frac{S}{d} \frac{\sinh b}{\cosh b - \cos a}$$

If the incident energy is constant throughout the spectrum, the absorption A, is:

$$A = \frac{1}{2\pi} \int_{-\pi}^{\pi} (1 - e^{-k(a)w}) da$$

If the line spacing, d, is large compared to the half-width, α , then:

$$kv = k(a) = \frac{Sb}{2d \sin^2\left(\frac{a}{2}\right)}$$

and $A = \operatorname{erf} \sqrt{\frac{\pi S \alpha w}{d^2}}$ where $\operatorname{erf}(x) = \frac{2}{\pi} \int_0^x e^{-t^2} dt$

The average absorption is $A = \operatorname{erf} \sqrt{\frac{l w}{2}}$ where $l = \frac{2\pi \alpha S}{d^2}$

For a frequency interval which contains several approximately equally intense, equidistant lines, where there is no absorption at the center of the band from lines outside the interval:

$$A_c = \operatorname{erf} \sqrt{\frac{l_o w}{2}}$$

The absorption bands of CO_2 are sufficiently regular to satisfy the requirements. Thus the Elsasser model should apply to CO_2 . Experiments have demonstrated that there is good agreement between measured and predicted absorption.

Goody developed a statistical or random model for a disordered band, which has been shown to fit H_2O absorption quite well. He considers the fractional transmission at the center of a frequency interval nS wide where n is the number of lines of Lorentz shape in the interval, and δ the mean line spacing. The line spacings are assumed to be random, and the line intensities which are uncorrelated with position, are assumed to follow the distribution law $P(S) = (1/\sigma) e^{-S/\sigma}$.

With these assumptions, it is possible to show that the transmission at the center frequency of a thickness w of absorbing gas is:

$$T(\alpha, w_c) = \exp \left[\frac{-w \sigma \alpha}{\delta(\alpha^2 + \frac{w \sigma \delta}{\pi})^{1/2}} \right]$$

Howard, Burch, and Williams chose to represent the variation of σ over a band by the relation $\sigma = k/w_0$. Then, letting $\beta = k/\delta$ and $\gamma = k/\pi\alpha$

$$T = \exp \left[- \frac{\frac{w}{w_0} k \alpha}{\delta \left(\alpha^2 + \frac{(w/w_0) k \alpha}{\pi} \right)^{1/2}} \right] = \exp \left[- \frac{(w/w_0) \beta}{\left[1 + (w/w_0) \gamma \right]^{1/2}} \right]$$

Values of the parameters β and γ were determined from experimental data, and a final result obtained.

$$T = \exp \left[- \frac{1.97 w/w_0}{\left[1 + 6.57 w/w_0 \right]^{1/2}} \right]$$

where w_0 is absorber concentration required to drop the transmission to 50 percent at a given frequency. This relation was found to fit all the H_2O bands considered in the referenced report.

SCATTERING

In addition to absorption by the atmospheric gases, energy incident upon the unoccluded atmosphere is scattered by the air molecules and by the atmospheric aerosol.

For "clear" air, i. e. , assuming that there are no clouds or haze particles present, the Rayleigh theory of scattering by air molecules as extended by Tousey and Hulburt⁽⁷⁾ can be used to calculate the amount of both primary and multiply scattered energy reaching an observer. Because the referenced report contains an extensive development of the theory, it will only be summarized here. Their notation is as follows:

1. ζ , the zenith angle of the sun.
2. ξ , the zenith angle of observation
3. ϑ , the scattering angle.
4. Z , projection of ϑ in the horizontal plane.
$$\cos \vartheta = \cos \zeta \cos \xi \pm \zeta \sin \xi \cos Z$$
5. $i_{o\lambda}$, intensity of sunlight outside the atmosphere as a function of wavelength, λ
6. δ , the polarization defect - the ratio of the weak to the strong polarized component of sky light at $\vartheta = \pi/2$
(It is assumed to have the value $\delta = 0.04$)
7. r , diffuse earth reflectivity (abedo). (An average value of 0.20 is assumed for model earth)
8. μ_λ , index of refraction for air - function of wavelength.
9. n , the molecular density of the clear atmosphere (molecules/cm³)
10. x , thickness of the atmosphere above the point of observation, reduced to NTP.

Scattered light reaching an observer consists of light scattered directly (primary scattering) and light which is scattered more than once (multiple scattering). The total observed is the sum of the

primary scattered, $i_{p\lambda}$, and the multiply scattered, $i_{m\lambda}$, light. In the infrared at wavelengths outside the ozone absorption band (9.6μ), the expressions are somewhat less complicated than in the original statement. The total scattered intensity is $i_{t\lambda}$.

$$i_{t\lambda} = i_{p\lambda} + i_{m\lambda}$$

$$i_{p\lambda} = \frac{3}{4\pi} i_{o\lambda} \exp(-\beta_{\lambda} \sec \zeta) \left[\frac{1 + \frac{1-\delta}{1+\delta} \cos^2 \phi}{3 + \frac{1-\delta}{1+\delta}} \right]$$

$$i_{m\lambda} = \frac{1}{8\pi} (a_i + b_i + b_o) \left[\frac{e^{-\beta_{\lambda} x_i \sec \zeta} - e^{-\beta_{\lambda} x_i \sec \xi}}{1 - \sec \zeta \cos \xi} \right] \left(1 - e^{-\beta_{\lambda} x_i \sec \xi} \right)$$

where β_{λ} = modified Rayleigh scattering coefficient.

$$= \frac{8\pi^3}{3} \left[\frac{(\mu_{\lambda} - 1)^2}{\eta \lambda^4} \right] \left[\frac{6(1+\delta)}{6-7\delta} \right] \left[3 + \frac{1-\delta}{1+\delta} \right]$$

$$a_i = \frac{i_{o\lambda} \cos \zeta}{1 + gt} \left[(1 + gt) (c - cx) - g x_i (c - cT + T) \right]$$

= intensity of multiply scattered beam moving downward at

$$b_i = \frac{i_{o\lambda} \cos \zeta}{1 + gt} \left[(1 + gt) (c - cx + x) - (g x_i + \tau) (c - cT + T) \right]$$

= intensity of multiply scattered beam moving upward at

b_o = intensity of multiply scattered beam moving upward at top of the atmosphere.

$$g = (1 - r) (1 - \eta) \beta_{\lambda} \quad (\eta = 1/2 \text{ for Rayleigh atmosphere})$$

$$c = \eta + (1 - \eta) \cos \zeta$$

$$x = e^{-\beta_{\lambda} x \sec \zeta}$$

$$T = e^{-\beta_{\lambda} t \sec \zeta} \quad (t = \text{total thickness of atmosphere at NTP})$$

Because of the $\cos^2 \theta$ term, the scattering should be maximum in the direction of the incident light ($\theta = 0^\circ$) and in the opposite direction ($\theta = 180^\circ$) and a minimum in the plane at right angles to the incident light ($\theta = 90^\circ$). The polarization of the light should be complete in this plane and zero at $\theta = 0^\circ$, $\theta = 180^\circ$. In practice - because of multiple scattering, the polarization will be more complicated. The attenuation coefficient for pure air has a theoretical value of $\beta = 0.0126/\text{km}$. However, when theoretical predictions were compared with values measured above 10,000 feet, it was found that β had to be increased to $\beta = 0.017/\text{km}$ to get good agreement. Below 10,000 feet scattering by dust, larger haze particles, etc., was so large as to make the assumption of a Rayleigh atmosphere unwarranted. The fact that β had to be increased from the pure air value indicates that there are a significant number of haze particles at higher altitudes. However, a comparison between measured values and values calculated with $\beta = 0.017/\text{km}$ (presented in the reference), shows that the correction is sufficient to enable the theory to give useful results.

In the region below 10,000 feet the most significant contribution to scattering is due to the particles of the atmospheric aerosol. The scattering of incident light by the particles of the aerosol depends upon their size, number, index of refraction, and the wavelength of the light. The most important class of particles is liquid droplets. As far as is known, the only possible mechanism for the creation of liquid droplets from water vapor depends upon the presence of condensation nuclei. The decrease in visibility when the relative humidity exceeds about 70 percent indicates that these nuclei are hygroscopic. Measurements by Junge⁽⁸⁾ indicate that the distribution of nuclei sizes follows this law.

$$N = K/R^3$$

where N = number of particles per unit volume

K = constant

R = particle radius.

This law appears to be valid in the region $R = 0.05\mu$ to $R = 10\mu$. The maximum particle concentration lies between 0.01μ and 0.05μ ; for smaller R the distribution decreases rapidly with decreasing radius. On the average, the law applies over the earth's surface. The condensation nuclei grow by condensing water on the surface. As the droplet grows the solution concentration decreases and the index of refraction changes. Since there is a wide range of possible particle sizes, particle scattering can vary widely.

The original solution of the problem of scattering by spherical particles is due to Mie. Considering scattering alone, the expression for the transmission of light follows an exponential law:

$$T = e^{-AX}$$

where

T = transmission

A = scattering coefficient

X = path length

Using the techniques of classical electromagnetic theory, Mie showed that the scattering coefficient could be expressed as:

$$A = \pi r^2 NK$$

where

r = particle radius

n = number of particles/cm³

K = the scattering area ratio

The number K relates the effective scattering ratio to the geometrical cross sectional area. It is a function of the index of refraction of the particle and the ratio of particle radius to wavelength. Figure 22 is a detailed graph of the variation of K with the parameter $\alpha = 2\pi r/\lambda$ for a pure water droplet ($m = 1.33$). Figure 23 presents K for several values of the index of refraction. ($m = 1.55$ corresponds to dry salt, which is believed to be the most important condensation nucleus.) The curves for any value of m tend to $K = 2$ with large α . For low values of α , corresponding to small particles, the curves follow a λ^{-4} law; i. e., the Mie theory reduces to the Rayleigh scattering law for small particles.

References 9 and 10 discuss the problem of scattering by a natural haze. Wavelengths investigated ranged from the visible (0.61μ) to the infrared (11.48μ). Measurements showed that the nuclei which caused attenuation of visible radiation also caused attenuation at infrared wave lengths. According to Gebbie most of the haze droplets have radii in the range 0.1μ to 0.6μ ; he assumes the distribution function of the radii is of the form $\exp - k(1 - r/r_0)^2$ where r_0 is the most probable radius (about 0.4μ). Thus the size parameter, α , of most particles in a natural haze for visible and longer wavelengths is less than 6. Qualitatively the attenuation by scattering of haze can be explained by the Mie theory. The scattering coefficient, a function of K , has a peak value near 0.61μ and decreases as shown in Figure 22 with increasing wavelength; thus, in a haze, infrared radiation should be less affected than visible radiation and long wavelengths should be scattered according to Rayleigh's law - which corresponds to observations. Exact calculations are impossible because of the lack of extensive data on the size, distribution, and characteristics of the scattering particles.

The straight line in Figure 23 represents an attempt by Gibbons⁽¹⁰⁾ to obtain a simple approximate expression for the scattering coefficient of natural haze. (The curve must lie between the curves for dry salt and pure water as those curves represent the limiting values for natural droplets.) Over the range of α which is appropriate for the size of particles involved, the approximation for K is $K = 0.9 \alpha = 0.6$. In general, the scattering coefficient σ_i for the i th type particle, of which there are n_i per unit volume, is

$$\begin{aligned}\sigma_i &= \pi r_i^2 N_i K_i \\ K_i &\sim \alpha_i - 0.67 \\ \therefore \sigma_i &\sim (2\pi r_i / \lambda - 0.67 / \lambda_0)\end{aligned}$$

Considering the entire haze:

$$\sigma = \sum_{i=1}^n \sigma_i \sim \sum_{i=1}^n (2\pi r_i / \lambda) - n (0.67 / \lambda_0)$$

From this relation it appears that a relation of the type $\sigma = c \lambda^n$ where $-1 < n < 0$ would be appropriate for wavelengths less than 4μ , Gibbons determined that the value $N = -0.7$ gave a good fit to Gebbie's data over the entire range of measurements - even though n should be positive for larger wavelengths. Therefore scattering by natural haze can be assumed to follow the law:

$T = e^{-\sigma k / \lambda^{0.7}}$ for λ from visible to 10μ , and follow the Rayleigh scattering law for longer wavelengths.

Mie Theory can also give a qualitative explanation for the attenuation by fog. The distribution of particle sizes in a fog has a form similar to that of haze particles, except that there are many more large drops-radii in the order of 2 to 7μ . This means that there are many more particles with size parameter, α , relatively large. Examining the curves for K , one sees that the scattering coefficient will be appreciable for wavelengths up to 40 or 50μ . Droplets in clouds and in rain are still larger so that infrared energy will suffer almost neutral extinction; i. e., for infrared wavelengths K will be approximately constant ($= 2$), so that scattering will be complete for short paths. Figure 24 presents the scattering distribution for a relatively large spherical particle. The predominance of scattering in the forward direction is called the Mie effect. It has been found that this effect increases with increasing α .

CLOUDS

Clouds play an important role in the determination of the background. For this reason they are considered separately, even though they are only special cases of the processes already considered. Low and middle altitude clouds are made up of water droplets; high clouds consist of ice crystals. Because of the R^{-3} relation discovered by Junge⁽⁸⁾ the most important nuclei which act as condensation centers are those with radii 0.1μ to 1.0μ . These nuclei arise from two main sources. Over the ocean salt

particles produced by the wave motion of the sea, and particles produced by combustion processes, dust storms, and volcanic action on land. Those nuclei produced on land are initially small, but grow by coagulation to the observed size. In the troposphere, there are always enough nuclei present so that condensation will occur near the point of water saturation. The growth rate of a droplet dR/dt is inversely proportional to the size of the droplet. Thus, even though there may be a considerable variance in the initial size of the nuclei in an air mass which rises in an updraft, the cumulus cloud which forms will contain a narrower spectrum of droplet sizes. However, as the cloud continues to grow, there will be a broadening of the spectrum due to coalescence. Reference 8 presents several theories which attempt the mechanism of coalescence, but the process is not well defined. Stratus clouds, formed when a layer of air is cooled without vertical movement, display the same type of spectrum broadening with time. Figure 25 presents droplet spectra for various types of low and middle altitude clouds. After a stratus cloud has grown to a few hundred meters in thickness it will start to drizzle. Because of their continual development, it is impossible to consider these clouds to be any given state; rather, each is part of a process. For this reason it is impossible to obtain an exact representation in the model of these clouds. They will be considered only in the gross sense initially described; their mechanisms of scattering and absorbing are special cases of the theories discussed above.

In contrast, the high level clouds - those which appear above 20,000 feet, can be considered to be in a relatively stationary state. These clouds are classed as cirrus - which includes the cirrostratus and cirrocumulus, nacreous, and noctilucent. Only a very limited amount of information, gathered by aircraft penetrations, is available about them. The accompanying table summarizes the characteristics of cirrus clouds.

	<u>Cirrostratus</u>	<u>Cirrocumulus</u>
Particle	Ice Crystal, possibly a few water drops.	Ice crystal, probably some water drops.
Shape	Single well formed column or twin crystal.	Bundles of incompletely formed columns.
Size	100 μ long, 40 μ wide	200-300 μ long, 50-100 μ wide
Particle Concentration	$10^5 - 10^6 / m^3$	$10^6 - 10^7 / m^3$
Water Content	0.01 g/m ³	0.1 - 0.4 g/m ³
IR Transmission		
Per meter	0.992 - 0.9992	0.53 - 0.98
Per 100 meters	0.46 - 0.92	0 - 0.09
Per 1000 meters	0.0005 - 0.46	0

Cirrostratus is the more prevalent type of cirrus cloud, appearing over wide areas preceding storms. Cirrocumulus may appear with cirrostratus and sometimes with thunderstorms. The altitude and thickness of these clouds is a function of season and latitude. For the purposes of the model average values will be taken. The average altitude is 32,000 feet; the average thickness is 2700 feet; they occur about 15 percent of the time.

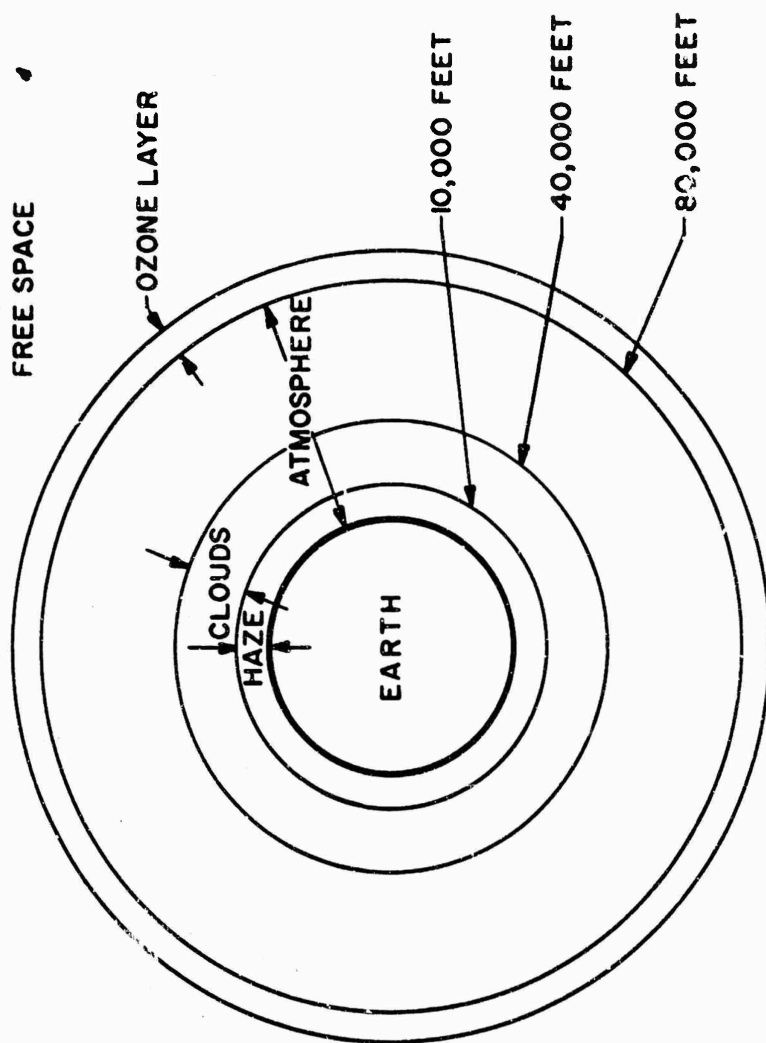
Nacreous clouds appear in the arctic region at altitudes of 21 to 30 km. Their frequency of occurrence is quite low, and their infrared transmission probably quite high. Noctilucent clouds appear only rarely. The most recent data indicates that they appear at an average height of 83 km over high latitudes: 45° - 71° N. Their transmission is probably high. In the model these two types of clouds will be neglected; cirrus clouds will be assumed to be the only high clouds of significance.

OBSERVED BACKGROUND RADIATION

The following table summarizes the sources which contribute radiation to both daytime and night time backgrounds:

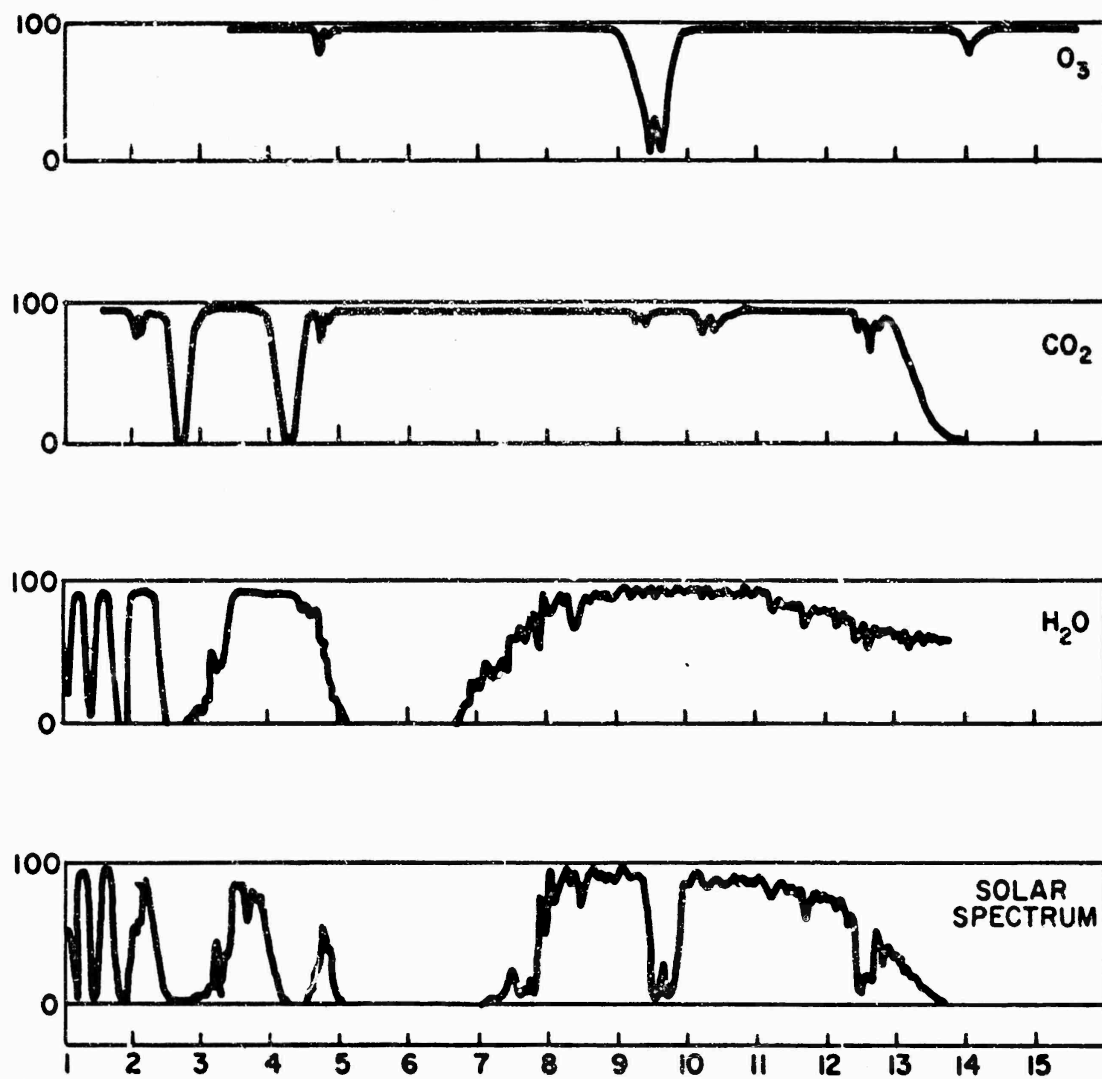
<u>Radiation Sources</u>	
<u>Daytime Background</u>	<u>Night Time Background</u>
1. Scattered radiation (both primary and multiple) from the sun.	1. Radiation from celestial bodies other than the sun. Assumed negligible for simplicity.
2. Solar radiation reflected directly to an observer by the earth or clouds.	2. Emission by clouds and the atmosphere.
3. Atmospheric emission and earth emission (for simplicity the earth is assumed uniform).	3. Emission from the earth which is assumed to be a uniform source; i. e., scattered intense sources are assumed to average out over the surface.

SUN



AW46-280

Figure 20. Atmospheric Model



AW 46-251

Figure 21. Typical Absorption Spectra of Major Atmospheric Components.

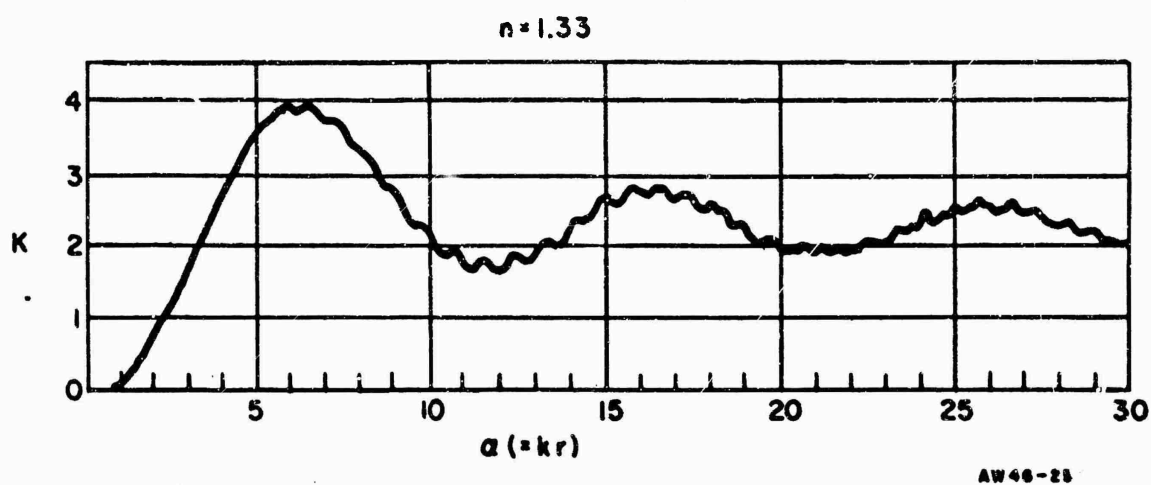


Figure 22. Effective Scattering Ratio to Geometrical Cross-Sectional Area.

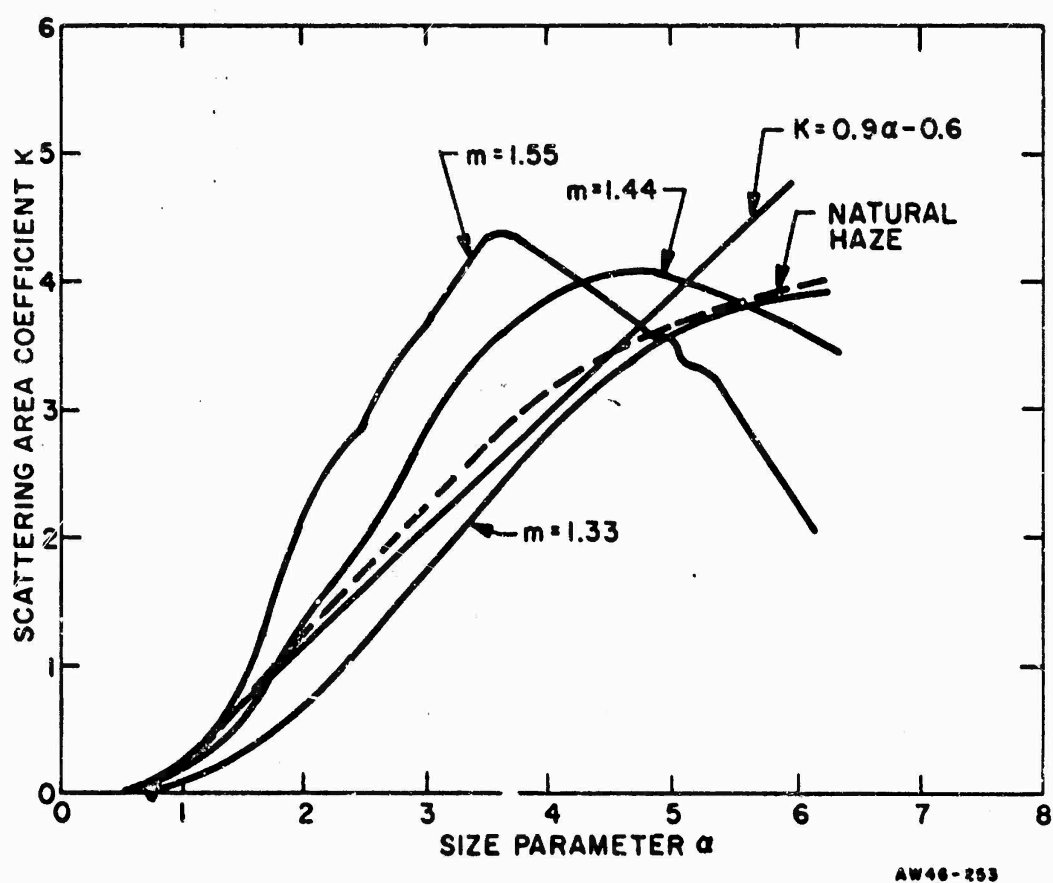
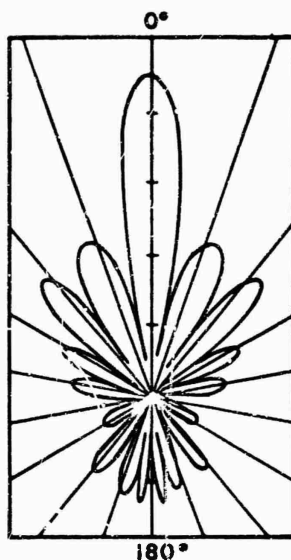


Figure 23. Scattering Area Coefficient for Several Refraction Indices.

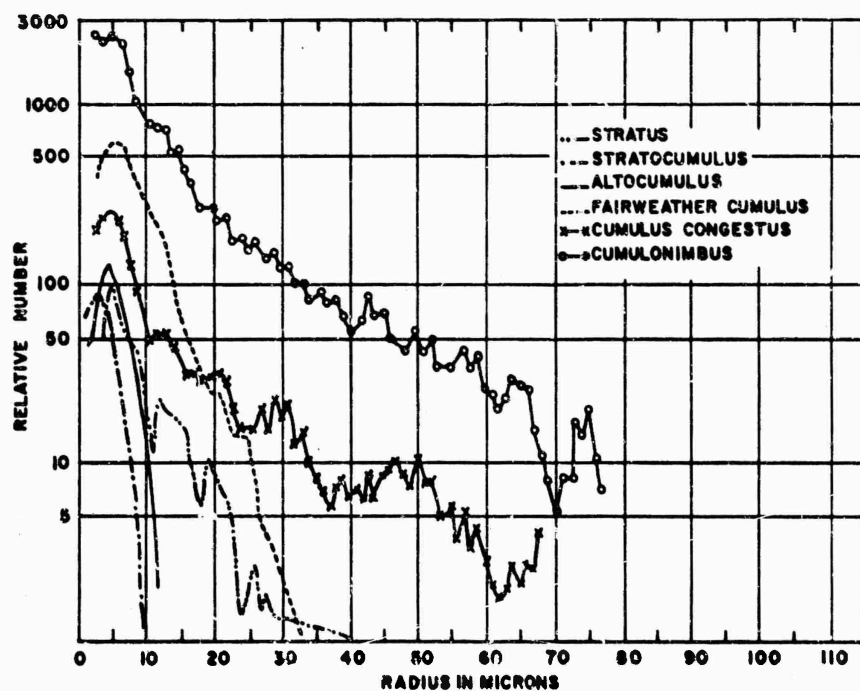


CALCULATED ANGULAR DISTRIBUTION
DIAGRAM FOR SPHERES
 $m=1.33, k=0, a=25$

K =EXTINCTION COEFFICIENT
 m =INDEX OF REFRACTION
 $a=\pi r D/\lambda$

AW46-254

Figure 24. Scattering Distribution for a Large Spherical Particle.



AW46-255

Figure 25. Droplet Spectra for Various Types of Clouds.

EMPIRICAL CONSIDERATIONS FOR A BRIGHTNESS MODEL

Delineated in the previous section is a general broad outline of the several processes which affect the infrared background. To formulate a completely general mathematical model even for the region of the spectrum from 1-10 microns represents a highly ambitious project. To be accurate, such a model would no doubt be complex. If it is to be more than a concept, and thus produce real numbers, severe burdens in labor and time may be imposed in its solution for specific problems. In many cases this is not justified by the requirements and a reasonable approximation is all that may be required. The purpose here is to present an expression of proportionality that may be developed into a reasonable approximation of the sky brightness function. Such an expression, because of its simplicity, must necessarily ignore the many causes of variations in the background and must be judged on the merits of its general or average accuracy. While the data taken at Key West has been used to make the approximations, the formula cannot be made to match at every point. In fact, the formula can only be made to approximate an average for most of the data. It must be remembered that the backgrounds measured at Key West were highly complex in their nature and are not themselves representative of average backgrounds. Measurements for a blue cloudless sky are required to make a beginning in this direction and it is hoped that the proportionality will be tested against such measurements. Investigation could then be made as to the best manner of adjustment for changing conditions.

Upon examination of background measurements, there are some trends that always occur. The energy received by a measuring radiometer is generated by two sources, the earth and the sun. The energy in the field of view is propagated along the line of sight modified by the complex processes of primary and higher order scattering, absorption, reflection, refraction, diffraction and emission. In general, however, spectral measurements (17, 18)

of the background characteristically show two sources of radiation, 1) nearly ambient temperature radiation (earth) and 2) high temperature radiation (sun). Some of the low temperature radiation is due in part to atmospheric constituents absorbing high temperature solar radiation and in turn re-emitting as a low temperature source.

Measurements made in terms of elevation and azimuth of the observed point also show certain general characteristics. It is noticed that the radiance emitted by clear sky is higher near the horizon than anywhere else and decreases with elevation. Again, when one measures the sky towards the sun, the radiation levels increase rapidly closer to the sun. Bennett, Bennett and Nagle⁽¹⁹⁾ show that the measured radiance at the horizon is closely that from a blackbody at approximately ambient temperature.

Depending upon the position of the sun, there would be additionally an increase at shorter wavelengths (1-3 μ) due to increased back-scattering from the denser air mass as one measures closer to the horizon. This occurs when the sun is behind the observer so that the observed point is at a large angle with the sun which is primarily in early morning and late afternoon hours. A further condition exists due to polarization.⁽²¹⁾ A minimum is expected at 90° from the sun but this is usually found to be shifted towards the zenith. Similar trends can be noted in the Polar Plots presented in the first part of this report, even though the sky is overcast or, at best, highly clouded, and the trends can be due to other causes. A plot of elevation with constant azimuth for the overcast sky shows the radiation levels near the horizon to be close to the blackbody levels at ambient temperature, but with increasing levels encountered with elevation angle in some cases due no doubt to change in temperature of the cloud cover, or differences in ambient temperature at higher altitudes. This would be apparent in total radiation measurements that cover a broad spectral range as these do, 0-16 μ . For the 4.25 micron region, if the data shown in Figure 4 is smoothed to remove some of the detail, it would appear as in Figure 26. No minimum is observed due to polarization but the trend of decrease with elevation from the horizon and increase toward the sun can be noted.

In Figure 5, which is for blue sky of June 23rd, a minimum is noted approximately 60° from the sun and the usual decrease from horizon and increase toward sun as well. It will be repeated here that these affects probably would not be so apparent except for the fact that the filter used to make the measurements has a bandwidth from 3.75 to 4.75 microns and consequently admits radiation outside of the CO_2 absorption region. These effects noted are probably due more to this radiation than to CO_2 emission.

To attempt a computation which would construct these polar diagrams synthetically, two general shaping functions have been chosen, one to represent the family of curves originating from the sun position and the other to represent the family of curves originating at the horizon. The sum of these two functions would then represent a proportionality which, when used with suitable constants, might approach the actual radiation measurements of the sky. Simplicity must also be the keynote for such functions or their usefulness is completely nulled. Since they are approximations only, a great deal of time for computing should not be required.

For several pieces of data at Key West, the family of circles originating with the horizon can be approximated by

$$\left(\frac{2 + \sin \Theta}{2} \right)^{-0.5} \quad (1)$$

Where Θ is the elevation angle, at any azimuth, measured from the horizon.

For the same pieces of data, the family of circles originating with the sun can be approximated by

$$1 - \sin^{1/2} \phi \quad (2)$$

Where ϕ is the angle between the sun and the observed point measured from the observer's station. Figure 27 is an illustration in point for the 0-16 micron region for two days. These functions

were used to compute the same points measured and published in table form in Report No. 3 for this contract. ⁽⁴⁾ The original data, the computation results, and the percentage differences are presented in Tables III, IV, and V, and polar plots have been made from the computations to compare with the data plots. Figures 28, 29, and 30 are the computed diagrams to be compared with Figures 2, 3, and 5, respectively.

The equation was written as follows:

$$N_{b_{\lambda_1-\lambda_2}} = \left(N_{a_{\lambda_1-\lambda_2}} + .12N_{s_{\lambda_1-\lambda_2}} \right) \left(\frac{2 + \sin \theta}{2} \right)^{-0.5} + N_{s_{\lambda_1-\lambda_2}} \left(1 - \sin^{1/2} \phi \right) \quad (3)$$

where N_b is the radiance of the background, N_a is the radiance due to ambient temperature and N_s is the radiance due to the sun.

Since it is not possible at this time to present a finished formula from the Key West data, but only to establish a proportionality, numbers were chosen for N_a and N_s to fit the data. N_a was taken as the blackbody radiance for ambient temperature for the wavelength region under consideration and this works out very well. In a sky completely overcast with clouds, it would be almost impossible, without either measurement or extended analysis, to choose a value for N_s . The 0-16 micron region contains almost all of the radiation for blackbody of 5500°C which is the equivalent for the sun. A great deal of this radiation would be lost due to backscattering and reflection from the top of the cloud cover. In turn, a large amount would be absorbed and re-radiated with ambient temperature distribution. There would be still further attenuation due to high relative humidity at ground level. It was evident that visible illumination was extremely low on June 16 and 17. N_s was taken as $4.45 \times 10^4 \mu\text{w}/\text{cm}^2 \cdot \text{steradian}$ for the 0-16 micron region and $178 \mu\text{w}/\text{cm}^2 \cdot \text{steradian} \cdot \text{micron}$ for the 4.25 micron region.

To N_a was added 12 percent of N_s as a coefficient for $f(\theta)$ because higher order scattering causes bright sky along the horizon resulting in uniform intensity with respect to azimuth, ⁽²¹⁾ and for the present is assumed to be a function of elevation from the horizon. These values were chosen to suit the 0-16 micron data for June 16th. Table III gives the observed values made during the field trip, and below these values, computed with equation (3). The percentage error has been obtained simply by taking the difference between observed and computed values and dividing by the observed value. Whether the error is plus or minus indicates the computation was high or low. For the 25 observed points, there are 14 minus values and 11 plus values with a median around -2 percent. The highest deviation was plus 22 percent and the lowest was minus 35 percent. Figure 28 is a polar plot of the computation and is to be compared with the plot of the actual data, Figure 2.

The same values for N_a and N_s were used to repeat this procedure for the 0-16 micron region for the following day. The results are shown in Table IV and the computation is plotted in Figure 29 to be compared with the actual data plot of Figure 3. Here the computation is a little on the high side with a median of plus 14 percent. A very small downward revision of N_s would have corrected this since June 17th was darker than June 16th.

Table V and Figure 30 are the results for the 4.25 region giving a median error of plus 1-1/2 percent with more than 1/2 the values being on the plus side. These are to be compared with the actual data plot of Figure 5. A computation was made but not plotted for the 4.25 region for June 17th with the results in Table VI. These can be compared to the actual data plot of Figure 4. As in Table IV for 0-16 microns, the values are all on the plus side with a mean of approximately plus 38 percent.

It appears that a proportionality exists which may be simple to compute and accurate enough for many engineering problems. In a cloudless and clear sky, the radiance levels near the sun have

a much steeper gradient than in a hazy sky where the increased scattering would tend to broaden the gradient. For the same reasons, the apparent emissivity of the atmosphere would tend to flatten as the air became filled with more scattering particles.

If $f(\Theta)$ is written

$$\left(\frac{2 + \sin \Theta}{2} \right)^{1 - \beta} \quad (4)$$

and plotted, as in Figure 31, for different values of β , the form is similar to that given by the expression for the emissivity of the sky⁽¹⁹⁾ when $\beta > 1$. As β increases, the resultant curve approximates emission curves for the sky as the sky becomes more blue with less scattering in the near infrared as a result.

In the same way, $f(\phi)$ can be written

$$1 - \sin^{1/\alpha^2} \phi \quad (5)$$

with the result that, as α increases, the steepness of the gradient increases about $\phi = 0^\circ$, as shown in Figure 32. β and α , therefore can be taken as "indicators" of the condition of the sky, becoming larger as the sky becomes clearer with less scatter. When there are clouds present in the sky, polar diagrams would, in certain wavelength regions more than others, produce higher values than the blue sky, and produce data that was very erratic in form because it would represent a large amount of detail. Under the overcast conditions at Key West, plots of energy levels with respect to Θ but at constant azimuth show a convex appearance that is no doubt due to heating of the cloud cover or a gradient in air temperature with altitude. If this is a general condition for certain types of sky, then fractional values of β will approximate the condition as seen in Figure 31. The detail of the cloud structure would disappear, but an average value would result.

No doubt if α and β were to be evaluated, it would be seen that they are really complex functions. Certainly they are a function of wavelength, and measurements on blue sky would determine values for specific wavelength regions. All of the computations given here were for $\beta = 1.5$ and $\alpha = 1.4$, or approximately equal. It may be that one index of the sky is all that is necessary to give a good approximation. Measurements of α and β would also produce the proper values for N_s which would be more compatible with expected values, especially in a clear sky.

The computations were not very difficult. The only one which appears troublesome is the determination of ϕ . This is a function of the elevation and azimuth of the sun, and the elevation and azimuth of the observed point, and is expressed as follows:

$$\cos \phi = \sin w \sin \Theta + \cos w \cos \Theta \cos p \quad (6)$$

where

p = the difference in azimuth of sun and observed point

w = sun elevation

Θ = observed point elevation

Most values of ϕ used in the computations were read by using dividers on a ball having latitude and longitude lines every 10 degrees. The dividers measure the chord distance between two points and this is used on any longitude (great circle) line to read degrees. ϕ has been read to one degree accuracy in this fashion on a 9-inch diameter ball which is accurate enough for ϕ greater than 30° . When ϕ is smaller, or changes slowly, as in the case for target azimuth planes at small angles to the sun azimuth plane, ϕ must be computed with equation (6). The values for the sines of Θ and ϕ in equation (3) were to 3 decimals and the calculations were performed on a slide rule.

Table III

16 June 1959 0-16 Microns

Azimuth → Elevation ↓	270	330	30	90	150	210
5	1.46	1.44	1.44	1.52	1.57	No
20	2.15	1.73	1.69	1.82	1.71	Data
40	1.79	1.71	2.53	2.23	1.87	Points
60	1.84	1.90	2.25	2.63	2.50	
80	3.18	3.18	4.06	3.70	5.16	
	Computed Values					
5	1.49	1.47	1.51	1.58	1.50	1.47
20	1.40	1.47	1.61	1.74	1.58	1.43
40	1.57	1.68	2.05	2.26	1.94	1.66
60	2.06	2.36	2.75	3.21	2.70	2.21
80	2.96	3.23	3.73	4.85	3.65	3.08

Percentage Error - Computed From Observed

5	+ 2.0	+ 2.1	+ 4.8	+ 3.8	- 4.5
20	-35	-15.0	- 4.7	- 4.4	- 7.6
40	-12.3	- 1.75	-19.0	+ 2.7	+ 3.7
60	+12.0	+19.5	+22.0	+22.0	+ 8
80	- 7.0	- 6.1	- 8.1	-34.0	-29

14 minus values

11 plus values

median approximately - 2 percent

Table IV
17 June 1959 0-16 Microns

Azimuth Elevation → ↓	Observed Values				
	270	330	30	90	210
5	1.41	1.36	1.50	1.79	1.40
15		1.56	1.61	2.14	1.45
30	1.53	1.65	1.86	2.50	1.87
45	1.44	1.62	1.83	3.05	1.26
60	1.39	1.59	2.11	6.79	1.36
75	1.49	1.59	2.04	2.31	1.58
90	1.76				

Computed Values				
5	1.82	1.51	1.76	2.04
15	1.59	1.41	1.79	2.3
30	1.45	1.38	2.03	2.9
45	1.33	1.49	2.34	3.7
60	1.5	1.77	2.60	4.53
75	1.82	2.05	2.49	3.01
90	2.39			

Percentage Error Computed From Observed				
5	+29.0	+11.0	+17.3	+14.0
15		- 9.6	+11.2	+ 7.5
30	- 5.2	-16.7	+ 9.15	+16.0
45	- 7.6	- 8.0	+28.0	+21.0
60	+ 7.9	+11.3	+23.0	-33.0
75	+22	+29.0	+22.0	+30.0
90	+36			
9 minus		27 plus	median approximately +14%	

Table V

23 June 1959 4.25 Microns

Azimuth → Elevation ↓	270	330	30	90	150	210
			Observed Values			
5	155.4	155.4	153.8	153.9	154	152.4
15	148.7	148.2	148.7	148.7	148.8	148.8
30	141.6	141.6	141.6	144.7	143.2	141.1
45	139.6	140.5	141.6	190.7	148.9	145.4
60	143.6	144.5	143.5	-	183.5	162.7
75	176.	169.8	185	-	191	180.6
90	193.4					

Computed Values

5	152.3	150.2	153.6	157.1	152.3	150.2
15	144.1	144.4	152.5	159	151	144.3
30	139	143.1	158.2	169.4	154.8	141.8
45	141.3	148.4	169.7	189.5	166.6	146.6
60	155.1	163.6	189.5	218.4	186	163.1
75	175.3	187.5	215.3	301	208.2	185.5
90	207.8					

Percentage Error - Computed from Observed

5	-2	-3.3	-0.03	+2.1	-1.1	-1.4
15	-3.1	-2.6	+2.5	+6.9	+1.5	-3
30	-1.8	+1.1	+11.7	+31	+8.1	+0.5
45	+1.2	+5.6	+19.8	+ .06	+11.9	+0.85
60	+8.7	+13.2	+32.4		+1.4	+0.25
75	-0.4	+10.4	+16.4		+3.8	+2.7
90	+7.5					

24 plus values
11 minus values

median approximately +1.5%

Table VI

17 June 1959 4.25 Microns

Azimuth → Elevation ↓	270	330	300	90	150	210
Observed Values						
5	118.6	103.6	103.6	109.6	180.7	123.9
15		87	75.8	92	122.9	128
30	97.1	108	122.9	109.6	113.8	139.1
45	148.4	120	111.1	90.4	116.3	105.6
60	117.3	120.8	130.5	Sun	130.5	130.5
75	126.4	136	121.8	135.9	119	123.8
90	123.8					
Computed Values						
5	159.6	150.9	156.0	161.6	154.3	151.8
15	148.4	143.9	168.4	171.0	152.5	143.9
30	137.0	139.9	161.6	167.0	173.8	139.0
45	133.9	142.6	174.3	213.9	167.8	139.9
60	139.6	151.5	188.2	273.0	180.2	158.3
75	154.8	153.5	190.2	213.9	185.5	162.1
90	179.6					
Percentage Error - Computed From Observed						
5	+29.0	+45.6	+50.6	+47.6	-14.6	+22.5
15		+65.0	+122.0	+86.0	+24.0	+12.5
30	+41.0	+29.5	+30.0	+71.5	+52.7	- .072
45	-19.0	+18.8	+57.0	+137.0	+44.2	+32.5
60	+19.0	+24.0	+44.3		+38.0	+21.3
75	+22.5	+20.2	+56.0	+57.4	+56.0	+31.0
90	+45.0					

32 plus values - 3 minus values - median approximately +38%

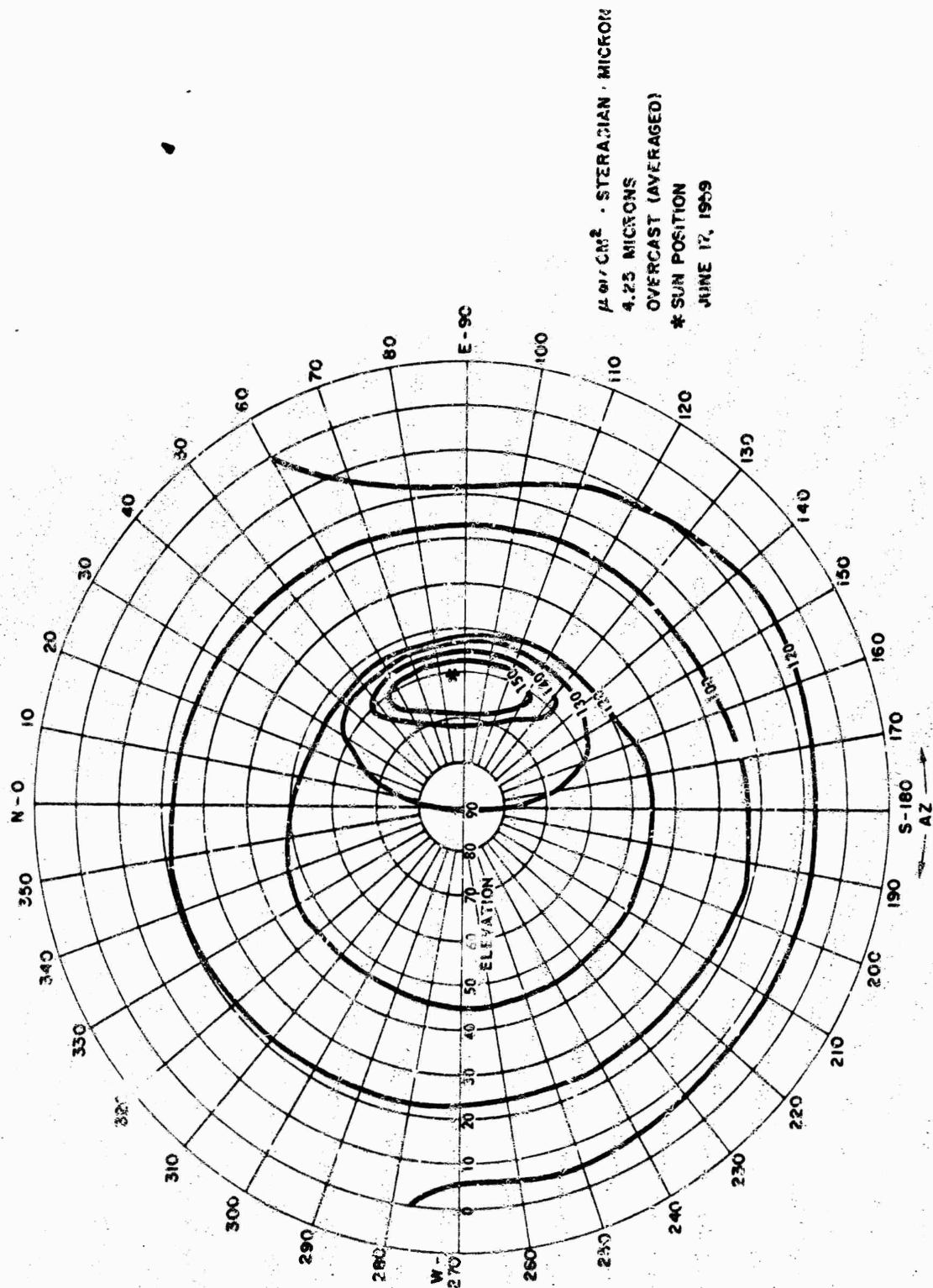
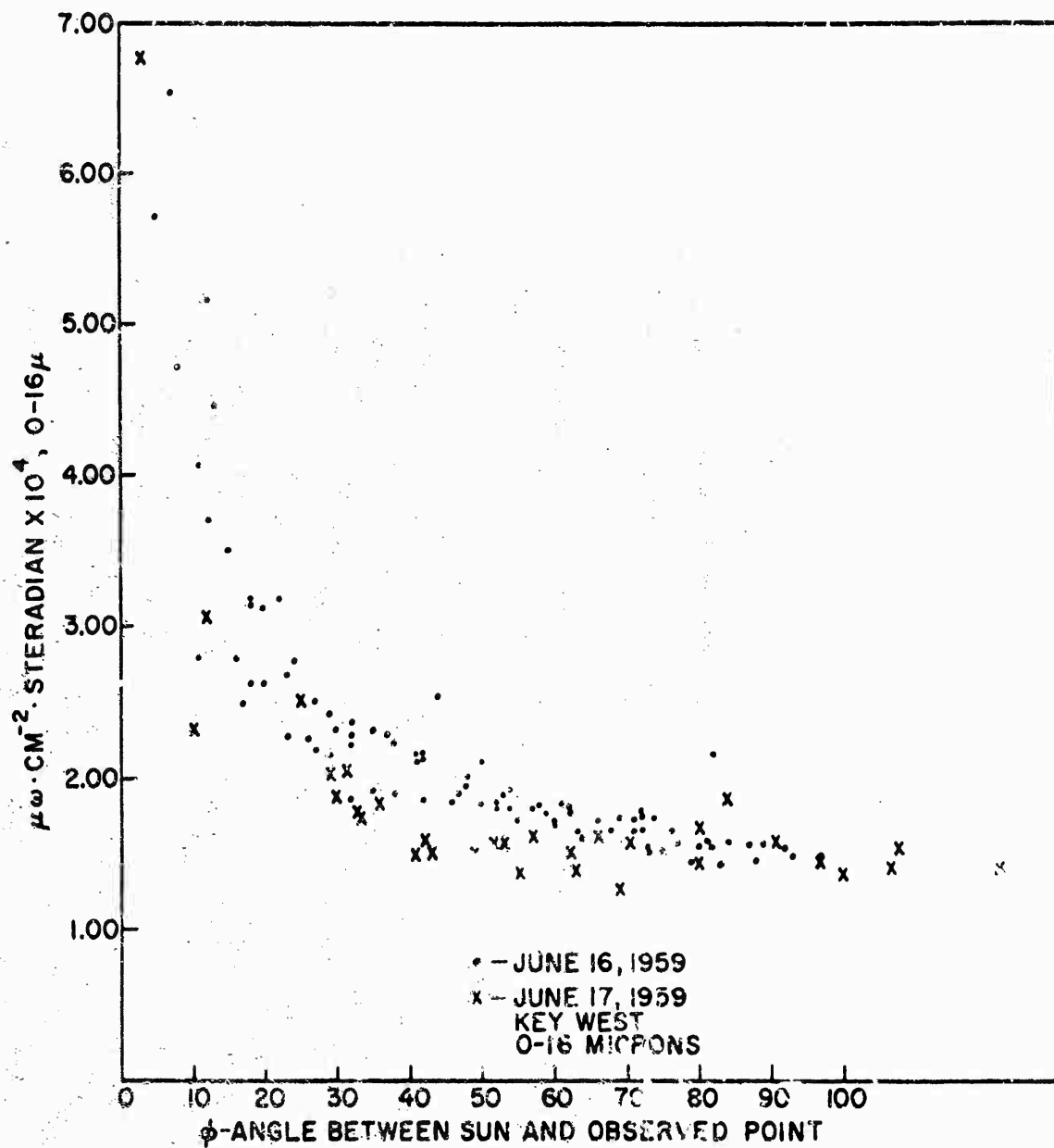


Figure 26. Averaged Overcast Sky, June 17, 1959, 4.25 Microns.



AW46-247

Figure 27. 0-16 Micron Region With Respect to Sun Position.

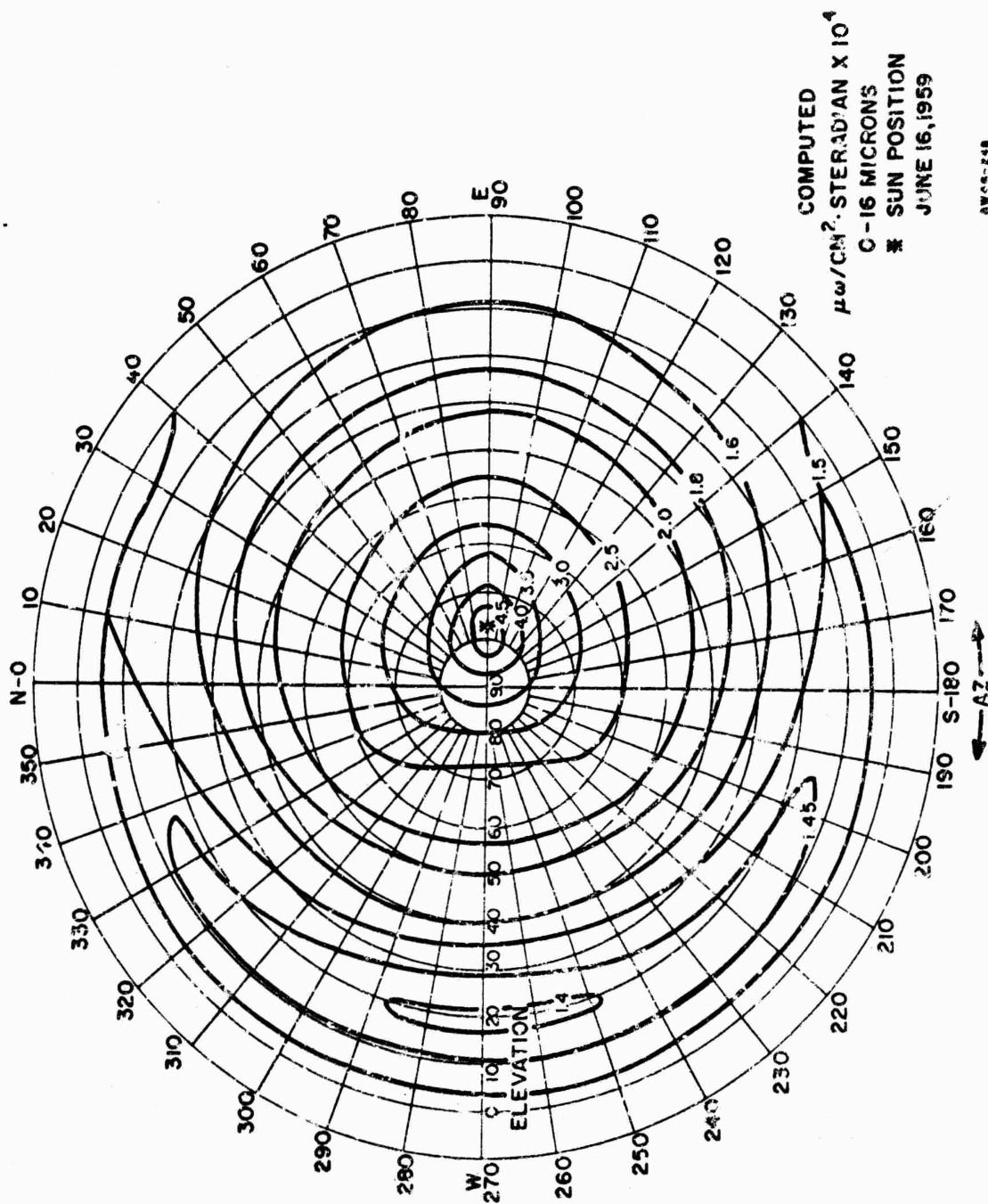


Figure 28. Computed 0-16 Micron Region for June 16th.

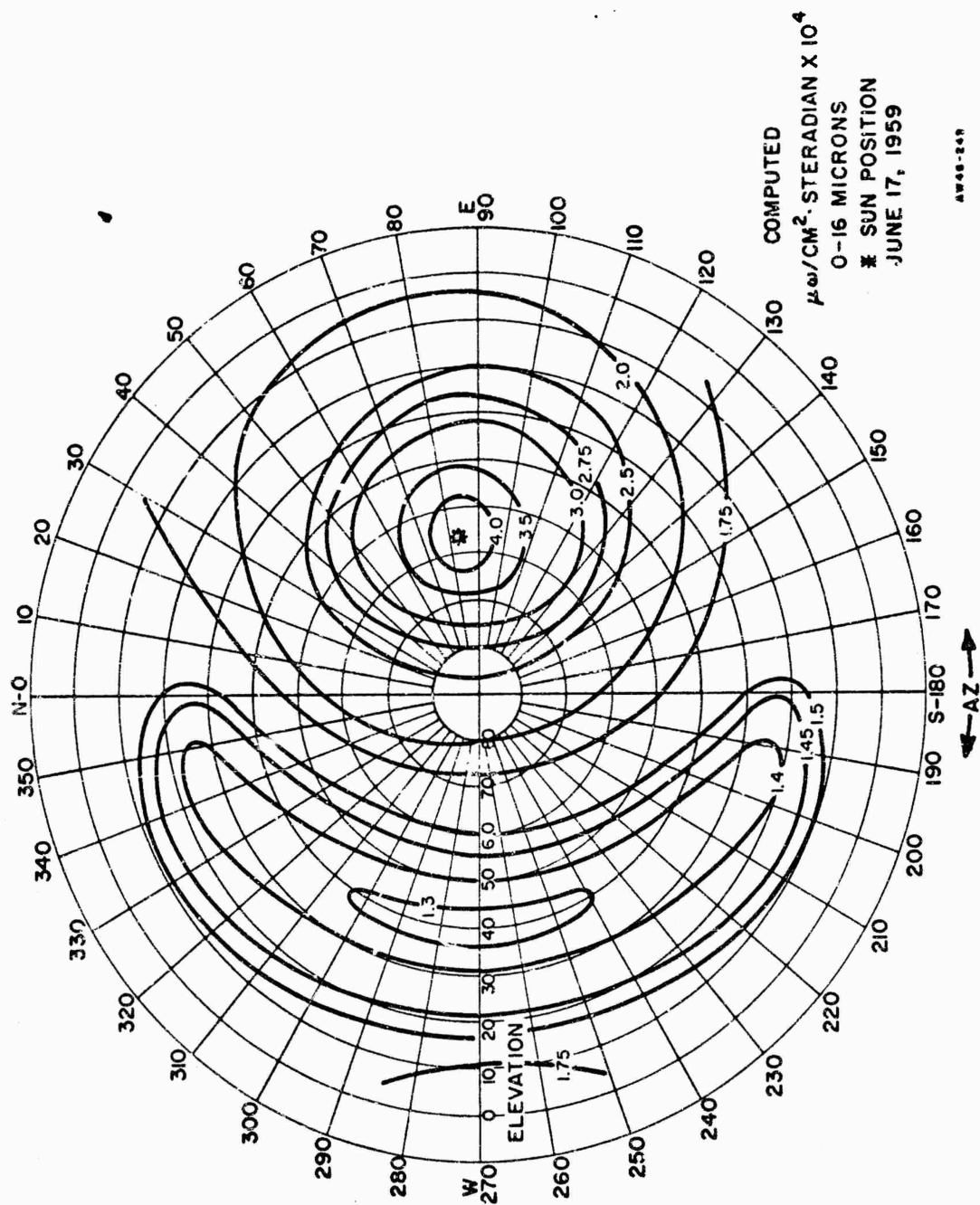


Figure 29. Computed 0-16 Micron Region for June 17th.

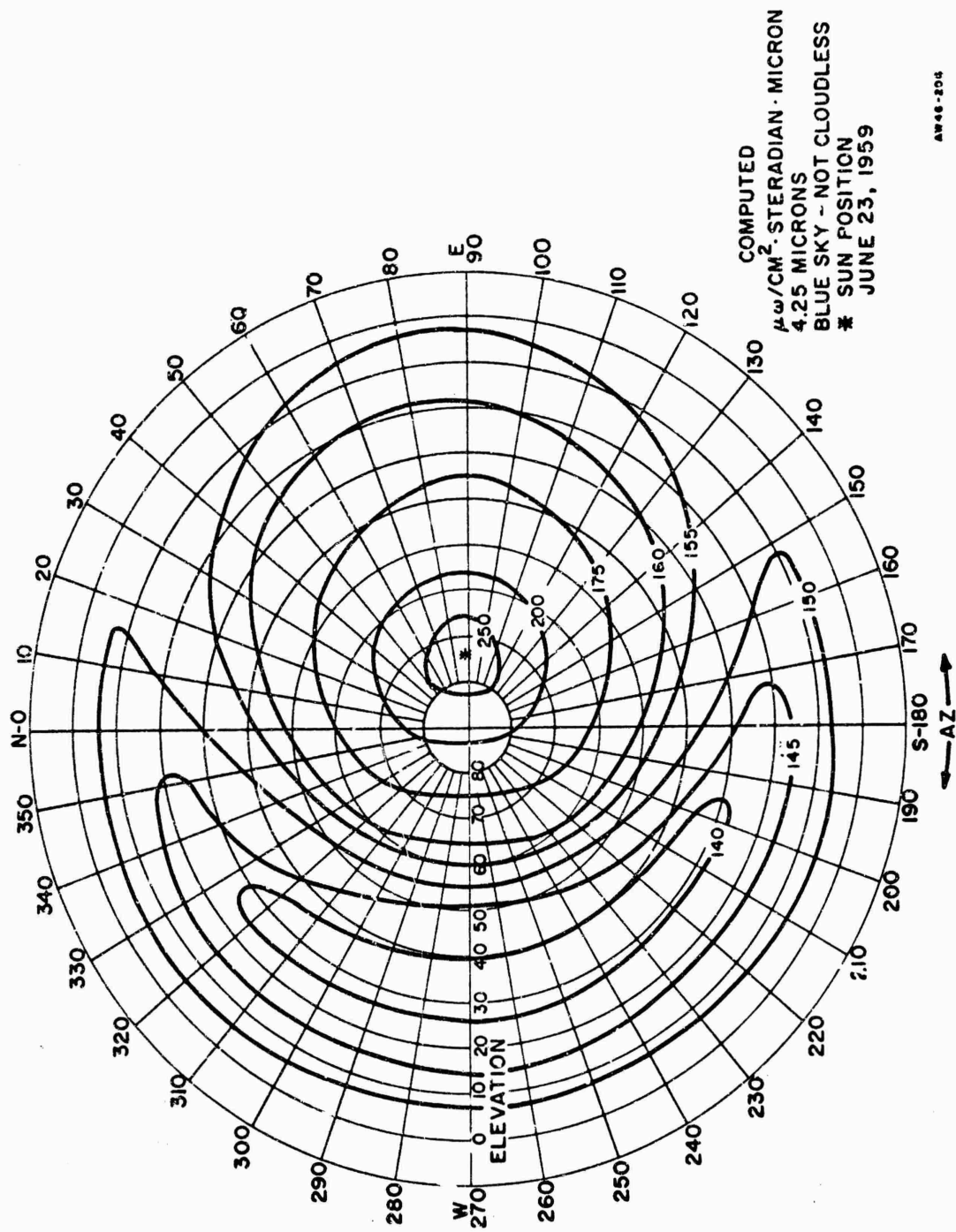


Figure 30. Computed 4.25 Micron Region for June 23rd.

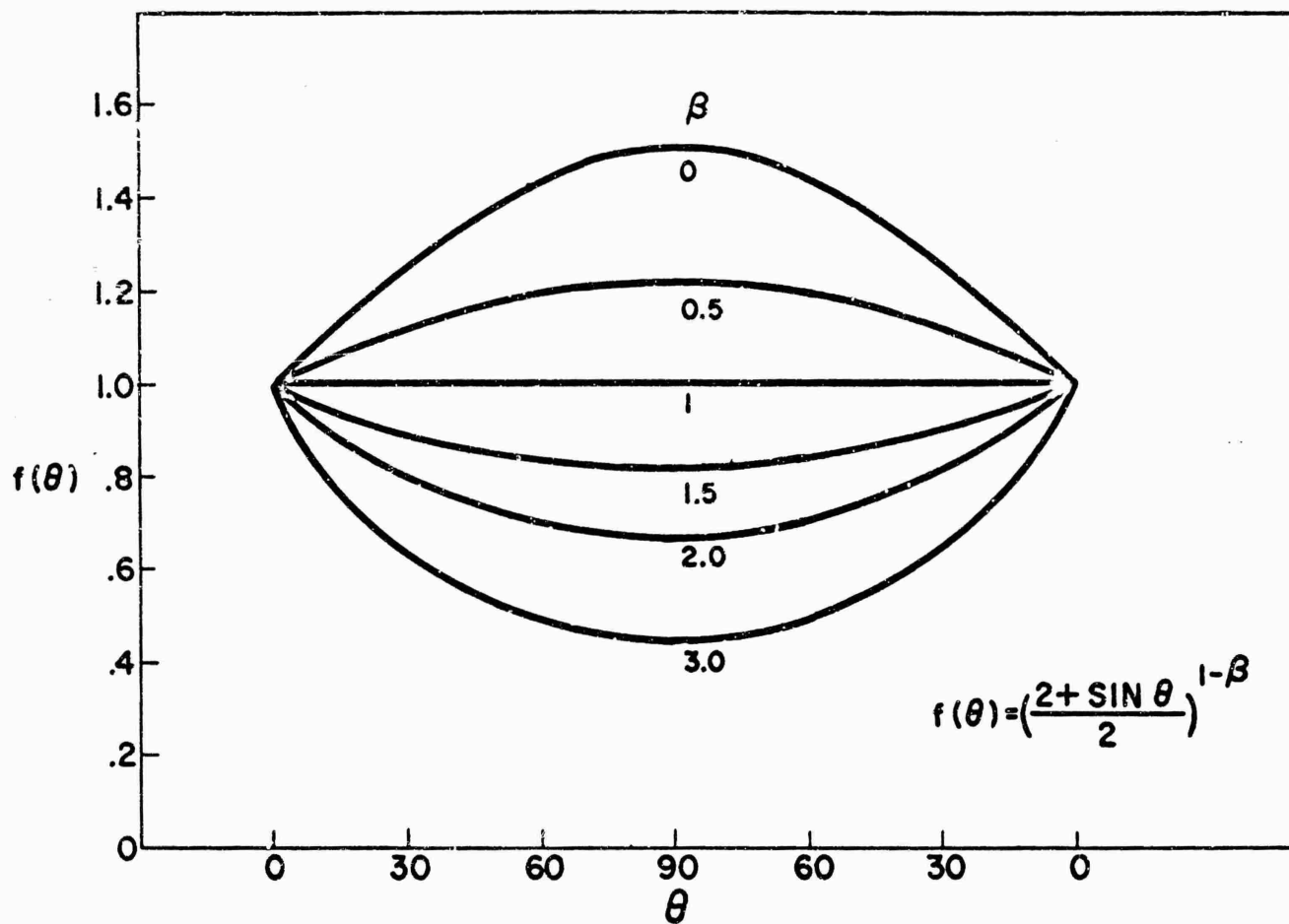


Figure 31. Effect of β on $f(\theta)$

AW46-295

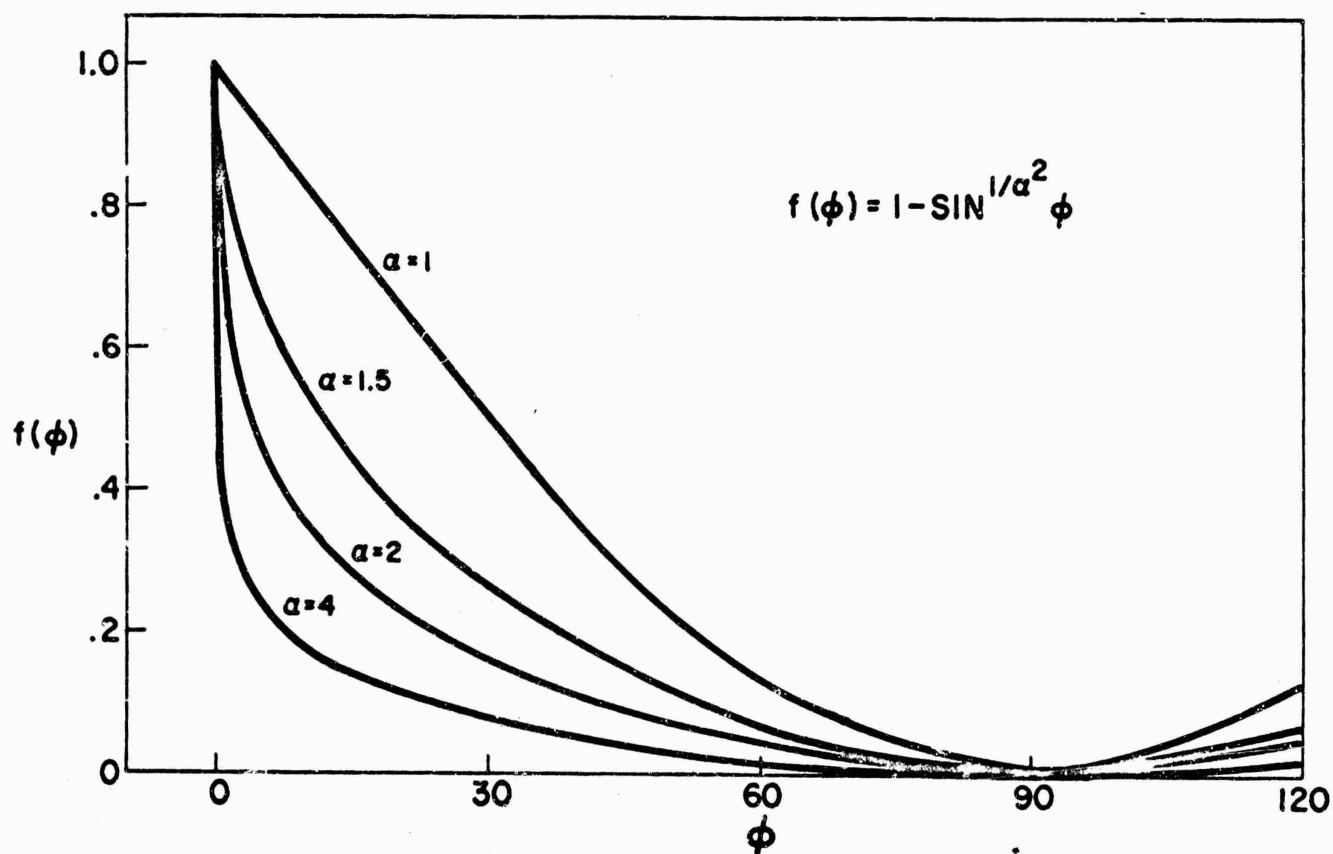


Figure 32. Effect of α on $f(\phi)$

AW46-297

ESTIMATED EARTH AND SKY BACKGROUND NOISE INTERFERENCE IN INFRARED DEVICES

INTRODUCTION

Backgrounds are a complex structure which reflect, scatter, and absorb incident electromagnetic radiant energy and, further, reemit some of this radiant energy due to their own thermal agitation and chemical composition. This gaseous composition of the atmosphere varies further with time, altitude and location on the earth. However, if one disregards the source from which the electromagnetic energy may have arisen and the corresponding operations through which it may have been subjected, some meaningful characteristics of backgrounds may be noted based upon strictly empirical observations. The background is there and possesses certain distinguishable features characterized by the spatial structure and spectral distribution of the radiation. Some of these salient characteristics are briefly noted below in Radiometric Observations.

In order to more fully and conveniently apply empirical gradient data regarding the background, it has proven useful to develop a hypothetical one dimensional model of background interference described below in One Dimensional Background Noise Spectra. This model has proven especially valuable in indicating expected interference distribution in regions of the spectral or spatial distribution where measurements have not as yet been made in great detail--for example, at high space frequencies. This heuristic model is developed below and indicates, for example, the importance of contrast in determining background interference, and further, indicates the expected space frequency accelerated drop off at high frequencies, and the expected levelling off at low space frequencies (it cannot continue to be $1/f^2$ to zero space frequency). This spatial structure of the power density function will also be shown to vary with altitude or distance to interfering backgrounds

(clouds) so that satellites viewing the earth will presumably see a different spatial structure than we are accustomed to, i. e. scaled down but with identical contrasts. This expected variation in structure with angle and altitude is described below and will be corroborated in the near future by a detailed examination and correlation of TIROS satellite pictures of the earth within the limits of the resolving power of that instrument.

The one dimensional Wiener spectrum of background noise has only limited usefulness in the calculation of noise interference levels when used with two dimensional field stops and reticles. Unfortunately, most background gradient structure is obtained in this manner today despite methods proposed by R. Clark Jones several years ago to obtain the two dimensional spectra directly. (24) A method of reducing the one dimensional data to a two dimensional Wiener spectra is described in Two Dimensional Background Noise Spectra.

Finally, one may apply directly the two dimensional noise spectra against the field stop and reticle to obtain an estimate of expected background interference. (25) This method is illustrated briefly in the section on Reticle-Aperture Space Filtering.

RADIOMETRIC OBSERVATIONS

Figure 33 illustrates some typical ambient radiometric measures of background intensity as a function of wavelength. Background interference existing primarily in wavelengths shorter than 3μ occur as a result of diffusely reflected and scattered sunlight. Atmospheric absorption bands due to CO_2 and H_2O are evident. Re-emission of solar energy in the absorption bands occurs at much lower temperatures than the apparent 5900°K sun and does not fill the absorption band corresponding to the decrease in solar intensity.

In the thermal emission band, beyond 4μ , the average spectral distribution follows that of an apparent 300°K blackbody. In this spectral band, atmospheric absorption and re-radiation occur at

closely the same apparent temperature and a corresponding smooth emission curve results. Beyond 8μ , however, little atmospheric emission occurs because the longer wavelength involved is significantly larger than the air molecules themselves (little atmospheric scattering is experienced at these longer wavelengths). Thus, only emission from clouds beyond 8μ permits a 300°K blackbody approximation of background interference when looking up. When looking down at the earth between $8-13\mu$ there would presumably be less contrast.

It will be developed shortly, that absolute background contrasts are the greatest single factor in developing interference levels in various spectral regions. We are familiar with the existence of relative contrasts in the visible spectrum and the enhancement of these contrasts (at least for clouds) by the use of near infrared film near 1μ . Actual contrast measurements between clouds and sky are shown to some extent in Figure 33. These contrasts are moderate towards the blue end of the visible spectrum, and then increase to ratios of 10, or 100, or a 1000 to 1 in the $1 - 3\mu$ band. It is these large contrasts that make daylight background interference in the $1 - 3\mu$ band such a formidable problem. Contrasts in the longer wavelength regions between 3.5μ and 8μ are small - an ideal region for obtaining minimum background interference. From $8 - 13\mu$ large contrasts exist again between cloud and clear sky indicating another region of large background interference.

ONE DIMENSIONAL BACKGROUND NOISE SPECTRA

The variations in intensity or detail of light distribution which arise from the background in space, has been described by R. Clark Jones as space power - or Wiener - spectra with ordinates of normalized space frequency. This method of describing actual backgrounds has been used with success in gradient meter measurements similar to the one conducted by the The Ramo-Wooldridge Corporation under Contract AF 19(604) 3473 from AFCRC and earlier under contract

AF 33(600) 30489.^(3,4) These spectra describe the background as varying approximately inversely to some power of the space frequency - at least at the higher space frequencies that have been measured. But this method of measurement gives only a partial description of the background since all phase information is lost; i. e. , an inverse space frequency spectra itself may arise from different background configurations. Furthermore, as a practical matter, if it is desirable to distinguish or highlight a particular size or shape object against the background, it may require different optimum filtering techniques - such as a discrete or non-linear space filter. (26)

The use of unrestricted theoretical models, however, may suggest alternate study, measurement or testing methods. For example, the model presented describes the nature of the transition from the ambient intensity level to the lowest space frequency spectra which can practically be measured. The model also permits an estimate of higher probability distribution of the background and permits alternate improved filtering techniques. Finally, the use of a theoretical model may permit a systematic method of normalizing or standardizing background space filtering techniques and their methods of test.

It will be assumed in the discussion which follows that, by and large, the greatest single source of background noise occurs from cloud structure - either against the sky when looking up - or against the earth when looking down. A Poisson distribution of cloud sizes will be assumed with a 50 percent probability of cloud occurrence at any point around the world. This assumption compares with an actual average 52 percent cloud cover around the world, according to C. E. P. Brooks. (5)

A series of pulses of random spacing and random width are used, all with a constant amplitude or height. These pulses then represent clouds against a blue sky (or earth) when scanned with an infinitesimally small field of view in one dimension. Only two amplitude levels are assumed to exist. The high level represents reflected sunlight (or ambient temperature of the cloud) and the

lower level represents scattered sunlight or earth (or apparent ambient temperature of the blue sky). The distribution of pulse lengths or cloud widths $P(d)$ is assumed to be a Poisson distribution peaking at lengths of 4 nautical miles, shown in Figure 34 and decreasing in probability in either direction of length or width from this value. The use of a particular probability of pulse duration, allows us to derive spectra for satellites since the cloud angular subtense will be proportionally reduced with altitude. A more exact distribution of cloud lengths will be determined in the near future; hopefully at Ramo-Wooldridge, with a detailed examination and compilation of TIROS pictures.

Most modern probability and statistic textbooks describe the mathematical relations and functions necessary to define the spectrum of a random or stochastic process. The results of these derivations only are presented in this section for the example chosen to represent the background.

The model selected to describe the background is illustrated below. The length of pulse or spacing is distributed in space x according to a probability function $P(a)$, with a height of magnitude either $+1$ or -1 . In practice, the difference between the two levels represents contrast. The resulting spectra may be multiplied by the contrast intensity in any spectral region as a first approximation to the gradient background interference.

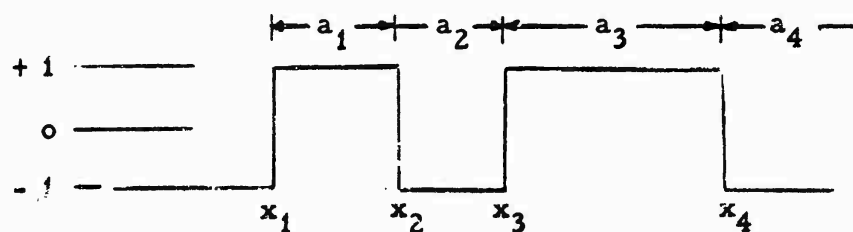


Figure 35

The model at this time neglects the ambient or dc level of the intensity which is always some value greater than zero. However, the average level may be readily added - and this will be done later - by employing the superposition concept to take care of the ambient level. The resulting ambient term will always appear as a δ function at the origin with an integral equal to the ambient level.

If the functions $\phi(f)$ and $\psi(f)$ are defined as follows:

$$\phi(f)_x + j\psi(f)_x = \int_0^{\infty} P(a) e^{-j 2\pi f_x a} d(a) \quad (1)$$

then the normalized power spectral distribution is given by H. M. Foley in "An Investigation in the General Theory of Pressure Broadening and an Experimental Study of Pressure Effects in the 14 μ Band of Hydrogen Cyanide." PhD Thesis, University of Michigan, 1942.

$$S(f) = \frac{2}{\pi \bar{a}(f_x)^2} \frac{1 - \phi^2 - \psi^2}{(1 + \phi^2 + \psi^2)} \quad (2)$$

where the average length of pulse \bar{a} is

$$\bar{a} = \int_0^{\infty} a P(a) d(a) \quad (3)$$

The space frequency ordinate against which the power spectra will be plotted is f_x .

If the cloud length is some arbitrary amount, then the angular subtense as observed from afar is inversely proportional to the distance from that cloud. For convenience, it is assumed that all clouds are grouped at 30,000 feet. The average angular subtense is, therefore, $4/r$ where r is the slant range in nautical miles from the observing station to the clouds. The probability of a particular pulse length a is then

$$P(a) = (r/4)^2 a e^{-ar/4} \quad (4)$$

Solving for $\Phi(f)$ and $\Psi(f)$ by substituting Equation (4) in Equation (1), we have

$$\Phi(f) + j\Psi(f) = \frac{(\tau/4)^2}{(\tau/4 + j\omega)^2} \quad (5)$$

and the resulting power spectrum from Equation (2) is

$$S(f_x) = r \left(\frac{\omega^2 + r^{2/8}}{\omega^4 + r^{4/64}} \right) \quad (6)$$

since $\bar{a} = 8/r$.

This power spectrum is plotted in Figure 36 and shows a power spectrum "break point" which varies with range or distance to the clouds. The dc or ambient radiometer results in a delta function at the origin. The ambient intensity remains invariant with altitude, or aspect, or space frequency bandwidth of field of view.

It is helpful to compare the above model with some actual sky or background observations and measurements. Several aspects will be considered; (1), the relation of the average or ambient level with respect to the contrast in intensity for clouds and sky background in the near and middle infrared; (2), the space frequency from which one can assume that the $1/f^2$ power spectrum intensity dependence holds; and (3), the effect of the sharpness of the step changes of intensity on the power spectrum.

In the near infrared the variation in intensity between a white cloud and adjacent blue sky is very pronounced. There is a change of an order of magnitude of 10 to 1000 times the intensity level. This sharpening of contrast in the near infrared has been frequently measured and is borne out by simple observations of heightened cloud contrast in photographs taken in the near infrared. The variation of intensity in the mathematical model must therefore be assumed to be of the same order of magnitude as the existing ambient level determined from the solar constant and albedo of the Earth.

In the middle infrared from $3.5 - 8\mu$ where the background energy primarily arises from the thermal emission of clouds or background, however, the contrast is not as pronounced. For example, the apparent change in radiation from the blue sky to a cloud is of the order of 20 percent greater than the blue sky thermal radiation. The ratio of the intensity level change for the variation from the mean level between cloud to sky is therefore of the order of $1/10$ times the average or ambient level. In the $8 - 13\mu$ band, the contrasts are larger than the $4 - 5\mu$ band, but not as great as the $1.3 - 2.7\mu$ band. Contrast levels equal to 50 percent of the ambient may be assumed in this band. The predicted background intensity in the thermal emission band beyond 3μ therefore is simply taken as the product of the proper curve of Figure 36 times one-half the contrast level or 0.1 and the total 300°K blackbody radiation within a particular spectral band. The procedure for estimating background interference in the shorter wavelengths during daylight illumination is similar, but the contrast levels are assumed to be 100 percent, or 0.50 for $1/2$ the contrast level, and 5×10^{-5} of a 5900°K blackbody is used for solar illumination.

Figures 37 and 38 illustrate examples of the predicted one dimensional background interference as well as actual gradient measurements obtained in the field. Reasonable agreement in interference levels is evident.

The step change in intensity assumed in the calculations moreover, is not realized in practice - especially in the thermal emission band. This fuzziness of the edges of clouds (or edge softening) will further attenuate the higher space frequencies. For example, if a 30 foot distance at the edge of the cloud is required to go from one extreme intensity peak to 63 percent of the value of the opposite peak, then an additional break point in the power spectrum $N(f_x)$ will occur beyond which the attenuation is $1/f_x^4$. This cloud edge transient may commonly occur in the near infrared. In the thermal band, however, the transient length is probably longer to obtain 63 percent of the peak change from one level to another which

will thereby shift the second break point to an even lower space frequency. There has been, however, insufficient data accumulated to date to conclusively verify this increased attenuation, but it is strongly indicated in the measured data at high space frequencies. A clear indication of any such trend will be obtained when background data is obtained for space frequencies substantially greater than those being measured today.

TWO DIMENSIONAL BACKGROUND NOISE SPECTRA

The background noise has been considered only for a one dimensional power spectrum, $N(f_x)$. The conversion from one dimension to a two dimensional noise spectrum is considered here as well as methods for measuring the two dimensional spectra directly, $N(\sqrt{f_x^2 + f_y^2})$.

An aperture with sides Δx and Δy has a two dimensional filter function $r(f_x, f_y)$ defined by

$$r(f_x, f_y) = \frac{\sin \pi f_x \Delta x}{\pi f_x \Delta x} \cdot \frac{\sin \pi f_y \Delta y}{\pi f_y \Delta y}$$

If Δx and Δy are approximately equal to each other, one obtains the one dimensional noise spectra considered earlier after compensation for the aperture in the scan direction. This correction factor is the reciprocal of the aperture function in the scan direction (if the filter function in the normal direction to scan is invariant) i. e., for scans in x direction with a square field at space frequency f_x .

$$\text{Aperture Correction} = \frac{\pi f_x \Delta x}{\sin \pi f_x \Delta x}$$

This aperture when convolved with the background noise, however, is then represented as the noise existing at a particular space frequency f_x . Actually, the background noise is for a constant f_x but includes a wide space frequency bandwidth in the normal

or f_y direction, most of which exists at distances substantially greater than f_x from the origin where relatively little background occurs. A two dimensional spectra derived from a one dimensional scan assumes an isotropic behavior, i. e., that the background noise level is only a function of $\sqrt{f_x^2 + f_y^2}$. To correct the one dimensional noise spectra for two dimensions, one must then divide the resulting output by the effective bandwidth in the normal direction to the scan.

If the effective bandwidth is considered to lie between the 1/2 power points, then in the presence of background noise varying inversely with space frequency, the effective bandwidth Δy at a one dimensional space frequency f_x is $\Delta y = 1/2f_x$.

At the low space frequency end, however, the background noise spectra is constant or "white." In this region, the effective bandwidth Δy will be constant and approximately equal to $1/2\sqrt{2} f_b$ where the break point f_b is the space frequency at which the transition between white and inverse space frequency dependence occurs. The resulting two dimensional noise spectra is illustrated in Figure 39.

The two dimensional characteristic noise spectra of background may be derived directly with a slit scan if the effective space frequency bandwidth normal to the scan direction is small in comparison with the space frequency in the scan direction. This was discussed by R. Clark Jones in 1955⁽²⁴⁾ for regions of space frequency f_x which are significantly higher than $1/2 \Delta y$. In such circumstances, the effective bandwidth Δy in the direction normal to the scan direction is a constant and the resulting two dimensional noise spectra may be represented as occurring at space frequencies equal to f_x , i. e., $|\sqrt{f_x^2 + f_y^2}| \sim |f_x|$.

RETICLE - APERTURE SPACE FILTERING

There are two convenient and alternative methods of analysis which permit a study of the space discriminating ability of optical systems--space and space frequency. The detail of light distribution across the object or image, whether from the background or target, can be expressed mathematically as a function of its intensity and the linear position in that plane, such as x and y . It may also be expressed mathematically as a function of inverse space or $1/x$ and $1/y$, in which case it is analogous to frequency in the true sense, and is called space frequency f_x and f_y . These equivalent descriptions of a function are analogous to the study of electrical networks in either the time domain (impulse and correlation function), or frequency domains (frequency response and transform analyses). The appropriate mathematical relations involved in space filtering are described more fully below.

In the general case, an object has a particular location in space and time, and also has particular reflection or emission characteristics for electromagnetic energy. The electromagnetic energy is, for all intents and purposes, incoherent in the visible and infrared spectrums and thus only the intensity is of interest. The optical imaging system is further assumed to be linear (displacements from center of field and intensities are proportional in object-image), as is the transmission factor of the optical elements; i. e., they are isoplanatic.

The total optical processing from the object plane to the cell is illustrated in Figure 40. A lens or mirror forms a two-dimensional image, which, grossly speaking, is linearly related to the object. The blur circle or aberration in the image plane is defined by the light distribution which arises from a point source and is analogous to the impulse response in electrical networks. The image of an extended object, however, is formed by the summation of many blur circles arising from the many point sources in the object. This resulting addition to describe a function in a linear

system is known as the superposition integral and is conveniently dealt with mathematically by use of the Fourier transforms. Therefore, the object can be expressed in terms of its two-dimensional space frequency content, the lens or mirror has a space frequency transfer characteristic (the transform of the blur circle) or "pass-band" which is an ability to translate this object detail into image detail, and the resulting image has a quality or space frequency content which is simply the product of the object function and lens function. This dependence on the object-image function has been described by Duffieux,⁽²⁷⁾ Elias,⁽²⁸⁾ and others.

In real space the reticle and field stop combination multiply their transmission function by that of the image. The field lens subsequently integrates the total light intensity which passes through the reticle by imaging the primary collector. The reticle function itself, however, must be separated into its time and space variables if it is simultaneously chopping and scanning. The resulting integrated space frequency multiplication results in a real convolution which is modulated at a time frequency depending on the separated time variable in the reticle function.

Mathematically, the output of a cell or detector $c(x, y, t)$ is desired as a function of: (1) the object intensity distribution corresponding to the background or target, $o(\xi, \eta)$; (2) the transmission factor of the optics, $s(x, y)$, which corresponds to the "spread function" or the blur circle pattern of a point object as seen on the image plane; and (3) the reticle function, $r(x, y, t)$, which may be simultaneously scanning and chopping the image.

The spread function, $s(x, y)$, is the light intensity distribution of a point object in the image plane. An extended, incoherently illuminated object, $o(\xi, \eta)$, has a resulting image, $i(x, y)$, composed of the integral of many point sources in the object modified by the transmission function. If unit magnification is assumed, then

$$i(x, y) = \iint_{-\infty}^{+\infty} s(x - \xi, y - \eta) o(\xi, \eta) d\xi d\eta \quad (1)$$

The light distribution immediately behind the reticle is the real space multiplication of the reticle and image. The field lens, however, integrates this total light intensity distribution upon a cell or detector. Furthermore, relative motion of the reticle in space imparts a real space convolution to the two space functions when combined with the integrating effect on the cell-condenser combination. The reticle function itself is separated into orthogonal time and space variables in a manner analogous to traveling wave theory.⁽²⁹⁾ The total light intensity falling on the cell is the product of each individual differential area summed or integrated over the various reticle displacements x' , y' , and modulated at the time frequency of the reticle.

$$c(x, y, t) = r_1(t) \iint_{-\infty}^{+\infty} r_2(x', y') i(x-x', y-y') dx' dy' = c(t) c(x, y) \quad (2)$$

The functional relationships in Equations (1) and (2) may also be related to each other in space frequency terms by employing the two-dimensional Fourier transform of a function, $f(x, y)$, defined as follows:

$$F(\omega_x, \omega_y) = \iint_{-\infty}^{+\infty} f(x, y) e^{-j(\omega_x x + \omega_y y)} dx dy$$

The resultant spatial transform of the cell output related to all the optical and reticle components is then

$$C(\omega_x, \omega_y) = R_2(\omega_x, \omega_y) S(\omega_x, \omega_y) O(\omega_x, \omega_y) \quad (3)$$

In summary, the total image processing from the object plane to the detecting element can be treated conveniently with Fourier transforms. The light intensity modulation on the cell is the product of the two-dimensional transform or space frequency of the object the lens and the reticle or field stop all modulated at a time frequency

determined by the separated time function of the reticle. Figure 41 illustrates two examples of circular field stops with rotating reticles. With stationary reticles, the time frequency output f_t is equal to the resulting transformed noise output $f(x, y)$, v_s where v_s is velocity in the scan direction.

In order to estimate background interference in any particular system, therefore, the product of the two dimensional noise spectrum, and the two dimensional reticle function are integrated at the modulating or time frequency of the reticle. If for example, the background noise of a 3° field of view tracker, with 3 milliradian reticle spacing in the $3.5 - 5.5\mu$ spectral band were desired, the following steps could be taken.

The reticle reinforcement frequency occurs at $1/(2 \times 3 \text{ mr})$ or 160 waves/radian. The effective bandwidth of the aperture at this frequency is approximately $1/\Delta x$ in the f_x direction and $1/\Delta y$ in the f_y direction or 19 waves/radian in each direction. The background at 160 waves/radian is assumed while within the space bandwidths of the aperture considered. The reticle has a field of view $\Omega = 277 \times 10^{-3}$ steradians but it is only 50 percent transmissive. The background contrast is 20 percent. Total 300°K blackbody radiation is 1.5×10^{-2} watts/cm²/steradian of which 2.5 percent occurs between 3.5 and 5.5μ . The background from Figure 38 at 160 waves/radian for an average distance to clouds of 5 n. mi. is then

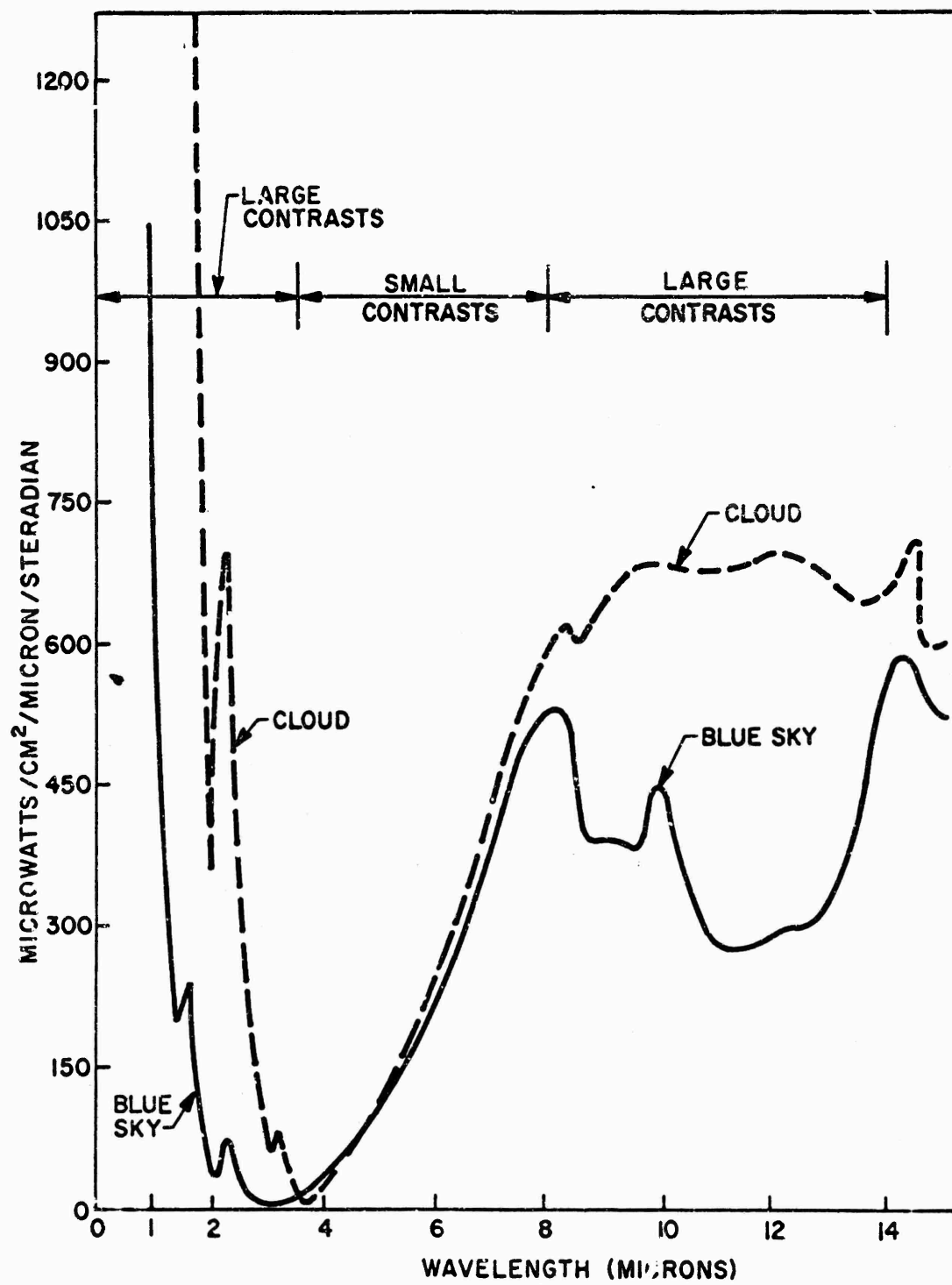
$$N(f_x, f_y) = \frac{6 \times 10^{-2}}{160^3} \times \left(1.5 \times 10^{-2} \times \frac{2.5}{100} \times \frac{1}{2} \times \frac{20}{100} \right)^2 \left(\text{w/cm}^2/\text{steradian} \right)^2$$

$$\left(\text{wave/radian} \right)^2 = 2 \times 10^{-17} \left(\text{w/cm}^2/\text{steradian} \right)^2 / \left(\text{wave/radian} \right)^2$$

The actual interfering noise irradiance is $\int N(f_x, f_y) R(f_x, f_y) d f_x d f_y$ where $R(f_x, f_y)$ is the Fourier transform of the reticle function or approximately $(\Omega/2)^2 (1/\Delta x) (1/\Delta y)$, at the reinforcing frequency,

$$\begin{aligned} \text{i. e., Noise Power} &= 2 \times 10^{-17} \times \left(1.38 \times 10^{-3}\right)^2 \times 19 \times 19 \\ &= 1.4 \times 10^{-20} \left(\text{w/cm}^2\right)^2 \end{aligned}$$

<p>Estimated Background Noise = 1.2×10^{-10} watts/cm² (rms)</p>



AW46-241

Figure 33. Radiometric Sky Observations

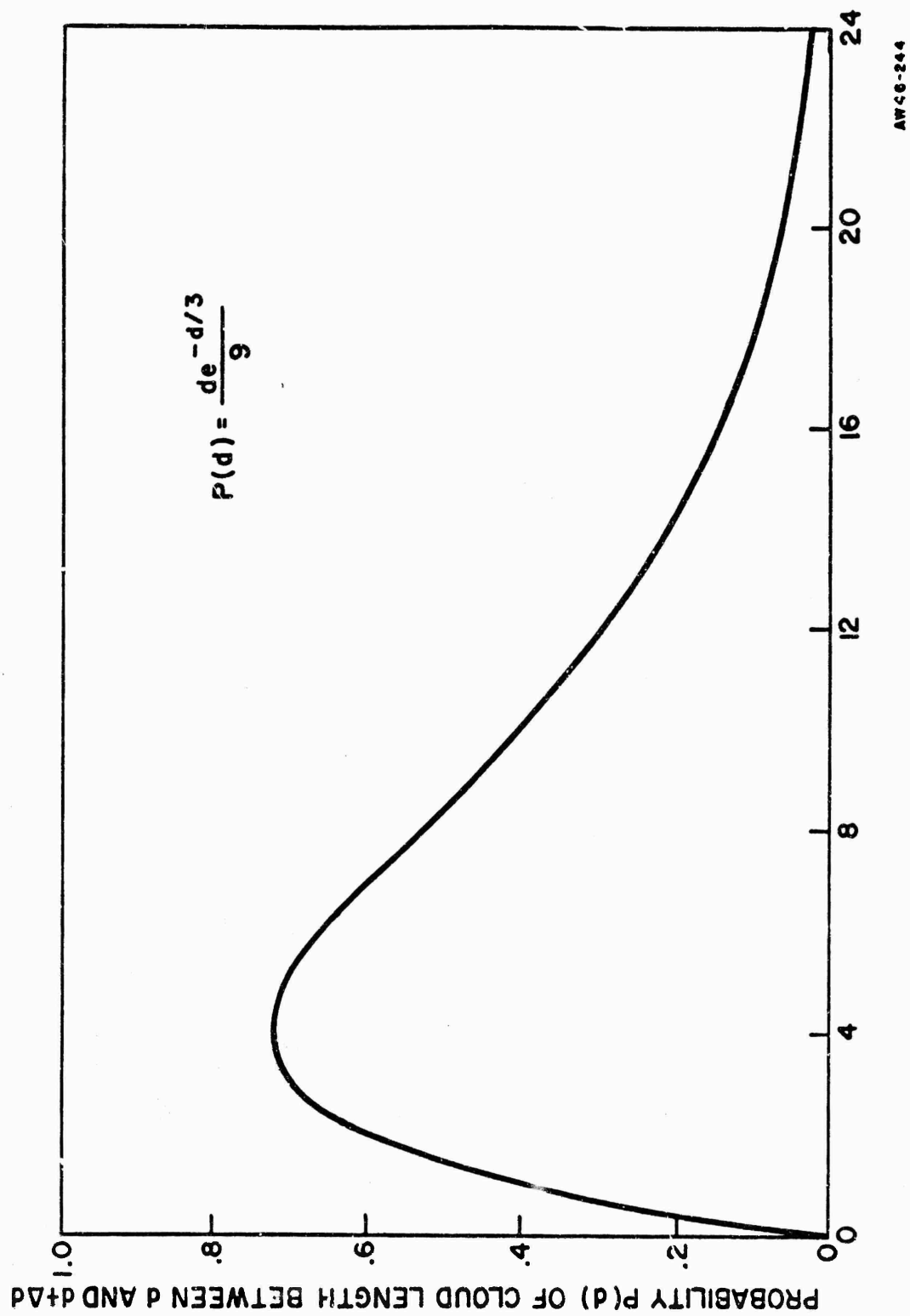
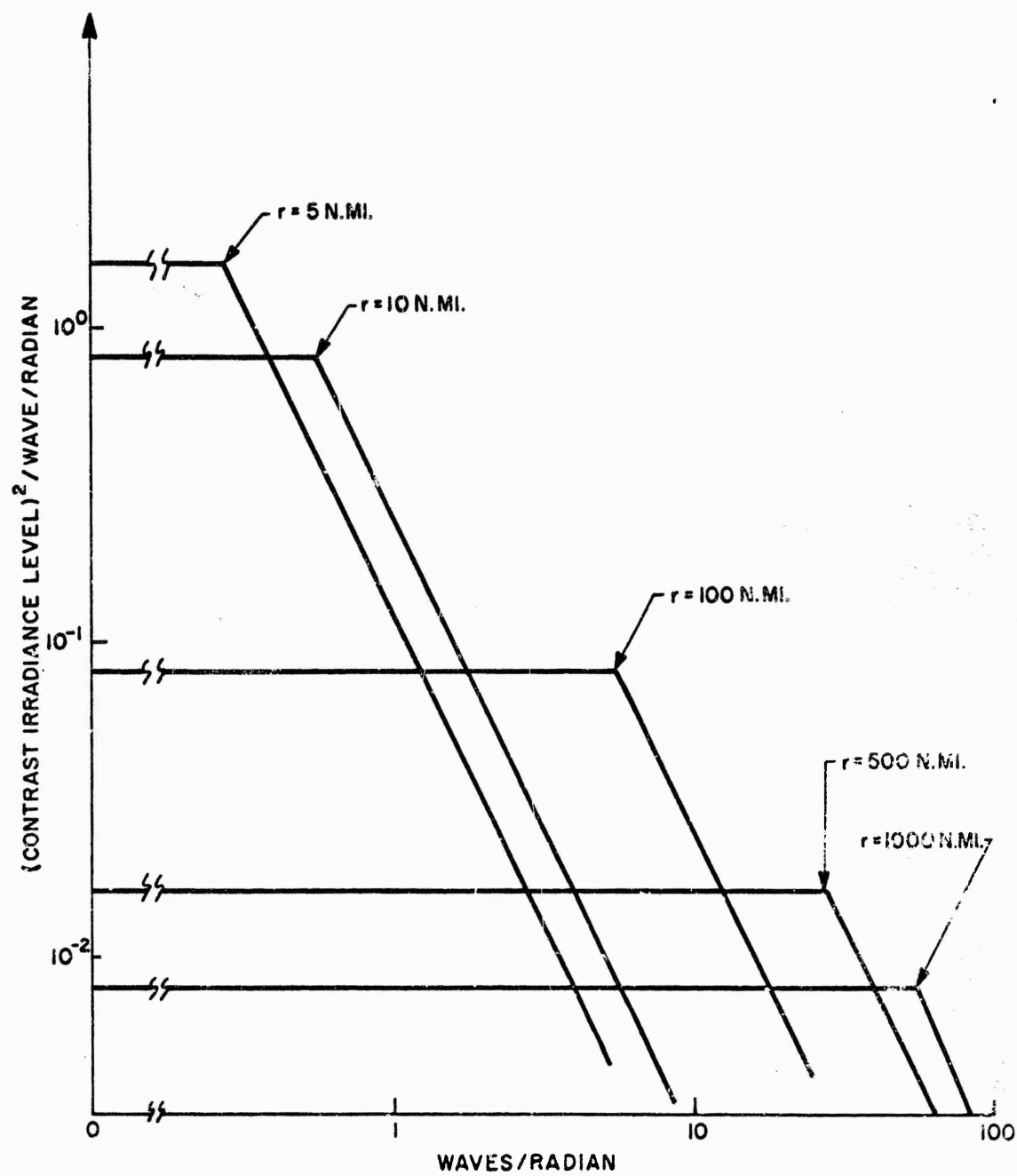
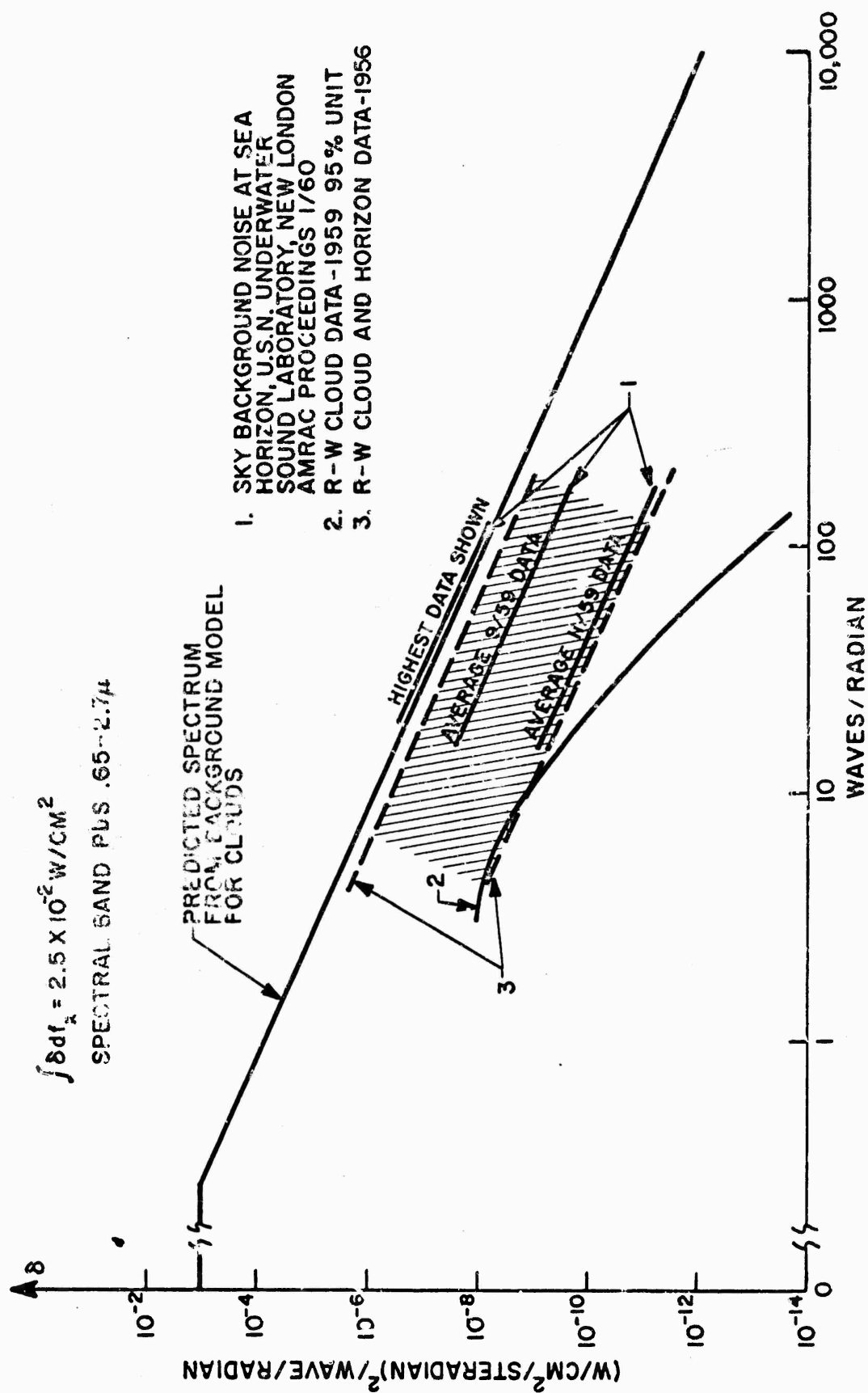


Figure 34. Assumed Probability Distribution of Cloud Lengths



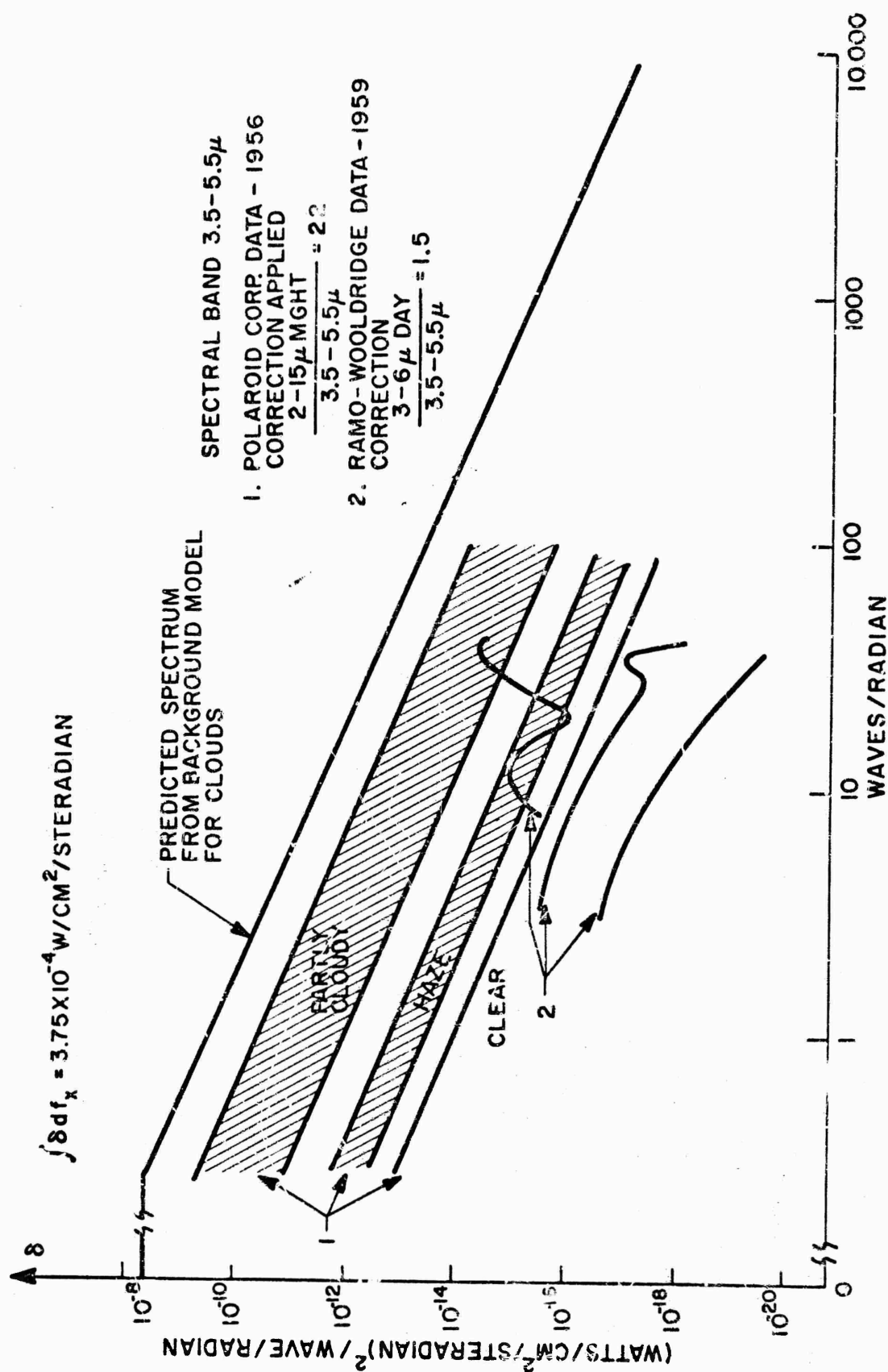
AW46-233

Figure 36. Predicted One Dimensional Wiener Background Spectra



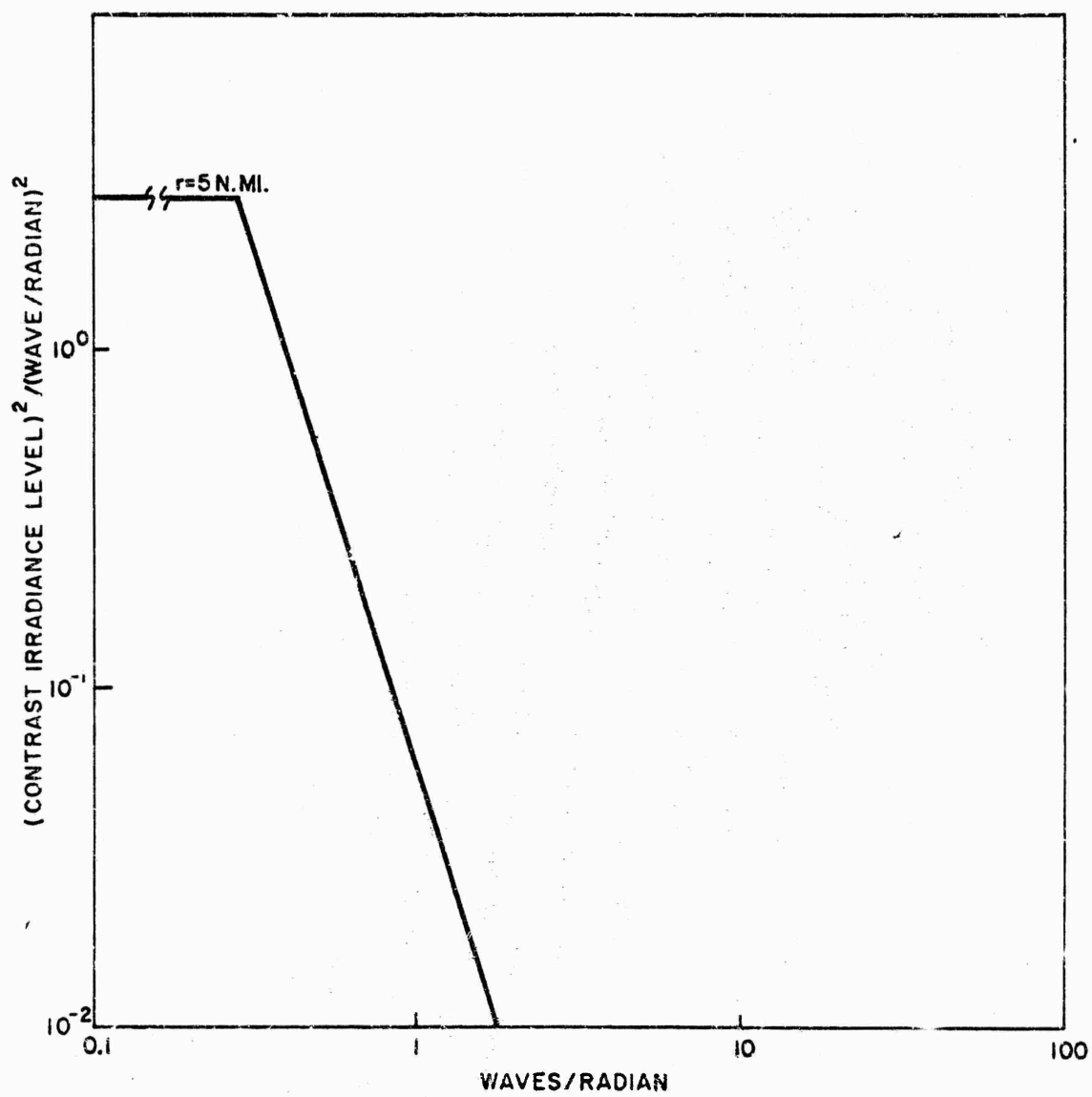
AW 46-243

Figure 37. One Dimensional Wiener Background Spectra - Solar Reflection



AW 46-252

Figure 38. One Dimensional Wiener Background Spectra - Thermal Emission



AW 46-240

Figure 39. Predicted Two Dimensional Wiener Background Spectra

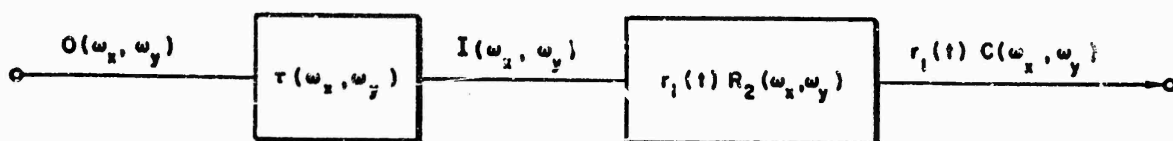
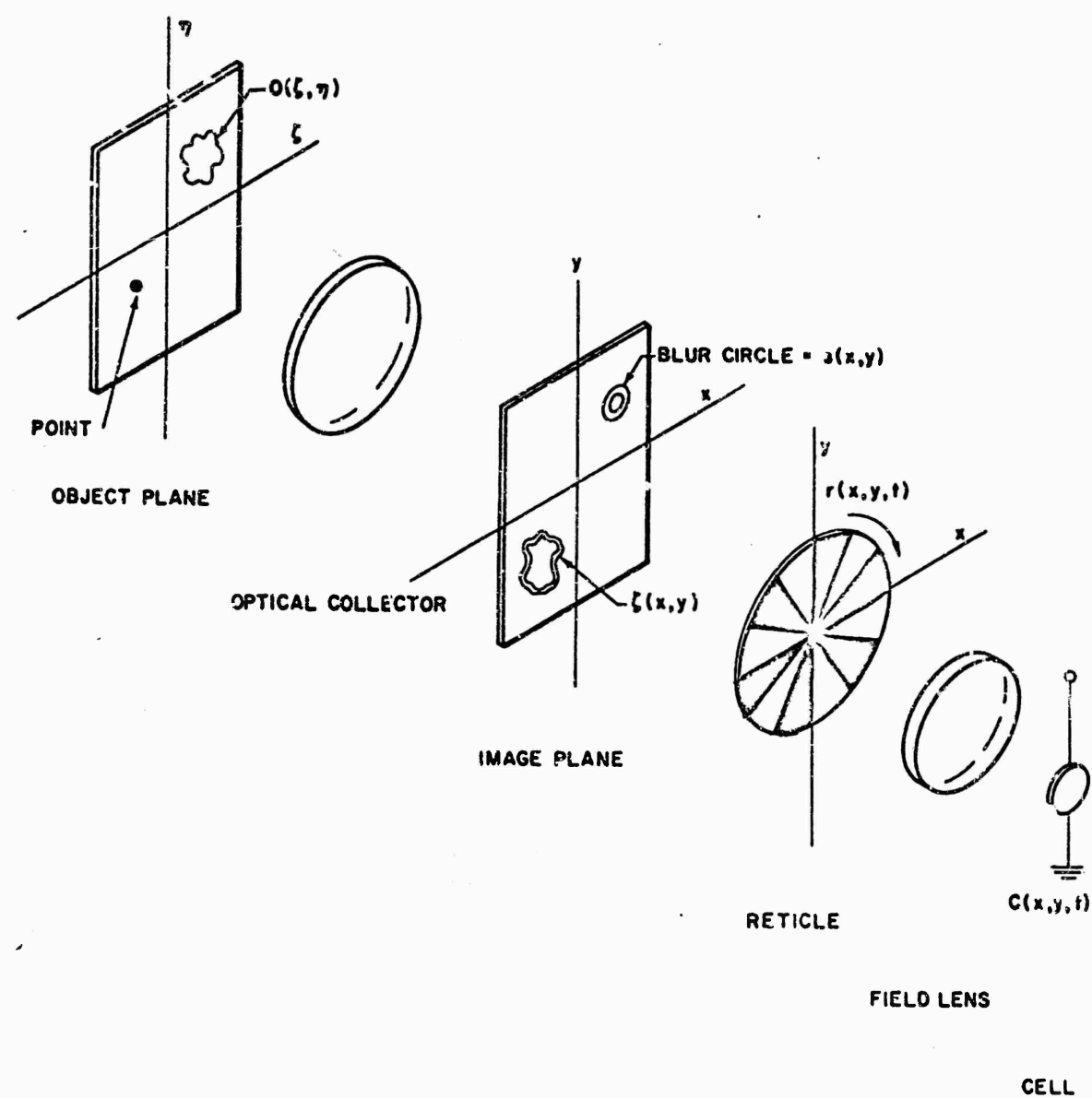


Figure 40. Linear Optical Imaging System

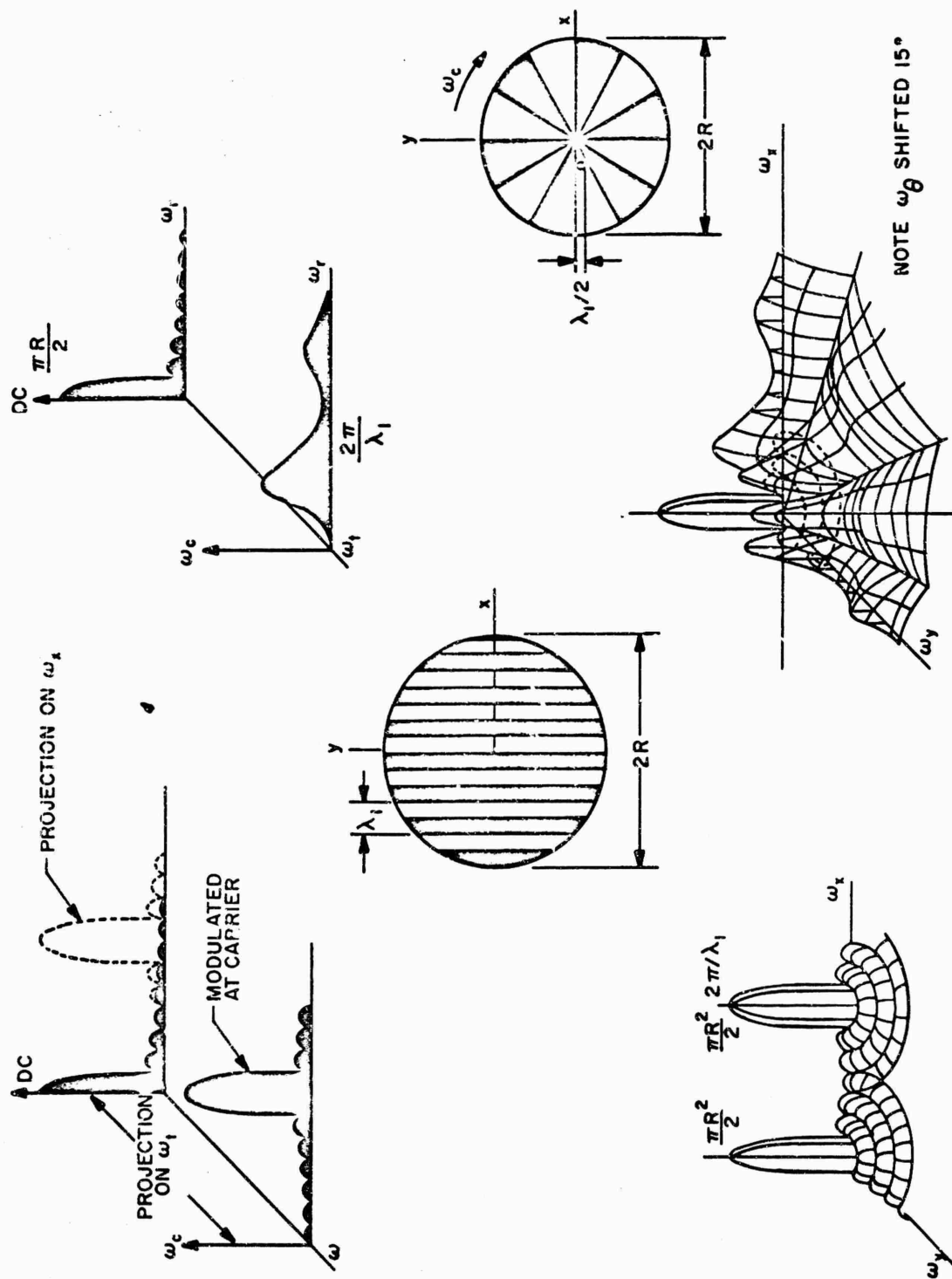


Figure 41. Transform of Parallel Slit and Radical Reticles

SUMMARY

The investigation of infrared sky backgrounds has been a continuing project since 1953. In that year, at North American Aviation, Inc., under Contract AF 33 (600)-24347 (WADC), the instrument known as a radiometer-gradient meter was designed, fabricated, and functionally tested. Additionally, a high-altitude weather study was performed. Four quarterly reports and a final report were issued.^(1, 2) The four quarterly reports embody the engineering, design and test of the instrument, associated electronics and the low temperature black-body calibrator. The second quarterly report contains a section devoted to the linear scanning motion of the instrument and the difficulties associated with the separation of the background Wiener spectrum and the spectra developed by the distortions of a saw tooth or triangular wave scan. Other details pertinent to the design of an instrument to produce an accurate measure of space frequencies is embodied in that report.

Quarterly Progress Report No. 4 of AF 33(600)-24347 contains a pertinent discussion on the Infrared Scattering of Sky Light based on the work by R. Tousey and E. O. Hulbert. The final report for the North American Aviation effort publishes the first Wiener spectra produced by the gradient meter in testing its functional capability. Realization of the need for this type of data is enhanced by the fact that copies of this data, first published in 1954, were requested of the author as late as 1957. The final report also contains the results of the high-altitude weather research which is a very complete and concise discussion of upper air meteorological phenomena. A remarkably complete and up-to-date (1954) source bibliography on the subject is included as well.

Infrared sky background investigations were continued by Ramo-Wooldridge, Corp., beginning in 1955 under Contract AF 33 (600)-30489. Three reports were issued semi-annually, tracing

the progress of the program. The equipment was readied for field use and a company-owned mobile laboratory was outfitted for this purpose. In addition, the radiometer was equipped with a set of 7 narrow band (Turner) interference filters for making spectral measurements in the region from 1 to 4.25 microns. During this program, the equipment was moved to the Colorado Springs, Colorado area for cooperative participation in the IRMP/56. The second semiannual report and the final report for this contract contain many individual Wiener spectra made at Mt. Wilson at 6000 feet altitude and also from the roof of one of the Ramo-Wooldridge buildings at sea level.⁽³⁾ The final report for this contract contains, as an appendix, a reprint of a paper by P. R. Karr of the Ramo-Wooldridge Corp. entitled "Mathematical Study of Background 'Noise'," presented at the second meeting of the East Coast IRIS, 26 April 1957. This is a highly valuable paper because it contains a number of elements particularly concerned with circular scanning, which is the method most used in obtaining the gradient data. Some of the equations are utilized in the main body of the report to present an example of the space frequency transmission of a simplified reticle.

The background investigation work continued to be performed by Ramo-Wooldridge, now a division of Thompson Ramo Wooldridge, Inc., under Contract AF 19 (604)-3473, from the Geophysics Research Directorate of the Air Force Cambridge Research Center. Four reports have been issued under this contract including this, the final report.⁽⁴⁾ Report No. 1 presented the first Wiener spectra to give an indication of the space frequency amplitudes in the lead selenide region. Report No. 2 is a comprehensive tabulation of sky gradients in the Key West area, while No. 3 tabulates radiometric measurements made at the same time. The present final report represents the generalization of the tabulated data in the two previous reports and, in addition, presents a model for background sky noise that may be of help in predicting levels at the higher waves per radian where much interest is centered today.

The equipment used since 1953 is essentially the same as designed, with a few minor improvements added during the course of time. It is substantial and dependable with no instrument "headaches". This dependability and accuracy of measurement has enabled the mass of data to be taken. In addition, the large amount of gradient data taken at Key West might have remained unreduced and consequently of no use had it not been for the use of the computer facilities at Ramo-Wooldridge.

REFERENCES

- (1) Study of Background Radiation and High Altitude Weather, North American Aviation, Inc., Downey, California, Quarterly Progress Reports, EM-300-1, -2, -3, -4, (1953-1954)
- (2) Whitney, T. R., "Study of Background Radiation and High Altitude Weather": WADC, TR54-581 (December 1954)
- (3) Infrared Sky Background Investigation, The Ramo-Wooldridge Corporation, 1st, 2nd, and final reports, RW 1631.70, 1631.84 and 1631.87, Contract AF 33(600)-30489, (1956-1957)
- (4) Eisele, R. E. "Infrared Background Investigation", Ramo-Wooldridge, a division of Thompson Ramo Wooldridge, Inc. Scientific Reports No. 1, 2, and 3, TN-59-843, TN-60-408, (TN number not yet issued) AFCRC - Contract AF 19 (604)-3473, (1959-1960)
- (5) The Earth as a Planet, edited by G. P. Kuiper, the University of Chicago Press, Chicago, Ill. 1953.
- (6) J. N. Howard, D. L. Burch, D. Williams, "Near - Infrared Transmission Through Synthetic Atmospheres", Geophysics Research Directorate, AFCRC.
- (7) R. Tousey, E. O. Hulburt, "Brightness and Polarization of the Daylight Sky at Various Altitudes Above Sea Level", JOSA, Vol. 37, No. 2.
- (8) H. S. Aufm Kampe, H. K. Weickman, "Physics of Clouds", Meteorological Monographs, Vol. 3, No. 12-20, American Meteorological Society.
- (9) H. A. Gebbie, et al, "Atmospheric Transmission in the 1-14 μ Region", Admiralty Research Laboratory, Teddington, Middlesex.
- (10) M. C. Gibbons, "Wavelength Dependence of the Scattering Coefficient for Infrared Radiation in Natural Haze", U.S. Naval Radiological Defense Laboratory, San Francisco, 1957.
- (11) J. Doyne Sartor, "Meteorological Aspects of Infrared Operations", IRIS, Vol 3, No. 4, Dec. 1958.
- (12) R. M. Goody, "The Physics of the Stratosphere", University Press, Cambridge, England, 1954.
- (13) H. C. van de Hulst, "Light Scattering by Small Particles", John Wiley and Sons, Inc. N. Y. 1957.
- (14) W. E. K. Middleton, "Vision Through the Atmosphere, University of Toronto Press, 1952.
- (15) Z. Sekara, "Scattering of Light in the Atmosphere and Diffuse Sky Radiation", Science Progress, London, 1957.

REFERENCES (Cont'd.)

- (16) G. C. Clark, C. M. Chu, S. W. Churchill, "Angular Distribution Coefficients for Radiation Scattered by a Spherical Particle", JOSA, Vol 47, No. 1.
- (17) P. T. Vandehei, "NAMTC Participation in Infrared Measuring Program in Colorado Springs Area", Technical Memorandum Report No. 111, Bureau of Aeronautics, June 1958.
- (18) Raymond William Sloan "The Infrared Emission Spectrum of the Atmosphere", Geophysics Research Directorate, AFCRC-TN-56-474, Contract AF 19(604)-1003, 1956.
- (19) H. E. Bennett, Jean M. Bennett, and Max R. Nagel, "Distribution of Infrared Radiance Over a Clear Sky", JOSA, Vol. 50, No. 2, 1960.
- (20) D. E. Burch and J. H. Shaw, "Infrared Emission Spectrum of the Atmosphere", JOSA, Vol. 45, No. 6, 1955.
- (21) Z. Sekera, "Scattering in the Atmosphere and the Polarization of Sky Light", JOSA, Vol. 47, No. 6, 1957.
- (22) H. Siedentopf, "Measurements of Illumination and Brightness in the Troposphere with Application to the Visibility of Aerial Targets and Stars in the Daylight Sky", Forschungsbericht Nr. 1937/1, Universitäts - Sternwarte Jena, Translated Sept. 3, 1952 for Geophysics Research Center, AFCRC, under AF 19(604)-203.
- (23) "New Approach to the Problem of Determining the Change of Scattered Radiation of Cloudless Skies", Air Intelligence Summary Report No. 1268F58 Prepared by Heinz Sack (FN), 7000th Supporting Wing (USAFE), 1959.
- (24) R. Clark Jones, "New Method of Describing and Measuring the Granularity of Photographic Materials", JOSA, Vol 45, No. 10, 1955.
- (25) George F. Aroyan, "Space Filtering by Reticles", The Ramo-Wooldridge Corp., IRIS, March 1958.
- (26) D. Z. Robinson, "Methods of Background Description and Their Utility", IRE Proceeding, Vol 47, No. 9, 1959.
- (27) P. M. Duffienx, P. M., "L'Integral de Fourier et ses Application a l'Optique", Besancon, Faculte des Sciences, 1946.
- (28) P. Elias "Optics and Communication Theory", JOSA, Vol 43, No. 4, 1953.
- (29) J. A Stratton, "Electromagnetic Theory", McGraw-Hill, N. Y., 1941, Chapter V, VI, VIII, IX.